Scattering and Coherence Phenomena in the Photoionization of Small Molecules

vorgelegt von
Diplom-Physiker
Daniel Rolles
aus Berlin

Fakultät II - Mathematik und Naturwissenschaften
der Technischen Universität Berlin
zur Erlangung des akademischen Grades

Doktor der Naturwissenschaften
– Dr. rer. nat. –

genehmigte Dissertation

Promotionsausschuss:

Vorsitzender: Prof. Dr. rer. nat. M. Dähne
Berichter/Gutachter: Prof. Dr. rer. nat. T. Möller
Berichter/Gutachter: Prof. Dr. rer. nat. U. Becker

Tag der wissenschaftlichen Aussprache: 25. Mai 2005

Berlin 2005
D 83

This document was generated using MikTeX pdf-LaTeX.
It is also available as a PDF document with *hyperlinks* at
`http://agb2.rz-berlin.mpg.de/~rolles/thesis.html`

Parts of this work are published separately. A comprehensive list of publications is attached in Appendix E. References to the particular articles are also given at the respective places in the text.

Abstract

Scattering, interference, and coherence phenomena are discussed for the inner-shell photoionization of the two showcase molecules carbon monoxide and nitrogen. The inner-shell photoionization process is studied using high resolution angle-resolved photoelectron time-of-flight spectroscopy as well as angle-resolved photoelectron–photoion coincidence spectroscopy (ARPEPICO). In the latter technique, the spatial orientation of free gas-phase molecules is determined from the fragment-ion momenta measured in an ion time-of-flight spectrometer equipped with a position sensitive anode.

In the heteronuclear CO molecule, the scattering of the carbon core photoelectron on the neighboring oxygen atom leads to photoelectron diffraction, which, for the first time, is studied over a wide energy range in a free gas-phase molecule. The measurement reveals a different diffraction behavior of the forward and backward scattering channels and provides the means for a direct determination of the molecular structure of a free molecule via photoelectron diffraction. It also provides direct evidence for the multiple scattering character of the so-called shape resonance, which is a prominent feature in the photoionization of small molecules.

In the homonuclear N_2 molecule, the inversion symmetry of the molecule and the resulting non-locality of the core electrons lead to coherent photoelectron emission from two identical atomic sites. The two-slit nature of the emission process is demonstrated by characteristic interference patterns in the molecule frame photoelectron angular distribution of the $1\sigma_g$ and $1\sigma_u$ core states. The transition to the symmetry-broken system of localized electrons is studied by comparing different isotope substituted species of the N_2 molecule. Isotope substitution is shown to lead to a partial localization of the non-local core hole, exhibited by a parity mixing of the outgoing photoelectron wave, if the substitution breaks the inversion symmetry of the molecule. This is the first experimental observation of such a Born-Oppenheimer forbidden isotope effect on the photoelectron spectrum of a diatomic homonuclear molecule. It demonstrates the onset of the gerade-ungerade symmetry breakdown accompanying the continuous transition from non-localization to localization and coherence to incoherence.

Contents

Chapter 1

Introduction

Coherence and interference are fundamental traits of the quantum world - or, as Feynman put it, single-particle interference is "*a phenomenon which is impossible, absolutely impossible to explain in any classical way, and which has in it the heart of quantum mechanics*".[1] This may be the reason why to this day, Young's two-slit experiment with massive particles has not lost any of its appeal as scientists around the world study the single- and multi-particle interference of electrons, positrons, neutrons, atoms (even some made of antimatter) and molecules as large as fullerenes[2] or even biomolecules.[3,4]

As physicists and physical societies around world are celebrating the *World Year of Physics*,[5] which commemorates this year's *100th anniversary of the photon*[6] and Einstein's *annus mirabilis*, just a few years after the equally celebrated *centennial of quantum physics*, a renewed interest has sparked in these fundamental concepts, and experiments studying the foundations of quantum mechanics are experiencing an unprecedent revival.[7,8] Modern state-of-the-art experimental techniques are applied to repeat and improve some of the first, groundbreaking experiments that led to the development and understanding of quantum theory. Yet, at the same time, the applications of quantum physics are also pushed into the new realms and the new fields of quantum cryptography, quantum teleportation and quantum computing are already paving the way for a future "quantum information technology".[7]

In this dissertation, the concepts of coherence and interference are discussed in the context of molecular photoionization, which seems particularly appropriate in the year of the 100th anniversary of Einstein's explanation of the photoeffect.[9] The work is situated right at the heart of quantum mechanics, discussing the classical particle phenomenon of scattering together with the quantum mechanical concepts of interference and coherence and stepping into the wide open field of the particle-wave dualism and the complementarity of these two pictures. And while bigger and bigger molecules are being entangled, single-particle interference experiments are performed on macroscopic molecules, and the wave-particle dualism is already taught in the high school physics class, there is still a surprising

amount to be learned about the simplest of all molecular systems, a diatomic molecule.

With the help of the modern spectroscopic tools of high-resolution angle-resolved photoelectron spectroscopy and photoelectron–photoion coincidence spectroscopy, the present work sheds some light onto very fundamental phenomena which relate to both 1920s quantum mechanics as well as 21^{st} century nanotechnology and quantum controlling.

After a general introduction into the physics of molecular photoionization in **chapter 2**, the experimental techniques applied in this work to measure high-resolution angle-resolved photoelectron spectra and photoelectron angular distributions of fixed-in-space molecules are explained in **chapter 3**. The subsequent chapters present showcase examples for scattering, interference and coherence effects in the photoionization of hetero- **(chapter 4)** and homonuclear **(chapter 5)** molecules, leading to a discussion of quantum mechanical indistinguishability and non-locality and the transition from coherence to incoherence probed by isotope substitution, in **chapter 6**. A summary of the main conclusions along with an outlook on future experiments and applications is given in **chapter 7**. Finally, a list of common symbols and abbreviations used in this work along with some additional background information can be found in the **Appendix**.

Chapter 2

Fundamentals of Molecular Photoionization

2.1 Photoeffect and Photoionization

Spectroscopic studies of atoms and molecules have substantially contributed to a thorough understanding of the structure of matter and have fundamentally influenced the development of modern physics. For many years, the only accessible information was contained in absorption spectra and in fluorescently emitted photons primarily in the visible spectrum. It was, to a big extend, the work Nobel laureate Kai Siegbahn and co-workers[10,11] in the 1960s and the advent of synchrotron radiation[12–14] in the 1970s that initiated the breakthrough of *photoelectron spectroscopy* (PES). In the broadest sense, this spectroscopy is based on the photoelectric effect discovered by Heinrich Hertz and Wilhelm Hallwachs in the late 1880s[15] and first explained by Albert Einstein's *light quantum hypothesis*[9] in 1905 as the process where an incident *light quantum* (i.e. *photon*) is absorbed by a solid and an electron with a certain kinetic energy is emitted.[a] Applying this concept to free *atoms* or *molecules,* light with the photon energy $h\nu$ creates, in the simplest case, a singly charged ion in its ground state and a photoelectron with kinetic energy

$$E = h\nu - E_{ion}, \tag{2.1}$$

where E_{ion} stands for the ionization energy of the respective electron (fig. 2.1(a),(b)). The atomic and molecular photoeffect is therefore called *photoionization*. According to *Koopmans' Theorem*,[16] the ionization energy of an electron in a bound state i corresponds to

[a] In the original sense, the photoelectric effect describes the emission of an electron from a solid when irradiated with electromagnetic radiation. Einstein postulated that each *light quantum* or *photon* carries a discrete energy $h\nu$, and that the kinetic energy of the photoelectron E corresponds to the difference between the photon energy and the energy which is needed to liberate the electron from the solid (usually called *work function* Φ).

the (negative) eigenvalue E_i of this state.[b] A simple photoelectron spectrum thus contains directly the information about the binding energies of the electronic states in the atom or molecule. Furthermore, photoelectron spectroscopy also allows to obtain a multitude of information about the fundamental nature and the dynamics of the photoionization process as well as, in more complex systems, about the electronic structure, chemical binding and composition of the studied sample.[10,11,17–19] Because of its far reaching applications, PES has nowadays become a standard tool in chemistry, material science, condensed matter, and atomic and molecular physics.

For the sake of simplicity, let me first concentrate on atomic photoionization and discuss additional features of molecular photoionization in chapter 2.2. Apart from the direct single photoionization described by eq. (2.1) and shown in fig. 2.1(a) and (b), there are *many-electron effects* in which more than one electron participate in the transition.[20] One example is the *shake-up* process in fig. 2.1(c), where part of the photon energy is transferred via Coulomb interaction to a second electron and promotes this electron in an excited orbital. In that case, the photoelectron is "missing" the respective energy and the photoelectron spectrum contains *satellite lines* in addition to the (generally) strong main line which represents the direct single photoionization. The satellites are also lines of discrete energy since the second electron can only be excited in discrete energy states. An exception is the *shake-off* or *direct double photoionization* in fig. 2.1(d), where two photoelectrons are emitted simultaneously and the available total energy is shared in an arbitrary ratio among the two electrons.[21,22]

If the emitted photoelectron does not originate from the outermost occupied orbital or if a satellite excitation takes place, the resulting ion remains in an excited state (i.e. it is not in the state of lowest possible energy) and can decay further.[23] If energetically possible, a *non-radiative* de-excitation, the *Auger decay*,[24] is the dominating process in light atoms and molecules.[c] In the Auger decay, an electron from an orbital which energetically lies above the hole created by the photoionization fills this hole and transfers the liberated energy to another electron via Coulomb interaction. The second electron leaves the atom as an *Auger electron* (fig. 2.1(e)-(h)). Schematically, these *nonresonant* Auger decay processes are usually described as a two-step process:[d]

$$\mathrm{A} + h\nu \quad \rightarrow \quad (\mathrm{A}^+)^* + e^-_{Photo} \tag{2.2}$$

$$(\mathrm{A}^+)^* \quad \rightarrow \quad \mathrm{A}^{++} + e^-_{Auger}. \tag{2.3}$$

[b] Strictly speaking, this is true only in the *independent electron approximation* which neglects correlation and relaxation effects.

[c] Another possibility is the *fluorescent* decay via photon emission. This process will not be discussed further since it amounts to a minor contribution in the molecules considered here[25] and is not necessary for the understanding of this work. For details on the fluorescent decay, I refer to the standard textbooks.[26–28]

[d] Although the two-step model is often applicable, a breakdown of this model is known for certain conditions; post-collision interaction (PCI) and electron recapture effects close to threshold are prominent examples.[29,30] For molecular inner-shell ionization, indications for a breakdown of the two-step model have been reported by Guillemin *et al.*[31]; however, these findings could not be confirmed in a subsequent study by Weber *et al.*[32]

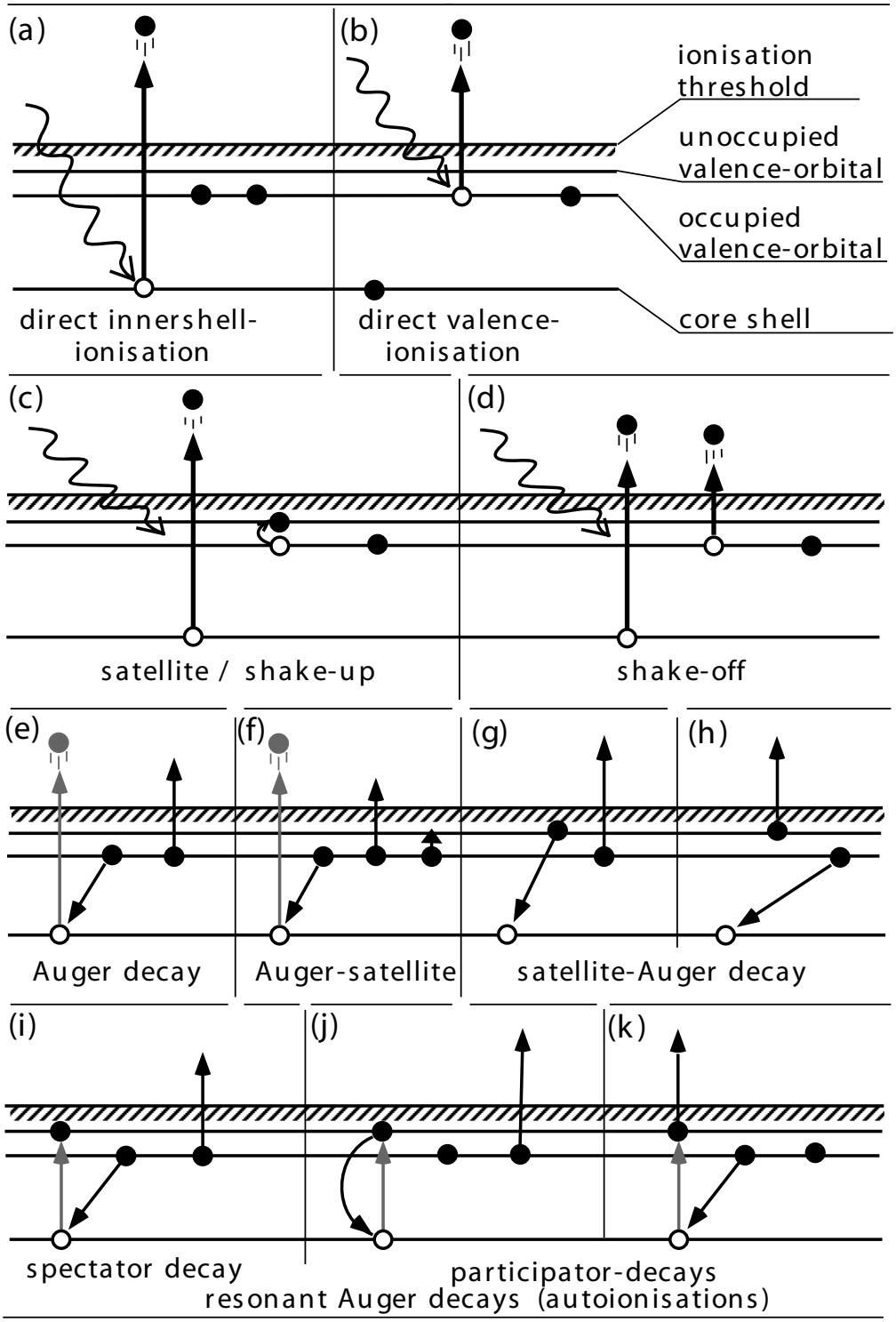

Figure 2.1: Common atomic photoionization processes[33]

Note that an Auger decay can also happen if the photoexcitation in eq. (2.2) does not produce a photoelectron and an ion but only excites an electron from an inner shell (also called *core electron*) into a bound state, whose energy lies above the first ionization threshold. This type of Auger process is called *resonant* Auger decay or *autoionization* (see fig. 2.1(i)-(k)). Note further that the system is not necessarily in its ground state after a first Auger decay, and that subsequent Auger decays (*Auger cascades*) are possible, which lead to multiply charged ionic final states (see chapter 2.2).

For a more detailed discussion of the atomic photoionization processes, I refer the interested reader to the extensive literature.[17,19–23,25,33–35]

2.2 Molecular Photoionization and Photofragmentation

The processes which have been described so far apply in a similar way to both atomic and molecular systems. They are usually explained for the atomic case where they can in general be understood easier due to the much simpler electronic structure. Fundamentally different and typical *molecular* features are all effects that are in the broadest sense based on the existence of more than one nucleus and/or a chemical bond. In quantum mechanical terms, generalizing from atomic to molecular systems results in two major changes:[37–40]

- The spherical symmetry of the Coulomb potential is broken, and even in the independent electron approximation, the orbital angular momentum l of the electron is not a good quantum number any more. For diatomic molecules, its component m_l with respect to the molecular axis still remains a good quantum number.
- In addition to the electron-nucleus and electron-electron interactions, the freedom of movement of the nuclei relative to each other contributes to the total Hamiltonian of the system.

While the first aspect is mostly taken into account by introducing *molecular orbitals* (MO), which are explained further in chapter 2.3, the second point leads to the vast field of rotational and vibrational excitations. The study of rotational and vibrational spectra represents its own big part of molecular physics and is mostly beyond the scope of this work.[e] However, certain aspects of the nuclear dynamics are important in particular in the context of isotope substitution (chapter 6) and are hence discussed in section 2.2.1 as well as Appendix C.

A related molecular phenomenon that plays a very important role in the experimental techniques applied in this work (see chapter 3) is the *photodissociation*. If a molecule is excited by the absorption of a photon with a photon energy above the *dissociation energy* of the molecule (usually in the range of a few eV), there is the possibility that the chemical

[e] For further information, I refer to the standard textbooks of molecular physics.[37–40]

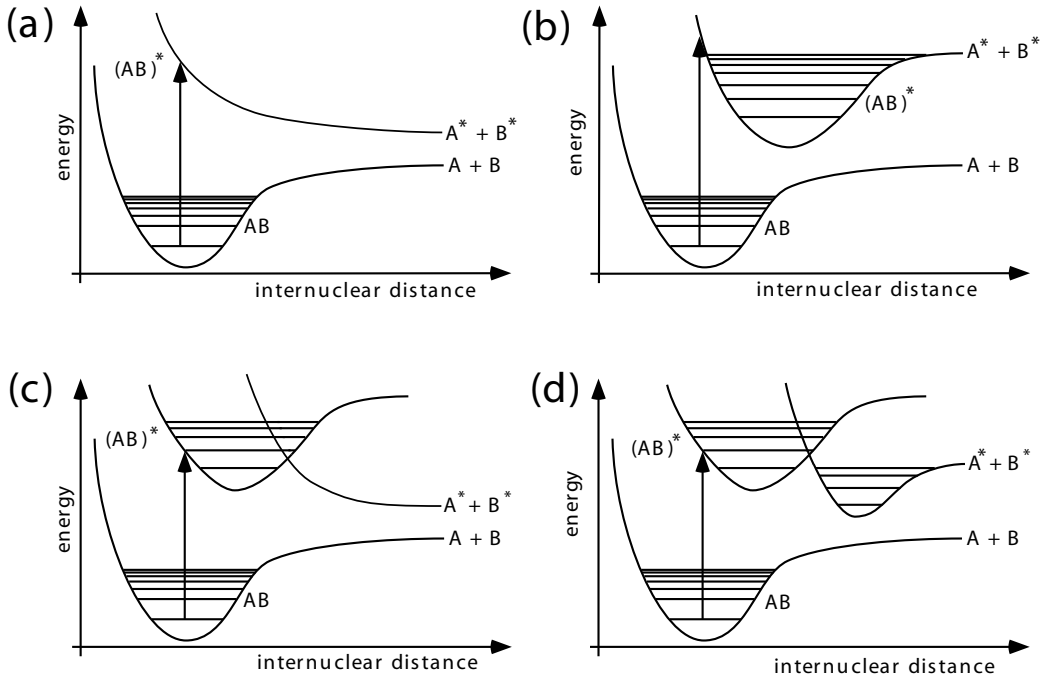

Figure 2.2: Schematic representation of the most common dissociation mechanisms after photoexcitation:[36] **(a)** excitation into anti-bonding orbital, **(b)** excitation into dissociation continuum of a bonding orbital, **(c)** predissociation into anti-bonding orbital, **(d)** predissociation into dissociation continuum of a bonding orbital. Note that the molecular fragments can be in an excited or ionized state after the dissociation.

bond is broken and the molecules fragments into several components. This process is therefore also called *photofragementation*. In most cases, a direct photoexcitation from the molecular ground state into the dissociation continuum of neutral, non-excited fragments is very unlikely due to selection rules and the Franck-Condon-principle (see chapter 2.2.1). Instead, the photoexcitation often leads to an excited molecular state which then dissociates directly (fig. 2.2(a),(b)) or via predissociation (fig. 2.2(c),(d)).[38] As the photon energy for an *inner-shell* photoionization is high above the dissociation threshold, there are usually several possible dissociation channels for a core-excited molecule.

Let me consider the dissociation of molecular nitrogen as an example, since N_2 is one of the showcase molecules in this work. After a *K-shell photoionization*,[f] the molecular ion is in a non-dissociative excited state $(N_2{}^+)^*$, which can then decay into a dissociative state via an Auger process:

$$N_2 + h\nu \rightarrow (N_2{}^+)^* + e^-_{Photo} \tag{2.4}$$

$$(N_2{}^+)^* \rightarrow N^+ + N^+ + e^-_{Auger}. \tag{2.5}$$

[f] The lowest molecular orbitals are usually very similar to the respective atomic orbitals (see chapter 2.3) and are therefore often referred to as *K-shell*.

However, alternative electronic decay channels to eq. (2.5) are

$$(\mathrm{N_2}^+)^* \rightarrow \begin{cases} \mathrm{N_2}^{++} + e^-_{Auger} \\ \mathrm{N}^{++} + \mathrm{N} + e^-_{Auger} \\ \mathrm{N}^{++} + \mathrm{N}^+ + 2e^-_{Auger} \\ etc. \end{cases} \tag{2.6}$$

2.2.1 Born-Oppenheimer Approximation and Franck-Condon-Principle

Because of the much greater mass of the nuclei compared to the mass of the electrons, the nuclei in a molecule move at much slower velocities than the electrons. To a first approximation, the motion of the electrons thus depends only on the location of the nuclei rather than on their velocity or momentum and can consequently be treated separately from the dynamics of the nuclei.[37–44] This is known as the *Born-Oppenheimer approximation*,[45] which allows to decouple the electronic and nuclear wave functions in the theoretical description of the molecule. The energy of a given molecular state is thus calculated for a *fixed internuclear distance R* which is then varied to obtain the *potential curves* that determine the nuclear motion (fig. 2.2 and 2.3). Between different states (i.e. different curves), only vertical transitions are possible, since electronic excitations and the reaction of the electron cloud are assumed to be fast enough to be considered *instantaneous* on the time scale of the slower nuclear motion (*Franck-Condon-principle*).[38–44] As the equilibrium internuclear distances of the electronically excited molecule is usually larger than in the ground state since the bond is usually weakened by the excitation, the corresponding potential curves are slightly shifted with respect to each other, and a vertical transition starting from the lowest vibrational state of the ground state can lead to several vibrational levels in the exited state (see fig. 2.3). The transition probabilities to the different levels, which are proportional to the overlap between the ground and final state wave functions within the Franck-Condon-region, are called *Franck-Condon-factors* and can be determined experimentally or calculated from the potential curves.

For most bound states, the potential curve near the minimum is very similar to a harmonic oscillator, and the vibrational states can be described by a simple quantum mechanical harmonic oscillator model (see chapter 6.1 and Appendix C). However, as the vibrational excitation increases, the anharmonicity increases and a *Morse potential*

$$V = D_e \left(1 - e^{-a(R-R_e)}\right)^2 \tag{2.7}$$

where D_e is the dissociation energy, R the internuclear distance, R_e the equilibrium distance, and a a constant that depends on the reduced mass, the dissociation energy and the oscillation frequency, is required to properly describe the higher vibrational states.[38,44] In

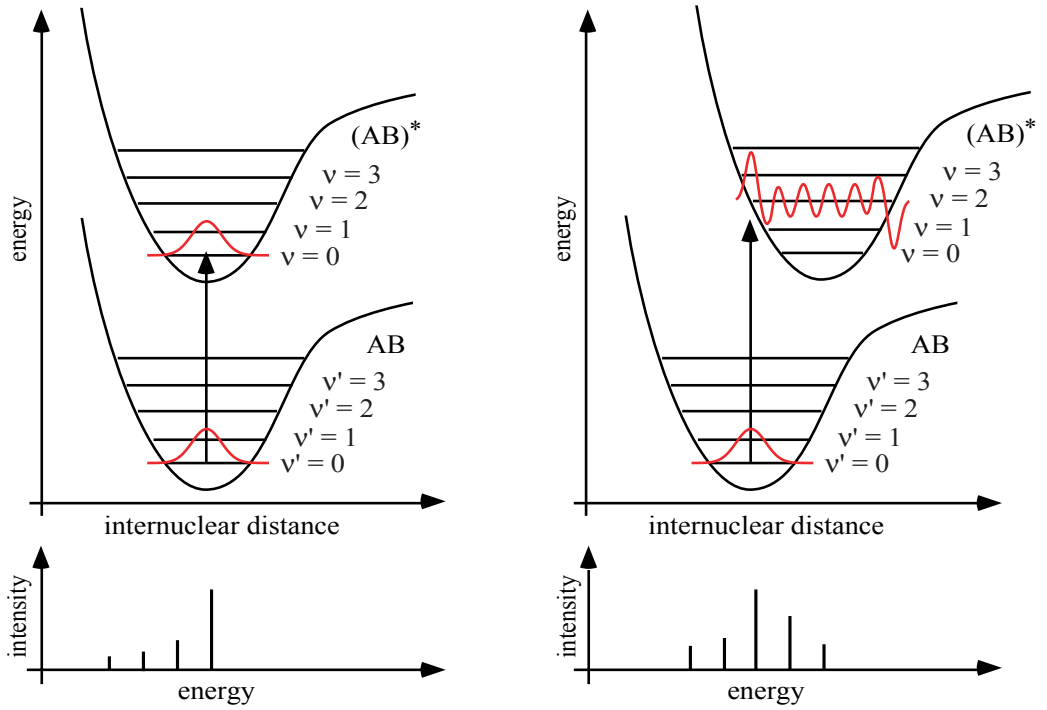

Figure 2.3: Schematic explantation of the Franck-Condon-principle: Electronic transitions are fast in comparison to the nuclear motion. Therefore, the internuclear distance does not change noticeably during these transitions, i.e. they occur *vertically* in the potential curve diagram. If the equilibrium internuclear distances of the ground and excited state are similar, excitations occur mostly between the two vibrational ground states, otherwise higher vibrational states are excited preferentially. The transition probability is highest where the overlap between the electronic wave functions is highest.

that case, the energy levels are given by the eigenstates of an *anharmonic* oscillator:

$$E_v = \hbar\omega \left(1 - c_a \left(v + \frac{1}{2}\right)\right) \left(v + \frac{1}{2}\right) \qquad v = 1, 2, 3, \ldots \tag{2.8}$$

Here, ω is the oscillation frequency for small amplitudes (i.e. given by the harmonic oscillator) and $c_a \ll 1$ is the constant of anharmonicity.

2.3 Molecular Orbitals

A common model for the conceptual understanding of molecular orbitals is the *Linear Combination of Atomic Orbitals* (LCAO) method[38–42] in which the molecular orbitals are expressed as linear combinations of the original atomic states in the independent atoms. A schematic explanation of this model is illustrated on the example of the simplest molecule, H_2, in fig. 2.4. In this *homonuclear* molecule, the two originally degenerate H(1*s*)-states form two molecular orbitals with different symmetry, which are called *gerade* and *ungerade* (referring to their inversion symmetry) or *bonding* and *anti-bonding*. The latter terms describes the fact that the gerade combination lowers the total energy of the system and consequently has bonding character, while the ungerade state is energetically unfavorable

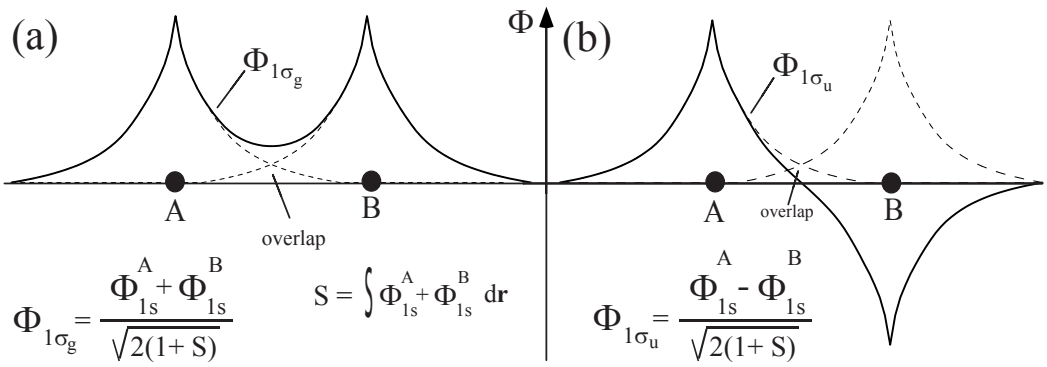

Figure 2.4: Schematic explanation of the LCAO model on the example of the H_2 molecule: wave function of the **(a)** gerade (i.e. bonding) and **(b)** ungerade (i.e. anti-bonding) $H_2(1\sigma)$ state.

and does not produce a stable molecule.[g] The energy difference between the gerade and ungerade state depends the *overlap* of the two atomic (1*s*)-states (see fig. 2.4).

Since this work focusses on K-shell photoionization of CO and N_2, let me discuss these two molecules and the respective orbitals in a little more detail: In the homonuclear molecule N_2, the two equivalent nitrogen atoms give rise to two almost degenerate core orbitals corresponding to the symmetric and antisymmetric linear combination of the atomic 1*s* orbitals. Similar to the case of H_2, these orbitals are called $1\sigma_g$ and $1\sigma_u$ referring to their inversion symmetry. The very small binding energy difference between these gerade and ungerade states has recently been measured in the photoelectron spectrum by Hergenhahn *et al.*[46] with the experimentally determined splitting of $\Delta E_{g/u} \approx 97\,\mathrm{meV}$ being in good agreement with theoretical results from LCAO and *Hartree-Fock* (HF) calculations.[47,48 h] As the overlap between the two atomic N(1*s*) orbitals is obviously extremely small, the two $N_2(1\sigma)$ orbitals can be described to a very good approximation as

$$\Phi_{1\sigma_g} \approx \frac{1}{\sqrt{2}}(\Phi_{1s}^{A} + \Phi_{1s}^{B}) \tag{2.9}$$

and

$$\Phi_{1\sigma_u} \approx \frac{1}{\sqrt{2}}(\Phi_{1s}^{A} - \Phi_{1s}^{B}) \,, \tag{2.10}$$

where Φ_{1s}^{A} and Φ_{1s}^{B} are the atomic 1*s* wave functions of atom A and B.[47,48]

Heteronuclear molecules like CO do not have inversion symmetry. Their lowest molecular orbitals are usually clearly separated in binding energy and very similar to the localized atomic orbitals, in this case to the O(1*s*) and C(1*s*) orbitals. Fig. 2.5 shows the energy eigenvalues (i.e. binding energies) of the molecular orbitals in molecular nitrogen (N_2) and

[g] In the more general case of molecules with more than one occupied orbital, one finds that the bonding state *strengthens* the chemical bond while the anti-bonding state *weakens* it.

[h] For the explicit and more precise calculation of molecular orbitals, *Self Consistent Field* (SCF) methods like the *Hartree-Fock* method[49] are often used.[50,51] For a general introduction to this approach, see standard quantum chemistry textbook.[38–42] An alternative method to obtain both bound and continuum states in a molecular system is the *Multiple Scattering* (MS) method,[52] which is described in Appendix B.

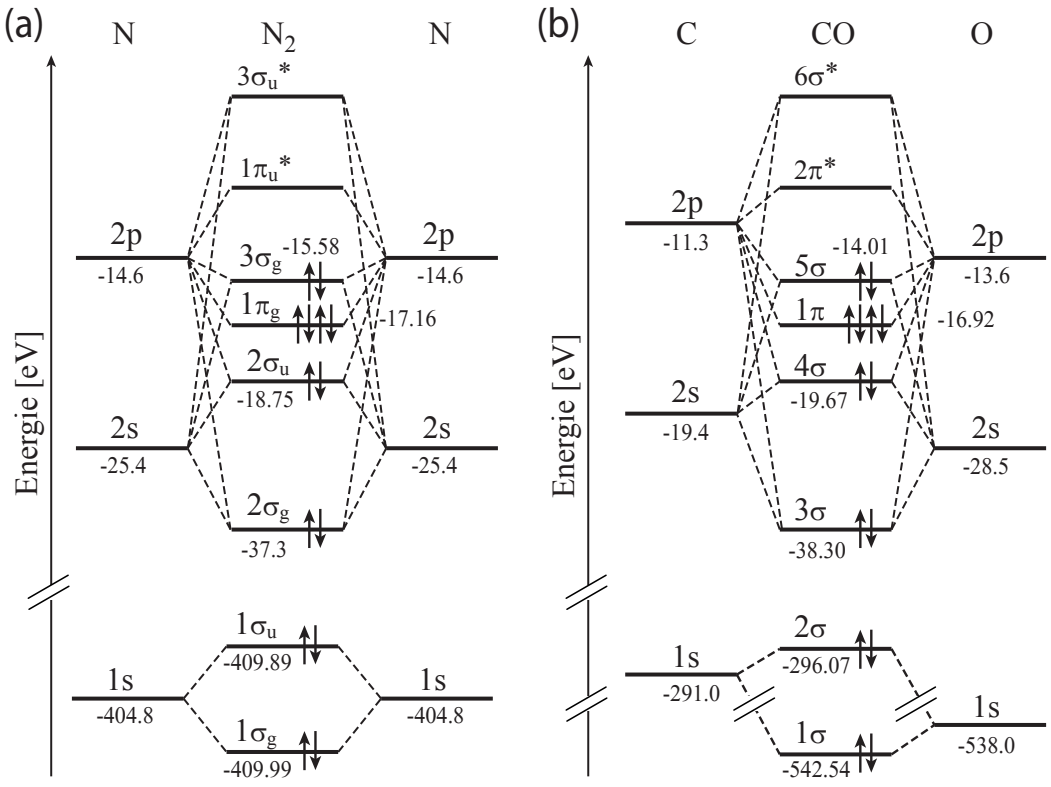

Figure 2.5: Molecular orbitals of the N_2 **(a)** and CO molecule **(b)** in the LCAO model together with their electronic ground state occupation. Molecular binding energies are taken from Hemmers[35] and Hergenhahn ,[44] atomic binding energies are based on calculations by Verner *et al.*[53]

carbon monoxide (CO) compared to the respective atomic orbitals.

The electronic ground state configuration of N_2 (fig. 2.5(a)) is

$$1\sigma_g^2\ 1\sigma_u^2\ 2\sigma_g^2\ 2\sigma_u^2\ 1\pi_u^4\ 3\sigma_g^2 \tag{2.11}$$

and has ${}^1\Sigma_g^+$ symmetry. The electronic ground state configuration of CO (fig. 2.5(b)) is

$$1\sigma^2\ 2\sigma^2\ 3\sigma^2\ 4\sigma^2\ 1\pi^4\ 5\sigma^2 \tag{2.12}$$

and has a ${}^1\Sigma^+$ symmetry.[i]

Except for the perturbations induced by the different nuclear charges in CO and the additional symmetry of the N_2 molecule, CO and N_2 have very similar molecular orbitals since they are *isoelectronic*. Hence, they are a good showcase to point out effects which are particularly sensitive to small differences in the electrostatic potential or to the inversion symmetry (see chapter 5 and 6).

[i] For further details about molecular orbitals and molecular states as well as for an explanation of the most common notations, please refer to the references.[35,37–42]

2.4 Cross Sections and Angular Distributions

2.4.1 Total and Partial Cross Sections

The experimentally measurable quantities that contain the information about the probability of a particular photoionization process are the *cross sections*. From a theoretical point of view, they are based on the *transition matrix elements*: For the interaction of a quantum mechanical system with an electromagnetic field, the transition probability W_{if} from an initial state Ψ_i with the energy eigenvalue E_i into a final state Ψ_f with the energy eigenvalue E_f can be obtained from *Fermi's Golden Rule*[54]

$$W_{if} = \frac{2\pi}{\hbar} \mid <\Psi_f|\hat{H}_{rad}|\Psi_i> \mid^2 \delta(E_f - E_i - h\nu), \tag{2.13}$$

where $\hat{H}_{rad}$ is the Hamiltonian describing the electromagnetic field and $<\Psi_f|\hat{H}_{rad}|\Psi_i>$ is the transition matrix element.[j] In the dipole approximation, the *partial cross section* of the respective transition is then given by[55]

$$\sigma_{if}(h\nu) = \frac{4\pi^2 \alpha\, a_0^2}{3}\, h\nu \mid <\Psi_f| \sum_\mu \mathbf{r}_\mu |\Psi_i> \mid^2. \tag{2.14}$$

Here, α is the fine structure constant, a_0 the Bohr radius, and $<\Psi_f|\sum_\mu \mathbf{r}_\mu|\Psi_i>$ the dipole matrix element (in length form).[k]

The partial cross section is measured rather straightforwardly in modern photoelectron spectroscopy experiments[55] and describes the photoionization process for a particular *subshell* of the atom or molecule. The *total photoionization cross section*

$$\sigma(h\nu) = \sum_{i,f} \sigma_{if}(h\nu) \tag{2.15}$$

indicates the total ionization probability of the system (also as a function of the photon energy). It can be determined experimentally for example via ion yield measurements.[56]

Fig. 2.6 shows the photoabsorption spectrum of CO and N_2 in the region of the carbon respectively nitrogen K-edge. Below the photoionization threshold of 296.1 eV (for CO) and 409.9 eV (for N_2), several sharp resonances can be seen. They correspond to excitations of a K-electron into the anti-bonding $2p\pi^*$ orbital (π^*-*resonance*) and into Rydberg states, often followed by an autoionization.[57–60] Another very interesting feature in the K-shell photoionization of small molecules is the appearance of a *shape resonance* (σ^*-*resonance*) in the continuum.[23,61] An illustrative way of explaining this resonance was proposed by Dehmer *et al.*,[62,63] who attributed it to a temporary trapping of ejected elec-

[j] The index *"rad"* in this notation simply refers to the electromagnetic field and shall not be confused with *radial* matrix elements for instance.

[k] For higher order transitions, the dipole operator $\sum_\mu \mathbf{r}_\mu$ has to be replaced by the appropriate term of the multipole expansion of $\hat{H}_{rad}$[26] as explained in chapter 2.4.3.

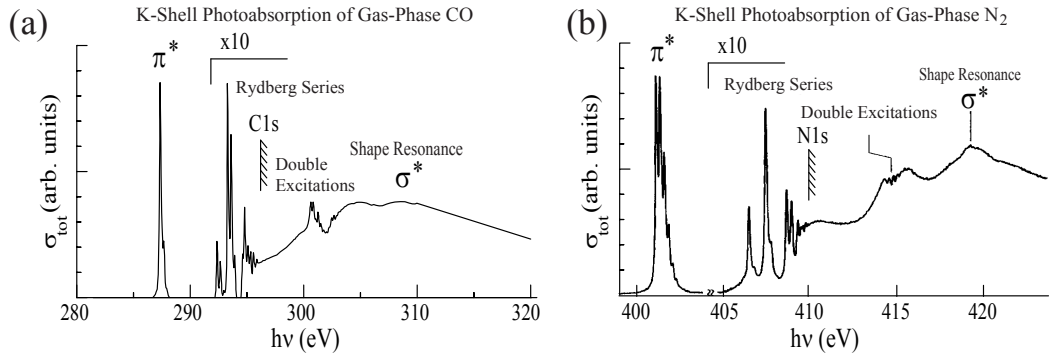

Figure 2.6: High resolution photoabsorption spectrum in the region of **(a)** the carbon K-edge of CO[57] and **(b)** the nitrogen K-edge of N_2.[58]

trons caused by a *centrifugal barrier* in the molecular potential. Alternatively, the shape resonance can be understood as a promotion of the core electron in the anti-bonding σ^* molecular orbital with a subsequent decay into the continuum.[50,64–66] A more detailed discussion of the shape resonance with an emphasis on its scattering aspects is presented in chapter 4.3.

2.4.2 Differential Cross Sections and Angular Distributions

The measurement of partial photoionization cross sections does not allow to differentiate between the different angular momentum components (*partial waves*) of the outgoing photoelectron since they are energetically degenerate. More parameters have to be measured in order to obtain more detailed information on the partial waves. *Differential cross sections* are used to describe the behavior of the partial cross section as a function of these other parameters. For example, the *photoelectron angular distribution* $d\sigma_{if}/d\Omega$ indicates the probability that an electron is emitted in a certain direction in space (i.e. in a certain solid angle element $d\Omega$). For *randomly* oriented molecules in the gas phase and within the framework of the dipole approximation, this angular distribution can be characterized by only one additional parameter, the *asymmetry parameter* β:[67]

$$\frac{d\sigma_{if}(h\nu)}{d\Omega} = \sum_{l=0,2} A_l \, P_l(cos\theta_e) = \frac{\sigma_{if}(h\nu)}{4\pi}[1 + \beta(h\nu)\, P_2(\cos\theta_e)] \, . \tag{2.16}$$

Here, Ω is the solid angle, $P_2(cos\theta_e)$ is the 2^{nd}-order Legendre polynomial

$$P_2(\cos\theta_e) = \frac{3}{2}\cos^2\theta_e - \frac{1}{2} \tag{2.17}$$

and the photoelectron emission angle θ_e is measured with respect to the polarization vector of the light $\boldsymbol{\varepsilon}$.[1]

[1]For unpolarized light, θ_e is measured with respect to the momentum-vector of the incoming photon and the angular variation is only half as pronounced as for linearly polarized light.[33,35]

From the energy dependence of the asymmetry parameter β, some information about the dynamical behavior of the different partial waves can be obtained.[50,55,68,69]

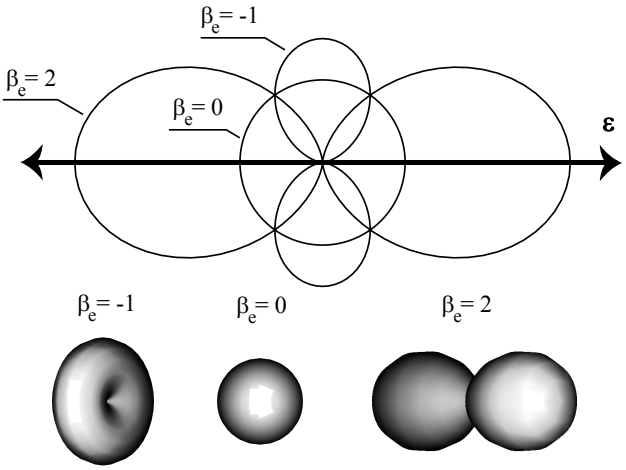

Figure 2.7: Electron angular distribution from randomly oriented molecules for different values of the asymmetry parameter β.

An equivalent expression to eq. (2.16) can be derived for the *photoion* angular distribution from randomly oriented molecules, where the asymmetry parameter β (sometimes also called β_e to avoid confusion) has to be replaced by the asymmetry parameter of the molecular photo-excitation β_m (also called *molecular alignment parameter*).[35,70,71]

The photoion angular distribution closely reflects the fact that the photoexcitation probability depends on the orientation of the molecular axis with respect to the polarization direction of the light. Precisely speaking, it is the symmetry of the *charge density* with respect to the molecular axis that causes the different photoexcitation probabilities, since the electromagnetic field (i.e. the $\boldsymbol{\varepsilon}$-vector) acts on these charge densities. Referring to the symmetry of the initial and final states, one distinguishes e.g. for the CO and N_2 K-shell photoionization between $\Sigma \rightarrow \Sigma$-transition (for the transition from an initial state with Σ-symmetry into a final state with Σ-symmetry), and $\Sigma \rightarrow \Pi$-transition (for the transition from an initial state with Σ-symmetry into a final state with Π-symmetry). Within the dipole approximation, for linearly polarized light with the $\boldsymbol{\varepsilon}$-vector *parallel* to the molecular axis, only $\Sigma \rightarrow \Sigma$-transitions are possible, while for a light polarization *perpendicular* to the molecular axis, only $\Sigma \rightarrow \Pi$-transitions are allowed.[70]

2.4.3 Nondipole Effects

For many decades, it was believed that the photoionization of atoms and molecules at photon energies below 1 keV is well described by the dipole approximation. However, as experimental techniques evolved and the precision of measurements improved, it turned out that even for photon energies in the range of several ten to hundred eV, electric quadrupole ($E2$) and magnetic dipole ($M1$) corrections can be important.[72] While the dipole approximation holds for the angle-integrated total and partial cross sections to which only the squares of the transition matrix elements contribute,

$$\sigma_{tot} \propto (E1)^2 + (E2)^2 + (M1)^2 + \ldots \; . \tag{2.18}$$

the differential cross sections (i.e. photoelectron angular distributions) can be strongly affected by the nondipole contributions. The reasons are cross-terms between the dipole and nondipole channels, which can, under certain conditions, be in the same order of magnitude as the leading dipole term:

$$\frac{d\sigma}{d\Omega} \propto E1 \otimes E1 + E1 \otimes E2 + E1 \otimes M1 + \ldots \; . \tag{2.19}$$

In that case, higher order nondipole corrections have to be included in eq. (2.16).[72,73] In the most commonly used notation, the differential photoionization cross section including the first-order nondipole contributions which arise from the interference between dipole and quadrupole photoionization channels, is given by[74]

$$\frac{d\sigma(h\nu,\theta_e,\phi_e)}{d\Omega} = \frac{\sigma(h\nu)}{4\pi}[1 + \beta(h\nu)\, P_2(\cos\theta_e) + (\delta(h\nu) + \gamma(h\nu)\cos^2\theta_e)\sin\theta_e\cos\phi_e] \; . \tag{2.20}$$

In this first-order correction, the angular distribution depends also on the azimuthal angle ϕ, and two additional *nondipole asymmetry* parameters, δ and γ, are necessary to describe the full angular distribution. However, for $\phi = 0$, i.e. in the plane perpendicular to the light propagation direction, the so-called *dipole plane*, the additional terms in eq. (2.20) vanish and the angular distribution takes the form of eq. (2.16) again.

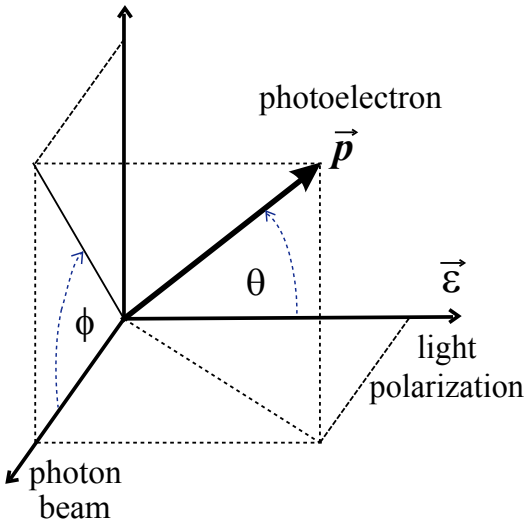

Figure 2.8: Geometry for nondipole angular distributions.

A non-zero δ and γ leads to a forward-backward asymmetry in the electron emission resulting in a net flux of electrons parallel or antiparallel to the photon propagation direction. The integrated flux can be measured as a macroscopic current called drag current.[75] First successful measurements have recently been performed on a variety of gases such as neon, xenon, and nitrogen and their results will be published soon.[76] They show that drag current can be a non-negligible electron transport process even at low photon energies where it has previously been disregarded. This may be of importance to fields such as astrophysics or physics of the upper planetary atmosphere.

Going beyond the dipole approximation could also be important when studying coherence effects in homonuclear molecules (see chapter 5), as the approximation of a *small initial state* (*small* compared to the wavelength of the incident light) is not necessarily fulfilled if the initial state is delocalized over two atoms.[77] In that case, an additional phase shift accounting for the path length difference between the two atoms might have to be in-

troduced as discussed in section 5.1. First experimental observations of nondipole effects in the photoelectron angular distribution of randomly oriented as well as fixed-in-space N_2 have been reported recently.[73,78] However, their exact origins remain an interesting question for theory and future experiments.

2.4.4 Photoelectron Angular Distributions from Fixed-in-Space Molecules

The photoelectron angular distribution of molecules with a *fixed molecular orientation* is a highly differential quantity which allows to obtain additional information on the dynamic behavior of the photoelectron partial waves lost in the photoelectron angular distributions from randomly oriented molecules.[79,80] Early multiple scattering calculations by Dan Dill, Jon Siegel, J.L. Dehmer, and James Davenport from the 1970s predicted a rich structure in photoelectron angular distributions of oriented diatomic molecules due to the enhancement of partial waves with high ($l \geqq 3$) angular momentum caused by the scattering of the photoelectron in the anisotropic molecular potential.[80,81] These structures are generally not observable in conventional molecular photoionization experiments on *free* molecules due to the random orientation of the molecules in the gas phase which averages out the angle-dependent intensity variations. Formally, the electron angular distribution of an oriented molecule is a *triply differential cross section* (TDCS): the partial cross section is given as a function of the electron emission angles θ_e,ϕ_e and the orientation of the molecule, i.e. the angle θ_m between the molecular axis and the light-polarization vector $\boldsymbol{\varepsilon}$ (or the photon momentum in the case of circularly polarized light). However, the term TDCS is generally not used in this case,[m] and one simply speaks of the photoelectron angular distribution from *oriented* or *fixed-in-space* molecules or of *molecule frame photoelectron angular distribution* (MPAD).[n] In the most general case, the MPAD can be described by an expansion in terms of spherical harmonics Y_{lm}

$$\frac{d\sigma}{d\Omega} = \sum_{l,m} A_{lm}\, Y_{lm}(\Omega). \tag{2.21}$$

For *cylindrically symmetric* molecules and linearly polarized light with the $\boldsymbol{\varepsilon}$-vector parallel to the molecular axis, eq. (2.21) reduces to

$$\frac{d\sigma}{d\Omega} = \sum_{l} A_l\, P_l(cos\theta_e). \tag{2.22}$$

The physical interpretation of the expansion coefficients A_{lm} respectively A_l was first explained by Dill *et al.*[79,80] who derived their relation to the *dipole matrix elements* and *relative phase shifts* among different partial waves. While mathematically, both sums go

[m] A more typical application of the term TDCS is e.g. the study of double-photoionization processes where the cross section is measured as a function of the emission angles of both electrons.[21,22]

[n] In the original paper by Dill *et al.*, they are also referred to as *fixed-molecule angular distributions* (FMAD's).[80]

up to infinity, one finds that they often converge rather rapidly and the coefficients become negligible for $l \gtrsim 10$. Eq. (2.22) is therefore commonly used to fit the experimental angular distribution patterns.[82–91] A more sophisticated analysis extracting the actual dipole matrix elements and phase shifts from the experimental data is also possible and allows so-called *complete photoionization experiments*, which are described in the next section.

2.5 Complete Photoionization Experiments

The term *complete* experiment is used to describe an experiment from which one can extract *all* the values necessary for a complete theoretical description of a certain process.[92] Since every theoretical description is valid within some approximation, the concept of a complete experiment is only valid within the same approximation as well. If the discussion of photoionization experiments is restricted to the electric dipole approximation, a complete photoionization experiment means the determination of all the dipole matrix elements and relative phase shifts among different partial waves from the measured data.[93–103]

The first complete experiments were discussed and performed for atoms,[93–95] where the dipole selection rules restrict the number of partial waves to only two ($l = l_i \pm 1$, where l_i is the angular momentum of the initial state). Including relativistic effects (i.e. spin-orbit interaction), at most five parameters describe the photoionization process in the simplest case of a closed-shell atom: Three dipole matrix elements corresponding to the transition from an initial state nlj (with $j = l \pm 1$) to the photoelectron final states with $(l-1)(j-1)$, $(l \pm 1)j$, and $(l+1)(j+1)$, and two phase shift differences between these three partial waves.

As explained above, the orbital angular momentum l is *not* a good quantum number in the case of a molecule due to the non-spherical nature of the molecular potential. Thus, the photoelectron wave functions can be represented only as an infinite expansion in spherical harmonics (with the origin at the center of mass). As the partial-wave expansions for both bound and continuum state wave functions are converging rather rapidly, one can truncate the summation to a good approximation after a limited number of terms (see section 2.4.2). In this more restricted sense, complete experiments are also feasible for molecules [86–88, 101–103] and have been realized very recently.[104–106] For a complete determination of all matrix elements and phases, it is necessary to measure the angular distributions for parallel and perpendicular orientation of the molecular axis, i.e. for pure $\Sigma \rightarrow \Sigma$- and $\Sigma \rightarrow \Pi$-transitions, as well as in an additional geometry or with circularly polarized light in order to determine the relative phase between the Σ- and Π-continua.[103]

Chapter 3

Photoelectron Spectroscopy of Randomly Oriented and Fixed-in-Space Molecules

The experiments presented in this work were performed with synchrotron radiation in the vacuum ultra-violet (VUV) range using multiple electron time-of-flight analyzers either operated in conjunction with a momentum-resolving ion time-of-flight spectrometer in order to record angle-resolved photoelectron-fragment ion coincidences or operated without the ion spectrometer in order to record non-coincident angle-resolved photoelectron spectra. As many of the components have already been described extensively in previous works,[22,106–109] this chapter introduces them rather briefly while emphasizing the changes and improvements made over previous setups. For a more detailed description of the individual components, I refer to the above-mentioned works as well as the references given in the respective paragraphs.

3.1 Electron and Ion Time-of-Flight Spectroscopy Using Synchrotron Radiation

When studying core photoionization processes of small atoms and molecules, a tuneable light source emitting radiation in the VUV range between 10 eV and 1 keV or more is highly desirable, and a synchrotron radiation facility such as the *Hamburger Synchrotronstrahlungslabor (HASYLAB)*, the *Berliner Speicherring Gesellschaft für Synchrotronstrahlung (BESSY)* or the *Advanced Light Source (ALS)* in Berkeley is therefore often the first choice. In these facilities, a beam of relativistic electrons or positrons very close to the speed of light is traveling on a closed orbit inside a storage ring optimized to emit very high-intensity VUV-radiation.[12,13] Usually, the radiation is created either in one of the *bending magnets* that keep the stored particles on their (almost) circular orbit or in a special

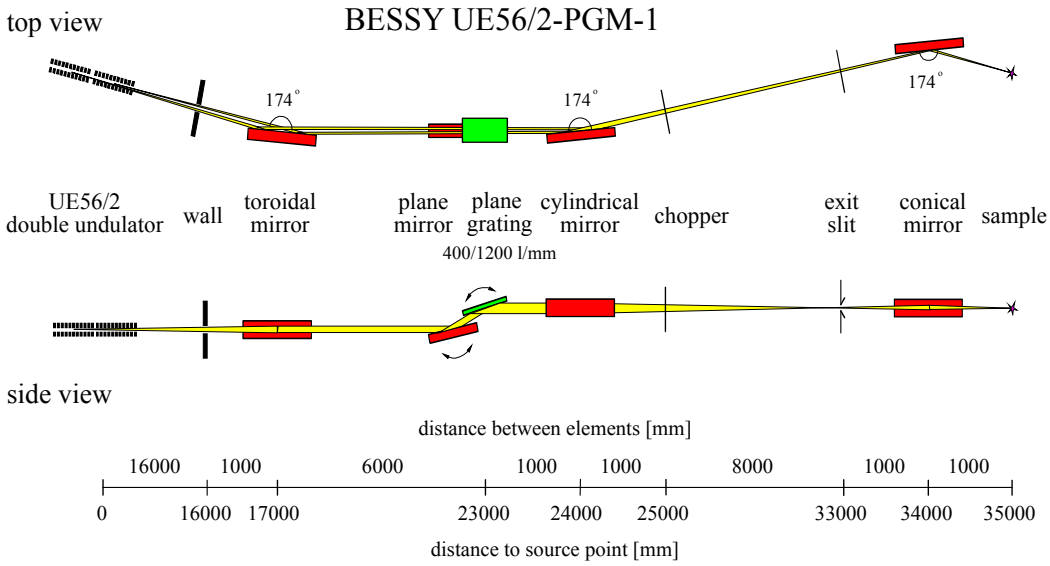

Figure 3.1: Schematic layout of UE56/2-PGM-1 beamline at BESSY.[111,112]

insertion device called *wiggler* or *undulator*. These consist of a periodic magnetic structure that forces the particle beam on an undulating trajectory, hence emitting high-intensity, polarized radiation into a very small forward cone.[12,13] All experiments in this work were performed on such an undulator beamline, namely BW-3 at HASYLAB, equipped with two interchangeable plane undulators,[110] and UE56/2 respectively UE56/1 at BESSY (see fig. 3.1), each featuring a Sasaki type elliptically polarizing undulator.[111,112]

Although an undulator emits an already much narrower spectral distribution than a bending magnet, the undulator radiation is sent through a monochromator, in the above cases a modified SX-700 plane grating monochromator (PGM),[110–112] in order to obtain the high photon energy resolution (typically below 100 meV at a photon energy of 400 eV) which is required by most state-of-the-art experiments.[a]

Once the monochromatized VUV radiation enters the experimental chamber which, for most gas-phase applications, has to be decoupled from the ultra high vacuum of the beamline via a *differential pumping section*, it interacts with the target, in this case an effusive gas jet, and creates electrons and ions which can then be detected. A very common approach for measuring the kinetic energy of the electron and/or the fragment ions is the time-of-flight (TOF) technique. The basic idea behind this method is that the trajectory and the velocity of a charged particle in a given electric field is determined by its mass m, charge q, and initial kinetic energy E. In particular, when passing though a region with *constant electrostatic potential* (usually called *drift tube*), the time-of-flight t of a given particle is proportional to $1/\sqrt{E}$. Consequently, the kinetic energy of the particle can be determined by measuring the time the particle needs to reach the detector. The advantage of the TOF spectrometry compared to *energy dispersive* methods (e.g. using hemispherical

[a] For a general introduction into synchrotron radiation experiments as well as a detailed technical description of the beamlines, I refer to the extensive literature[12,13] and to the special publications.[110–112]

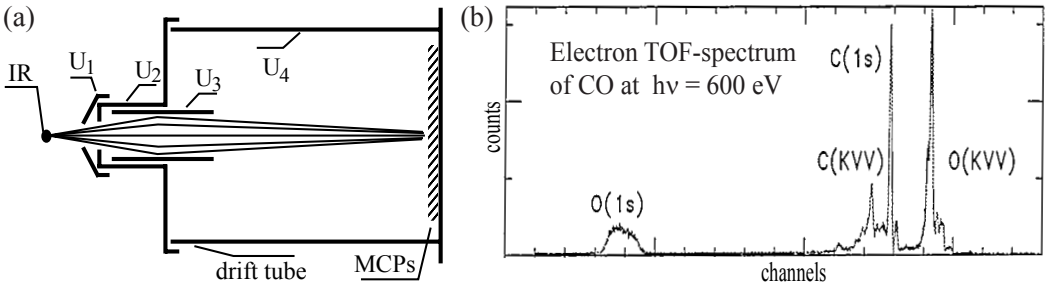

Figure 3.2: (a) Schematic model of an electron time-of-flight spectrometer.[36] **(b)** Example of an electron TOF spectrum of CO taken at a photon energy $h\nu = 600\,\mathrm{eV}$.[113]

analyzers) is that particles with different kinetic energies can be detected simultaneously since they arrive at the detector at different times. In turn, the time-of-flight technique is only applicable if the particles are not generated continuously, but rather by a pulsed light source for instance, and if the interval between two light pulses is longer than the maximum spread in flight time due to the different kinetic energies so an unambiguous relation between time-of-flight and initial kinetic energy is guaranteed.

Hence, synchrotron radiation from dedicated synchrotron radiation facilities is very well suited for time-of-flight experiments, since the electrons respectively positrons in the storage ring are not distributed continuously but grouped in *bunches* and the synchrotron radiation generated by these bunches is therefore pulsed. Most synchrotron light sources even offer a special *reduced bunch mode* dedicated to users with time-of-flight applications, during which less bunches are injected in the storage ring than in the regular *multi-bunch mode* in order to make a longer time window available for the measurement. For example, HASYLAB offers a *two bunch mode* in which only two positron bunches circle in the storage ring with an interval of roughly 480 ns in between them, while BESSY offers a *single bunch mode* with a 800 ns period.

Fig. 3.2(a) shows a schematic model of an electron time-of-flight spectrometer.[22, 33, 36, 114] The electrons are produced in the *interaction region*, where the light ionizes the target molecules. Depending on their initial kinetic energy and on the required energy resolution, electrons flying in the direction of the TOF spectrometer can be accelerated or retarded by the electrostatic field of one or several electrodes, in order to increase the resolution for fast electrons or to obtain higher transmission for electrons with low kinetic energy. At the end of the drift tube, the electrons are detected via a stack of *multi-channel plates (MCPs)*. As an example, the electron time-of-flight spectrum for the photoionization of CO at a photon energy $h\nu = 600\,\mathrm{eV}$ is shown in fig. 3.2(b). Time-of-flight peaks corresponding to photoelectrons produced by the (direct) photoionization of the O(1*s*) and C(1*s*) orbitals can be seen as well as Auger and satellite lines. At the chosen retarding voltage, the O(1*s*) photo line at a kinetic energy of 57 eV is well separated from other lines, while C(1*s*) and Auger electrons have a much higher kinetic energy and consequently appear in the spectrum with comparably small time-of-flight differences. A higher retarding voltage would cut out the O(1*s*) line, but would allow to properly resolve the C(1*s*) and/or the Auger lines.

3.2 Angle Resolved Electron and Ion Spectroscopy

A typical electron TOF spectrometer as shown in fig. 3.2(a) has a rather small acceptance angle in the order of a few degrees corresponding to a solid angle of roughly $4\pi/2000$ (for an acceptance angle of $\pm 2.5°$). Consequently, it is well suited for *angle resolved spectroscopy* in the sense that it detects only electrons emitted in the solid angle covered by the spectrometer. If several electron TOF spectrometers are used or one spectrometer is rotated into several positions, the electron intensity for different emission angles can be measured.[55]

In the same way, a regular ion TOF spectrometer can also be used to detect fragment ions emitted into a certain direction in space.[115,116] More advanced instruments for angle resolved ion spectroscopy use *imaging* ion TOF spectrometers, which cover the full 4π solid angle and measure not only the ion times-of-flight but also the ion hit positions via a *position sensitive multi-hit anode*. From the time-of-flight information in combination with the anode hit positions, it is possible to deduce the *initial momenta* and charges of the fragment ions and thereby derive both their kinetic energy as well as their emission direction. For a diatomic molecule, this corresponds to the spatial orientation of the molecular axis at the time of the fragmentation and, under the assumption of the *axial recoil approximation* (see section 3.3), also at the time of the ionization.[83,117–120] However, a crucial condition is that to a certain order, the time-of-flight is independent of the exact position where the ions are produced. If the size of the interaction region is in the order of one to a few millimeters, the time-of-flight differences due to different starting positions would otherwise cover to some extend the effect of the different initial momenta. An appropriate choice of voltages for the *ion extraction field* and the *drift tube* known as *Wiley-McLaren condition* can compensate this influence of the starting position, and hence allow an unambiguous determination of the momenta also for an extended interaction region.[121]

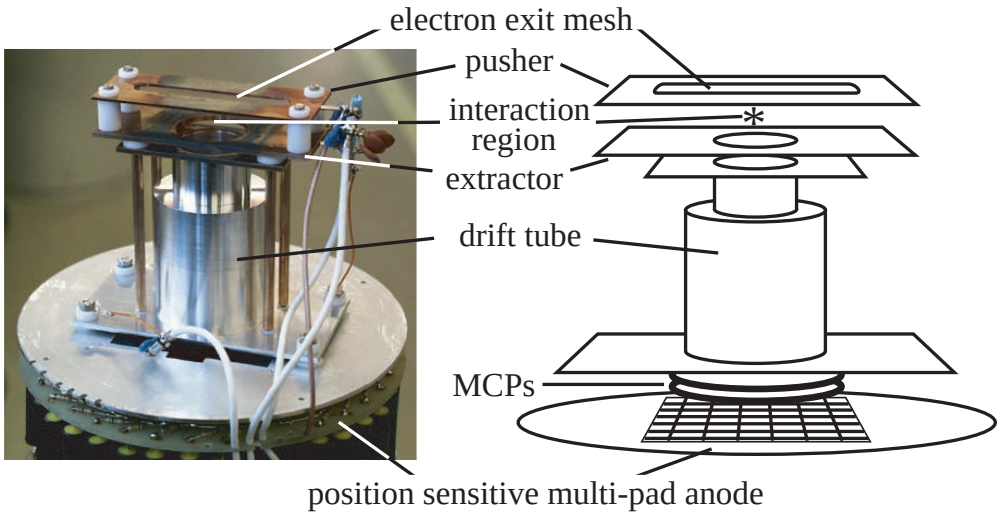

Figure 3.3: Photograph and schematic setup of the angle resolved ion TOF spectrometer ARFMADS.[108]

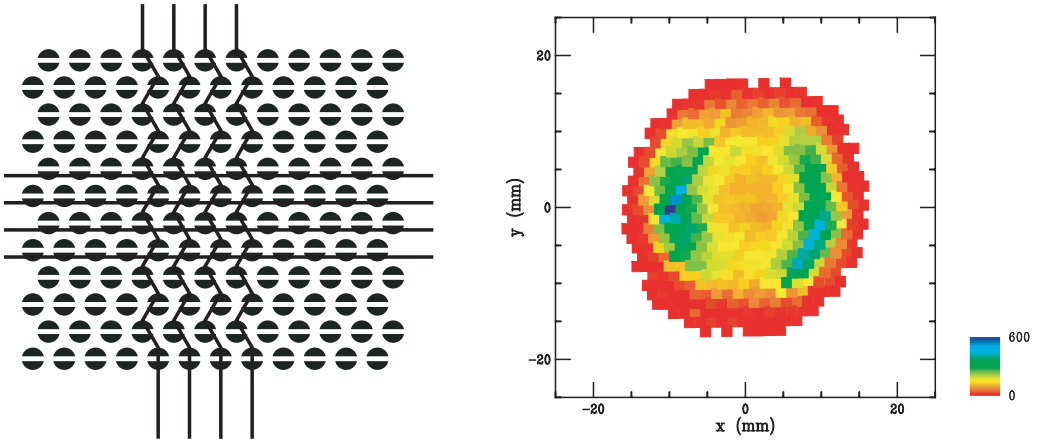

Figure 3.4: Schematic drawing of the position sensitive crossed-wire/multi-pad anode (left) and a typical anode pattern showing the fragmentation of a diatomic molecule (right). The distance of two neighboring pads on the anode is 1.46 mm, giving rise to a spatial resolution of about 0.5 mm when interpolating between pads.[122]

Fig. 3.3 shows a photograph and the schematic setup of a position sensitive ion TOF spectrometer, the *Angular Resolved Fixed Molecule Angular Distribution Spectrometer (ARFMADS)* which was used for this work. The ions are produced in the interaction region situated between the *pusher* and the *extractor* electrodes. A static or pulsed high voltage applied to these electrodes accelerates the ions into the *drift tube*, where they travel in a constant electric potential until they hit a stack of *multi-channel plates*. The ion impact produces a cloud of secondary electrons in the MCPs which are detected on the fast multi-hit capable *position sensitive anode* (fig. 3.4). A *reflection mesh* above the MCPs prevents secondary electrons from leaving the detection zone and being accelerated by the drift tube potential back into the interaction region. Otherwise, they could ionize other molecules or cause a background noise in the electron analyzers which are often used together with the ARFMADS.

In the current version of the ARFMADS, the position sensitive anode consists of a circular array of electrode pads arranged in dense packing with a distance of 1.46 mm to the nearest neighbor. The pads are connected by a grid of 29 times 35 wires in a *crossed-wire* scheme, so that the x and y coordinate of the ion hit positions can be determined along with the times-of-flight.[b] An alternative type of position sensitive anode is the *delay-line anode* which is used e.g in the COLTRIMS apparatus described in section 3.5.

[b] For further technical details and requirements, I refer the interested reader to the extensive description of the ARFMADS in the references.[36, 107, 122]

3.3 Angle Resolved Photoelectron-Photoion Coincidence Experiments

As mentioned in chapter 2.4.4, early multiple scattering calculations by Dan Dill, Jon Siegel, J.L. Dehmer, and James Davenport from the the 1970s predicted a rich structure in *molecular frame* photoelectron angular distributions (MPADs) from diatomic molecules.[80,81] These structures are generally not observable in conventional molecular photoionization experiments on *free* molecules due to the random orientation of the molecules in the gas phase which averages out the intensity variations. In the past, studies on *spatially oriented* molecules were only possible for molecules adsorbed on surfaces.[123–139 c] In that case however, the electronic structure of the molecules is altered by the additional chemical bond, the electron emission is affected by scattering on the surface,[140,141] and the electron emission angles are limited to the half-space above the surface.

Photoelectron-Photoion Coincidence Spectroscopy (PEPICO) is a well established spectroscopic tool widely used in synchrotron as well as laser applications. By measuring the photoelectron and the fragment ion(s) in coincidence, the detected particles can be attributed to *one* particular photoionization event, making it possible to determine e.g. the ionic final state of a given photoionization channel.[23,142] Combining this principle with the angle resolved spectroscopy techniques described in the previous section has recently created the *Angle Resolved Photoelectron Photo-Ion Coincidence technique (ARPEPICO)*.[82,83,106,109,143–146 d] If the *rotation time* of the molecule is much larger than the

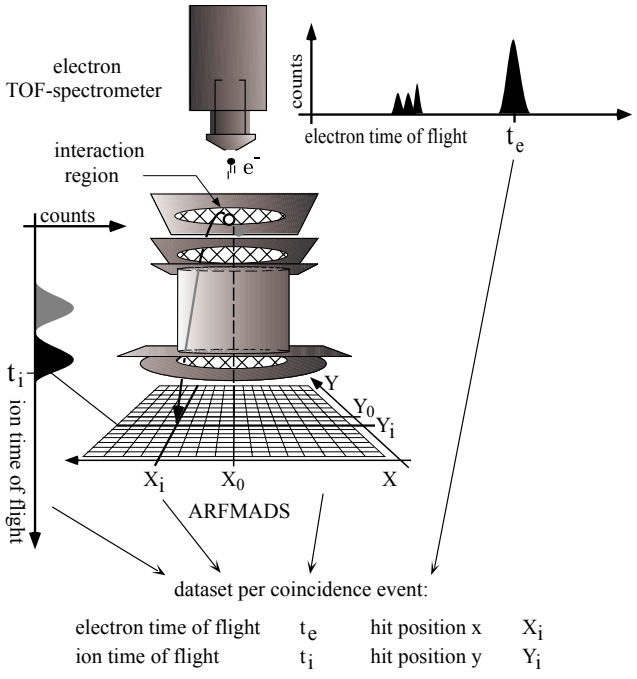

Figure 3.5: Schematics of angle resolved electron-ion coincidence experiment using the ARFMADS and an electron time-of-flight spectrometers.[36]

[c] For some molecules, it is also possible to obtain a certain degree of orientation in a molecular beam, in strong electric (hexapole) fields[147–150] or via "symmetry-selective" processes.[151,152] The degree of orientation is rather hard to estimate and generally not as good as with the photoelectron photo-ion coincidence techniques. A new and elegant way is the spatial orientation via rotational wave packets produced by femtosecond laser pulses.[153]

[d] The same technique can of course be applied to Auger electrons and is thus also called *Angle Resolved Electron Fragment-Ion Coincidence technique* (AREFICO).[31,32]

time the molecule takes to dissociate after photoionization, the *spatial orientation* of the molecular axis *at the instant of the photoionization* can be determined from the measured fragment ion momenta. This condition is known as the *axial recoil approximation*.[154, 155 e] If it is fulfilled, it is possible to perform experiments on free, spatially oriented molecules and to measure the *Molecule Frame Photoelectron Angular Distribution (MPAD)* (see chapter 4 and 5).

Several different setups have been and are currently being used to measure MPADs ranging from a combination of a conventional ion TOF-spectrometer with an electron TOF[115, 116]or parallel plate analyzer[82, 145, 146] to more sophisticated setups using imaging spectrometers as described in the previous section for the ion detection[83, 109] or even for both ions and electrons.[120, 158, 159] The latter have the advantage that all orientations of the molecular axis are measured simultaneously, thus yielding a much higher efficiency than the *orientation-selective* methods. The molecular orientation for a particular event is determined only *"a posteriori"* in the data analysis, which also makes these *orientation-sensitive* techniques more flexible. However, they have the disadvantage that the detection of *all* ionic fragments requires either a constant or a pulsed extraction field in the interaction region, which in turn either limits the accessible energy range and the resolution of the electron measurement (see chapter 3.5) or requires very sophisticated timing and electronics (see chapter 3.4).

In this work, the position-sensitive ARFMADS imaging ion spectrometer described in the previous section was used in combination with several electron TOF-analyzers as shown in fig. 3.6.[f] As a constant electric ion extraction-field in the interaction region would

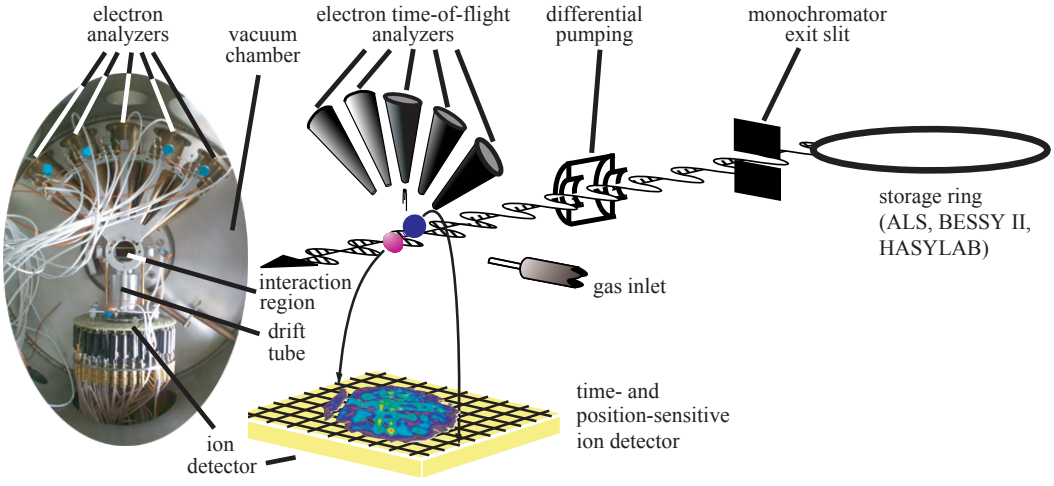

Figure 3.6: Schematic setup for photoelectron-photoion coincidence experiments with synchrotron radiation using the ARFMADS and several electron time-of-flight spectrometers.[108, 109] The inset on the left shows a photograph of the actual setup inside the vacuum chamber.

[e] The validity of this approximation is discussed in section 3.6 and in more detail by Wood *et al.*[156] and Weber *et al.*[157]

[f] Alternatively, the ARFMADS ion spectrometer can also be used in combination with a modified hemispherical Scienta analyzer.[160–162]

deflect the electrons considerably and make an angle resolved detection of electrons in the TOF-spectrometers impossible, the ARFMADS has to be operated in a *pulsed mode*. The gas is introduced between the pusher and the extractor electrodes of the ion spectrometer via a copper needle kept at ground potential and the interaction region is kept (almost) field-free until the detection of an electron in one of the electron analyzers triggers a rectangular high voltage pulse that extracts the ions. In other words, the extraction field is applied and the fragment ions are detected *only* if an electron is detected previously. Consequently, the coincidence count rate is limited mainly by the electron detection efficiency, and up to five electron TOF analyzers are used in the standard setup to increase this efficiency and to detect the electrons at several emission angles simultaneously (see fig. 3.6).[g]

3.4 Electronic Setup of the Coincidence Experiments

As mentioned above, a rather sophisticated signal timing is crucial for a coincidence experiment especially when operating with pulsed ion extraction fields. Since the electronic setup of the experiment and the data acquisition system have recently been switched to a completely new concept,[164] both are described in more detail in the following.

While the old setup was based on analog timing using time-to-amplitude converters (TAC) followed by analog-to-digital converters (ADC) and multichannel analyzers (MCA),[22,108] this combination is now replaced by a time-to-digital converter (TDC) which directly communicates with the data acquisition computer via a PCI card. The data acquisition hardware is illustrated in fig. 3.8. It is based on dual-chip TDC modules for the electrons (resolution 60 ps, multi-hit dead-time < 20ns) and fast multi-hit TDC modules (resolution 120 ps, multi-hit dead-time < 10ns) for the ion time and a fast FPGA-buffer for the ion position information.

With the TDCs, the setup for a non-coincident electron time-of-flight experiment is now very simple (see fig. 3.7). Note that compared to the previous setup where the time-measurement was started by the electron signal and stopped by the bunch marker, the timing is now inverted and the bunch marker provides the start and the electron signals after pre-

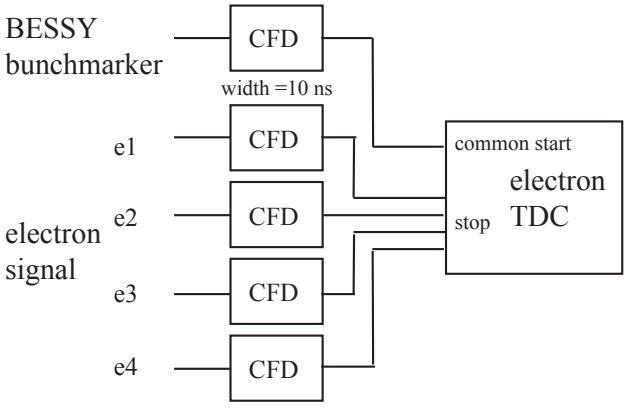

Figure 3.7: Schematics of the electronic setup using a TDC for an experiment with several electron time-of-flight spectrometers.[164]

[g]Currently, a new spherical vacuum chamber with the possibility to install more than 200 electron detectors is being commissioned to be able to detect the electrons at almost arbitrary emission angle.[163]

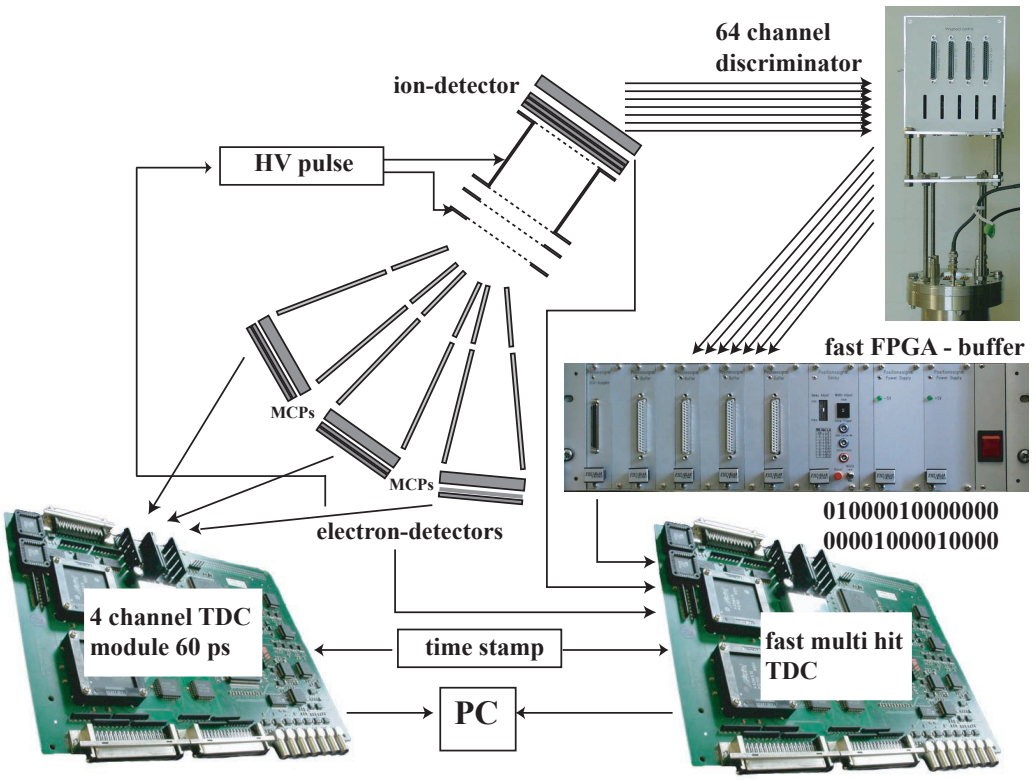

Figure 3.8: The data acquisition system of the current setup using TDC cards.[122,164]

amplifier and constant fraction discriminator (CFD) provide the stop (see fig. 3.10). Up to 4 electron channels can be processed with one TDC card, and more TDC cards can be added for more electron channels.

When recording electron-ion coincidences, the electronics become considerably more complex since the correct timing between the electron and ion signals is important in order to be able to identify coincidence events. The slightly simplified electronic setup is shown in fig. 3.9 and a schematics of the signal timing in fig. 3.10). The full setup used in the actual experiment which includes some additional elements to prevent a possible time-stamp mismatch between electron and ion TDC is shown in appendix A.

Conceptually, the measurement is based on the idea of *event recording*, i.e. each detected event is recorded in an event list together with a time stamp that allows to identify whether or not several events happened in coincidence. The time stamp is provided by a time-stamp generator ("*clock*") synchronized with the bunch marker which in turn is synchronized with the synchrotron light pulses via a tunable delay. When an electron is detected, the ion measurement cycle is started and a high voltage ion extraction pulse is triggered by the *next* bunch marker after the detection of the electron. This link to the bunch marker guarantees that both the ion time-of-flight as well as the time between the creation of the ions and the extraction pulse (called the *insertion delay*) are independent of the electron arrival time. As the ions from dissociative events leave the interaction region with a large velocity, the maximum electronic time delay of the extraction pulse as well

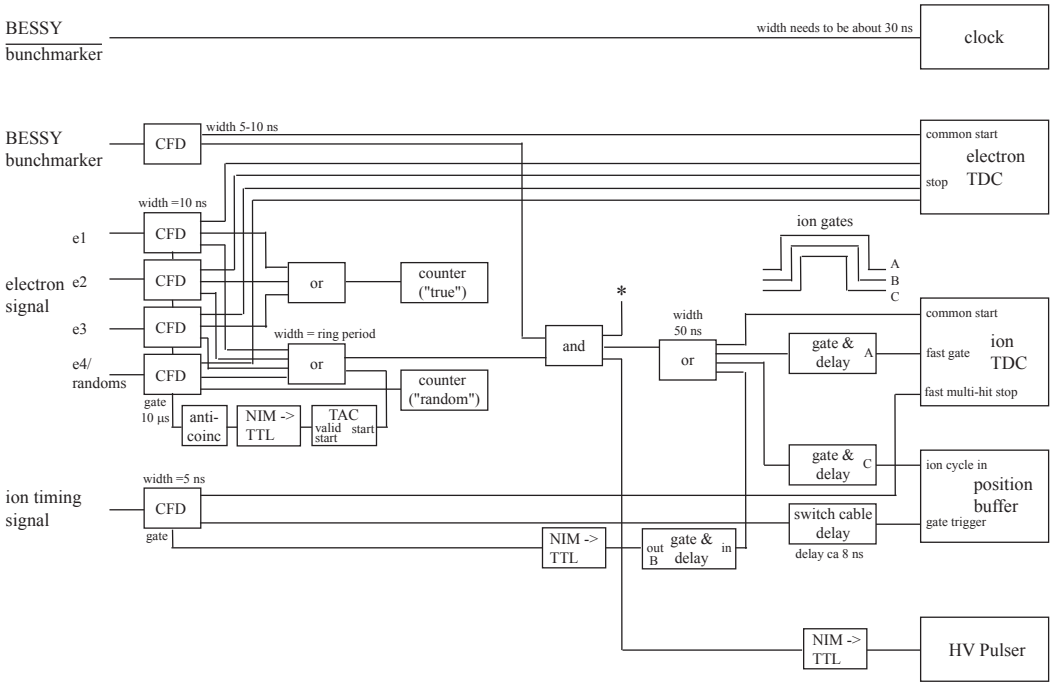

Figure 3.9: Schematics of the electronics and signal pathways for an experiment with several electron time-of-flight spectrometers.[164]

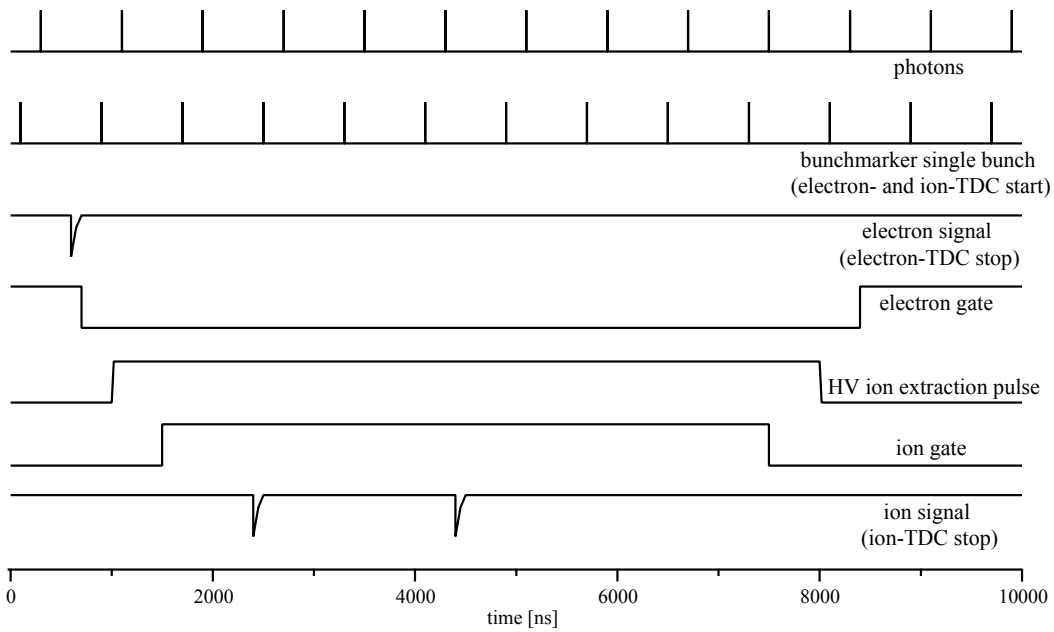

Figure 3.10: Schematics of the timing of a photoelectron-photoion coincidence experiments with synchrotron radiation using the ARFMADS and one or more electron time-of-flight spectrometers.[164]

as its shape are critical for the success of the experiment. Hence, a custom made pulse generator (GPTA HVC-1000) with a maximum delay of 120 ns and 15 ns rise/fall time (10% /90%) is used.[122] The gate for the ion detection opens only *after* the high voltage pulse is fully applied and closes *before* it starts to fall again in order to gate out the noise created by the HV pulse on the signal lines. For the same reason as well as in order to avoid a double triggering of the HV pulser and/or the ion TDC, the electron detection is also inhibited until the full coincidence measurement cycle is finished. Practically, this is done with the combination of TAC and anti-coincidence unit which create a gate for the electron CFDs that closes very fast after an electron signal arrives in one of the CFDs.

When the full capacity of the ion spectrometer is used, i.e. the time-of-flight as well as the hit-positions are recorded, a position buffer that stores the position information has to be used in connection to the ion TDC. It is triggered by the ion timing signal, which also provides the fast multi-hit stop for the ion TDC, and is read out at the end of the ion cycle. The electron time-of-flight information together with the time-of-flight and the hit-positions of each detected ion in the corresponding ion cycle are recorded in an event file from which coincidence events of any type as well as single-electron events etc. can later be extracted for the analysis.

3.5 The COLTRIMS-Technique

An alternative method to measure MPADs is the *Cold Target Recoil Ion Momentum Spectroscopy (COLTRIMS)*.[h] It was originally designed for the application in *atomic* collision and photoionization studies. In that case, it is particularly important that the target atoms have a very small initial momentum (i.e. that they are *cold*) before the interaction with the light or other particles takes place. This requirement is fulfilled in the COLTRIMS technique by using a super-sonic gas jet in which the gas particles have almost zero momentum perpendicular to the direction of the jet. Other than this, the main difference compared to the ARFMADS technique is the use of an *imaging technique* for ions and electrons. *Both* ions *and* electrons are guided onto position sensitive detectors by constant electrostatic and magnetic fields. For photoionization studies within the first 30 eV above threshold, COLTRIMS therefore yields a complete three-dimensional image with 4π detection efficiency for all particles. However, the use of static guiding fields for both electrons and ions requires to compromise between kinetic energy resolution and 4π acceptance angle for the electrons. The energy resolution consequently degrades considerably as the electron kinetic energy increases, leading to a resolution in the order of even a few eV for 10 eV electrons. For electron kinetic energies above 30 eV, the magnetic field that guides the

[h] A general description of the COLTRIMS apparatus is given in a detailed review article[159]; its specific application to molecular photoionization is described by Dörner *et al.*[91,157,165] and for a very similar setup by Lafosse *et al.*[166]; technical information on the position sensitive delay-line anode is also available on the web site `http://www.roentdek.com/`.

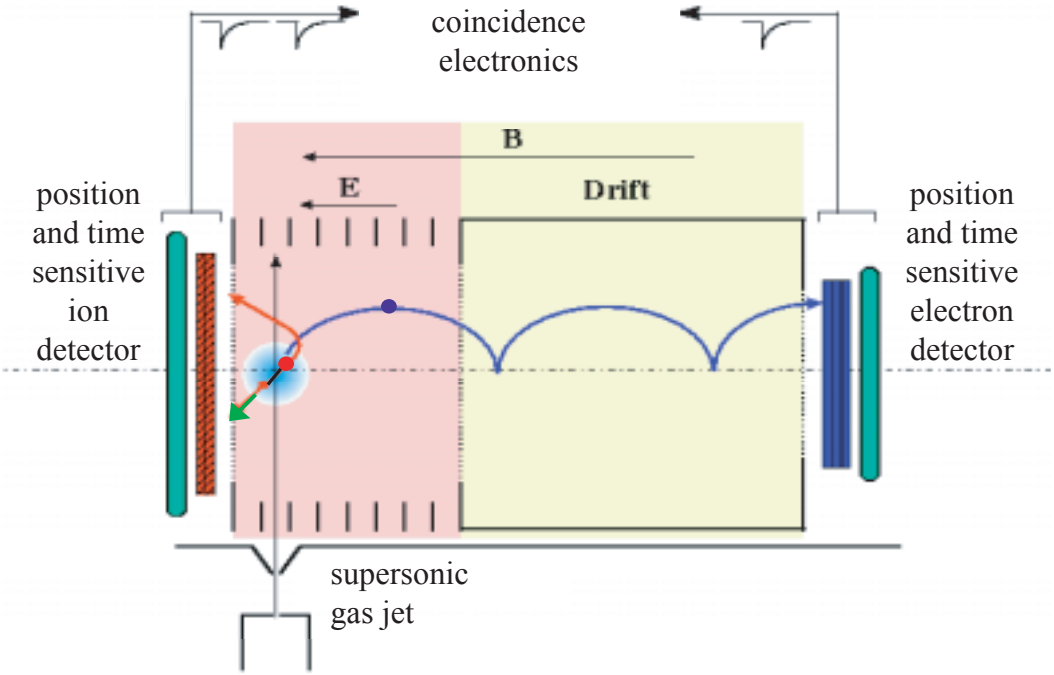

Figure 3.11: Schematic setup of the COLTRIMS apparatus: A supersonic molecular gas jet is crossed with the photon beam. An electric field (20 V/cm) drives the fragment ions and the electron onto the position sensitive channel plate detector with delay line multi-hit readout. A magnetic field forces the electrons on cyclotron trajectories in order to retain them within the detectable region. For the electron and both fragment ions, the positions of impact and the time-of-flight are measured in coincidence.[159]

electrons onto helical trajectories cannot confine them within the detectable region for all emission angles any more and the COLTRIMS electron detector has to be operated like a conventional electron TOF.[32]

3.6 Data Analysis Procedure and Discussion of Experimental Errors and Uncertainties

A fundamental data analysis problem in all coincidence experiments are the *random* or *false coincidences*. Random coincidences correspond to the coincident detection of an electron and ion which originate from two different ionization events. This is particularly problematic in pulsed operation if only a small fraction of the produced electrons are detected. In that case, many fragment ions are created that are not extracted immediately by an extraction pulse. As the interaction region is field free during most of the time, those ions that are not created in a dissociation reaction with a large kinetic energy release have only thermal velocity and need a considerable amount of time before they escape the source region of the ion spectrometer. Hence, they can often generate random coincidences with electrons produced by following light pulses.[i] Experience has shown that the number

[i] In addition, random coincidences can be caused by purely electronic, i.e. statistical, noise on the detectors and amplifiers.

of residual ions in the interaction region can be reduced substantially by applying a small constant potential of usually around 0.5 V to the extractor plate, which often cuts the rate of random coincidences in half. However, the ratio of true to false coincidences can still be as high as 2:1 or even 1:1, creating a non-constant background in the coincidence spectrum that has to be subtracted in the data analysis. In order to characterize the random coincidences, one of the electron channels is connected to a pulse generator that triggers the high voltage ion extraction pulse at random times with respect to the light pulse. The coincidences recorded in this channel are a measure of both the rate of random coincidences as well as of their shape in the multi-dimensional coincidence matrix consisting of electron and ion times-of-flight and ion hit positions, and can therefore be used to subtract the random coincidences. For that purpose, a histogram of the ion times-of-flight produced by the random trigger is generated and scaled by the ratio of detected electron to randomly triggered events. The result is subtracted from the measured time-of-flight spectrum of ions in order to create the *true coincidence* ion spectrum. For the subtraction of the random contribution to the coincident electron spectrum, the *non-coincident* electron spectrum scaled to contain the same number of events as were subtracted from the ion time-of-flight spectrum is subtracted from the coincident electron spectrum resulting in the true coincidence electron spectrum. All coincident spectra and molecule frame angular distributions shown in this work are the result of these subtraction procedures.

For both coincident as well as non-coincident measurements, the data analysis also has to account for possible differences in the *detection efficiency* for different emission angles. If different electron TOF analyzers are used, they have to be normalized with respect to each other in order to cancel the efficiency differences. This is usually done by comparison to calibration gases such as neon or helium which have well known photoionization cross sections and angular distributions. For imaging detectors as used in the COLTRIMS apparatus and in the ARFMADS, the spatial efficiency of the position sensitive anode has to be properly calibrated which is not always a straightforward task for lack of appropriate calibration methods and suitable calibration gases for which the ion angular distributions are known well enough.

Additional errors and uncertainties arise from the mathematical procedure used to derive the initial ion momenta from the time-of-flight and position information. The finite spatial resolution of the position sensitive anode as well as experimental uncertainties in the calibration of the extraction fields both lead to increased errors of the emission angle as well as kinetic energy. For that reason, the finite angular and energy resolution for both electrons and ions also have to be taken into account when comparing to theoretical predictions. Especially for imaging detectors, the angular resolution can sometimes be hard to estimate and may vary for different angles since it depends crucially on the precise knowledge or reconstruction of the electric and magnetic fields. An experimental "acceptance angle" between $\pm 5^\circ$ and $\pm 10^\circ$ is therefore usually a reasonable choice for the particles that are detected in the imaging spectrometer. Consequently, it is experimentally impossi-

ble to measure the MPAD for an orientation of the molecular axis of precisely 0° or 90° for instance, which means that the theoretical selection rules for pure $\Sigma \rightarrow \Sigma$- and $\Sigma \rightarrow \Pi$-transitions (see section 2.4.2) are never completely fulfilled in the experimental angular distribution patterns. Moreover, sharp structures in the MPAD are "smeared out" due to the finite angular as well as energy resolution.

Aside from these technical difficulties, there is the fundamental question of the validity of the axial recoil approximation on which all of the ARPEPICO techniques are based. Very recently, it was found that under certain conditions, namely low *kinetic energy release (KER)*, this approximation might be violated.[157] While being valid for all fragment energies in the case of N_2, the axial recoil approximation breaks down for the CO molecule for kinetic energy releases below 10.2 eV. This could explain to a big extend why the first experimental data on CO taken by Heiser and Shigemasa[83,86] deviate considerably from newer angular distribution measurements[89,91,157,167] in which the energy window of the ion spectrometer was set *above* the critical range.

In summary, one has to keep in mind that some of the experimental errors can sometimes be hard to estimate and that especially when measuring molecule frame angular distributions and comparing different molecular orientations, there can be certain cases in which the uncertainties are higher than expected. Relative measurements such as the diffraction data presented in chapter 4.1 are less prone to some of these errors since most efficiency effects are compensated by comparing only electron events detected in the same electron analyzer and ion events detected in the same area of the position sensitive anode.

Chapter 4

Photoionization of Heteronuclear Molecules: CO:C(1s) Photoelectron Diffraction

The dynamics of the photoelectron emission process in molecules differ from those in atoms in one major respect, namely the angular momentum composition of the outgoing photoelectron waves (see section 2.2). Whereas in atomic photoionization, the number of outgoing partial waves is essentially limited to two,[a] this number may be much larger in molecules due to the intramolecular scattering of the emitted photoelectron. This process depends on the geometry of the molecule, thereby providing information on its topology and electron density distribution.

For many decades, photoionization studies of gas phase molecules were restricted to measurements of total, partial and differential photoionization cross sections of randomly oriented molecules.[17,19] In that case, most of the structural information contained in the scattered electrons is masked by the intrinsic averaging over all molecular orientations. However, over the last 10 years, substantial experimental advances and the development of angle resolved photoelectron-photoion coincidence (ARPEPICO) and multiparticle coincidence techniques described in the previous chapter have made photoionization experiments on *free, oriented* (*"fixed-in-space"*) molecules in the gas phase an exciting new tool to study electronic structure and the dynamics of the continuum wave function. The new techniques allow a much deeper insight into the underlying physical processes and have made very detailed quantitative information accessible to the experiments.[82–91,108,116,120,145,146,157,158,165–181] As explained in section 2.5, *complete experiments* from which all dipole matrix elements and relative phase shifts among different partial waves can be determined, are now possible even for molecular photoionization.[104–106]

[a] Strictly speaking, this limitation is only fullfilled within the limits of the dipole approximation (see section 2.4.3).

Of particular interest in the K-shell photoionization of small molecules are those photon energies -usually the first 20 eV above threshold- for which a *shape resonance* (see chapter 2.4) appears in the continuum, since the photoionization and photoabsorption cross sections as well as the photoelectron angular distributions show radical changes over a narrow energy range,[62,63,71,182,183] and the molecule frame photoelectron angular distributions display rich structures.[80–91,157,167,175,176,179] However, as the following discussion shows, the scattering nature of the core photoelectron emission is displayed even more prominently when a wider energy range is investigated.

4.1 Photoelectron Diffraction from Free Molecules

Photoelectron diffraction (PD)[b] is a well established tool in solid state and surface physics, in which the scattering properties of emitted electrons yield information about the environment of the electron emitter. It is used for example to determine surface structures[139,140,184,185] or the orientation and geometry of molecules adsorbed on metal surfaces.[129–138] While related methods such as EXAFS (extended x-ray absorption fine structure)[186,187] and SEXAFS (surface extended x-ray absorption fine structure)[188] treat modulations of the *total* photoionization cross section, photoelectron diffraction refers to a modulation of the differential cross-section, i.e. angular distribution,[108]

$$\sigma_{PD} \equiv \frac{d^2\sigma_{if}}{d\Omega_{\underline{m}_{\boldsymbol{\varepsilon}}}\, d\Omega_{\underline{\kappa}_{\boldsymbol{\varepsilon}}}} \,, \tag{4.1}$$

where $\underline{m}$ is the molecular axis and $\underline{\kappa}$ the momentum, i.e. emission direction, of the electron, both relative to the polarization vector of the incident radiation $\boldsymbol{\varepsilon}$.

In the past, PD experiments were only possible for molecules adsorbed on surfaces ,[129–138] as the random orientation of gas phase molecules averages out the intensity variations.[c] However, the electronic structure of adsorbed molecules is altered by the additional chemical bond, and the electron emission is affected considerably by scattering on the surface.[139,140] Furthermore, the observable electron emission angles are naturally limited to the half-space above the surface, and the adsorption geometry often makes only one orientation of the molecule accessible to PD studies. From a molecular physics point of view, ARPEPICO experiments on fixed-in-space molecules are thus ideally suited to measure the full and *undisturbed* photoelectron diffraction from free molecules. The first experiment of this kind was performed by Geßner *et al.*, who observed photoelectron diffraction oscillations in the C(1*s*) photoionization of fixed-in-space CO molecules.[108,189]

In the present work, an extensive study of the photoelectron diffraction from free CO

[b] The abbreviations PED and PhD are also common.

[c] An exception is the photoelectron diffraction-like behavior observed in randomly oriented C_{60}, where the high molecular symmetry leads to diffraction oscillations in the partial cross-section of the outermost valence states.[189–191]

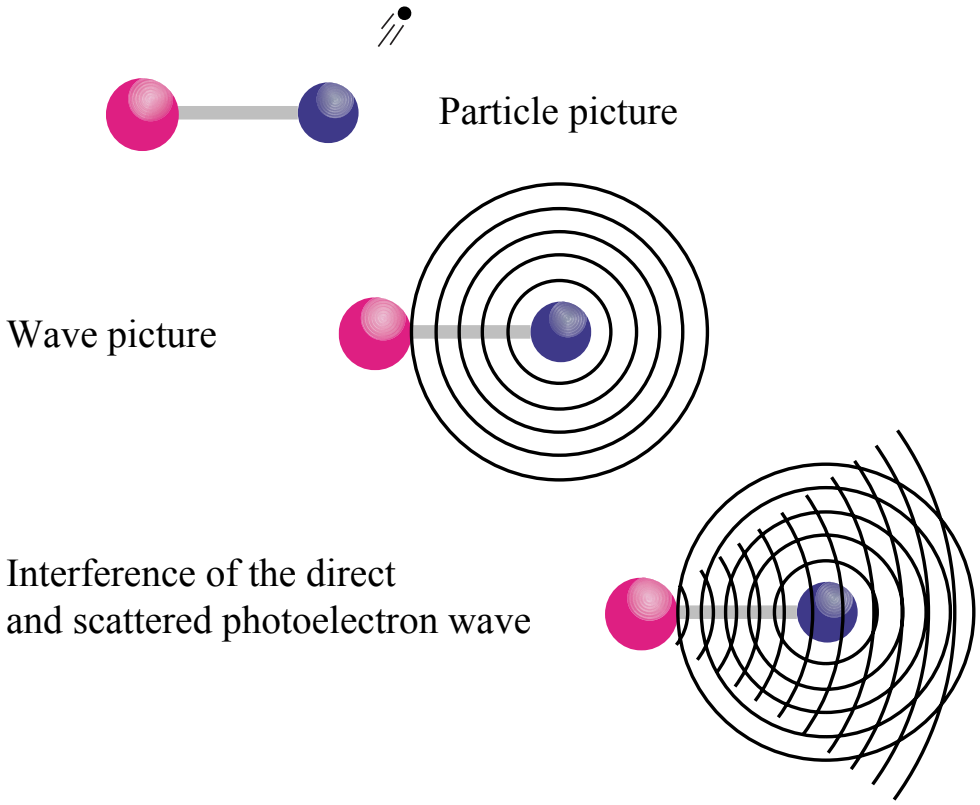

Figure 4.1: Illustrative model of photoelectron scattering in a molecule.

molecules over a wide energy range from the C(1*s*) threshold up to a photoelectron kinetic energy of 400 eV is presented. As explained in chapter 3.3, the spatial orientation of the molecules is determined through an electron-ion coincidence experiment, where the time-of-flight of the electrons is recorded together with the time-of-flight of the ionic fragments and their hit positions on a crossed-wire type position-sensitive anode. This information allows to reconstruct the initial momenta of the fragment ions and hence, within the axial-recoil approximation,[154,155] the orientation of the molecular axis at the time of the fragmentation. The electrons produced in the interaction region by the monochromatic, linearly polarized synchrotron radiation crossing an effusive beam of CO gas (99.999% purity) are detected at various angles relative to the light polarization vector with an acceptance angle of $\pm 4^\circ$, determined by the entrance aperture of the electron TOF-spectrometers. A retarding or acceleration voltage is applied to the drift-tubes of lengths ≈ 150 mm in order to increase the resolution for fast electrons or to obtain higher transmission for electrons with low kinetic energy. For the analysis of the photoelectron diffraction, only those coincidence events are selected, for which the molecular axis was oriented parallel respectively perpendicular to the polarization vector (with an acceptance angle of $\pm 25^\circ$ in order to improve the statistics). Coincidence events of a C(1*s*) electron with either a C^+ or O^+ ion are used for the selection of the molecular axis,[d] and only fragment ions with a kinetic

[d] According to branching ratio measurements, the C^+-O^+ channel accounts for 80% of the total ion yield above the C-K-edge.[192,193]

energy above 5 eV for O^+ respectively 6 eV for C^+, i.e. above ≈ 11 eV total kinetic energy release (KER), where considered in order to assure the validity of the axial recoil approximation.[157]

To compensate for the rapidly decaying C(1*s*) partial cross section and to avoid possible transmission effects in the electron spectrometers, the axis-selected electron–ion–coincidence intensity σ_{PD} is normalized to the non-coincident intensity of the C(1*s*)–photo line $I_{C(1s)}$ in the same electron analyzer:[108]

$$\tilde{\chi}_{PD}(k) \;=\; \frac{\sigma_{PD}}{I_{C(1s)}} \;. \tag{4.2}$$

This angle-dependent, non-coincident intensity $I_{C(1s)}$ is given by eq. (2.16) and is proportional to the partial cross section σ_{1s} weighted by the effect of the electron angular distribution, which scales with $(1+\beta_e)$ for detection *along the polarization direction*, β_e being the photoelectron angular distribution asymmetry parameter for randomly oriented molecules (see chapter 2.4.2):

$$\tilde{\chi}^0_{PD}(k) \;=\; \frac{\sigma^0_{PD}}{I^0_C(1s)} \;=\; \frac{\sigma^0_{PD}}{\sigma_{1s}\,(1+\beta_e)} \;. \tag{4.3}$$

In order to compensate for the additional angular distribution effect induced by the normalization, the data are then corrected with the experimentally determined angular distribution parameter, so that the final diffraction curves are independent of β_e:

$$\chi^0_{PD}(k) \;=\; \tilde{\chi}^0_{PD}(k)\,(1+\beta_e) \;=\; \frac{\sigma^0_{PD}}{\sigma_{1s}} \;. \tag{4.4}$$

The experiments on free molecules allow to select *any* molecular orientation and emission geometry, in particular the two extreme cases where the electron is emitted along the molecular axis and the emitting atom points either directly towards or away from the electron emission direction. Fig. 4.2 shows the resulting diffraction curves for electrons emitted from the carbon atom (a) *into* the molecule towards the oxygen atom ("forward scattering" geometry) as well as (b) *away* from the molecule ("backward scattering" geometry), with the molecular axis being oriented along the light polarization vector. The new data are shown together with the data taken by Geßner *et al.*[108,189] with an older version of the coincidence apparatus described in chapter 3.3. While the general design of the two is very similar, the new setup has higher position and time resolution and an improved detection efficiency, which leads to a much improved overall performance of the experiment. Furthermore, previously published data taken by Landers *et al.*[91] using the COLTRIMS technique have been re-analyzed in order to compare to the present measurements at low kinetic energies. All data sets are in very good agreement.

The experimental data are also compared to a calculation in the partially relaxed-core

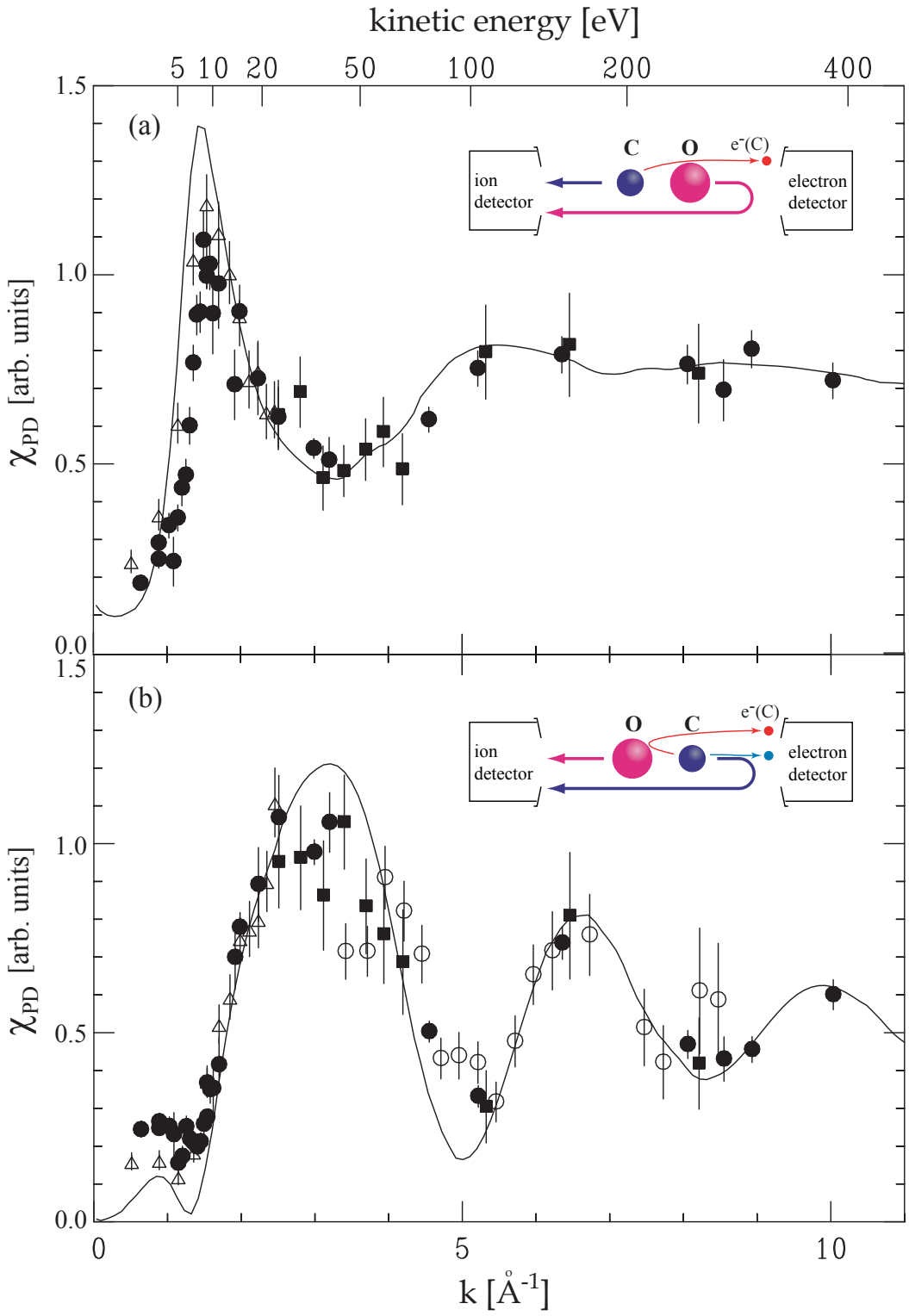

Figure 4.2: C(1*s*) photoelectron diffraction from free CO molecules in the forward (a) and backward (b) scattering geometry. Full circles represent data taken with the new setup, while the squares are taken with the old apparatus (see text). The open circles represent previously published data[108,189] measured also with the old setup, while the open triangles are a re-analysis of data measured by Landers *et al.* with the COLTRIMS apparatus.[91,194] The lines are calculations in the partially relaxed-core Hartree-Fock (RCHF) approximation by Zimmermann *et al.*[195]

Hartree-Fock (RCHF) approximation by Zimmermann *et al.*[195,196] [e] The ground state wave function is calculated in the self-consistent Hartree-Fock approximation, while the ionic state wave function is derived in the Slater transition state approach,[197] where only a *fraction* of an elementary charge, in this case half an electron charge, is removed from the carbon K-shell in order to account for the *screening* of the core hole.[198,199] The final state electron wave function is then obtained using the iterative Schwinger variational method.[200] [f]

Fig. 4.2(b) shows the typical, bond length dependent photoelectron diffraction oscillations known from surface physics experiments. The oscillations are very pronounced in the backward scattering channel while the forward scattering shown in fig. 4.2(a) exhibits a large peak at low photoelectron kinetic energies but is rather structureless at high energies. The origin of the oscillations, which can be approximated by an attenuated sine wave

$$\chi_{PhD}(k) \approx A(k)\,\sin\left(2\pi\,\frac{k}{\mathscr{P}} + \varepsilon(k)\right)\,, \tag{4.5}$$

where $A(k)$ decays exponentially with increasing k, $\mathscr{P}$ is the moduation period, and $\varepsilon(k)$ accounts for scattering phase shifts, can be explained by a simple geometrical model illustrating the interference of directly emitted and scattered electron waves (see fig. 4.3). For a first quantitative estimate, let us assume a spherical electron wave starting from the carbon atom and being scattered off the oxygen atom. The path length difference Δs between the direct and the first order scattered waves at the position of the detector is of course a function of the electron emission angle θ_e with respect to the molecular axis: $\Delta s = R + R\cos\theta_e$, where R is the bond length of the molecule. The maximum path length difference thus occurs *along* the molecular axis in the backward scattering geometry, i.e. $\theta_e = 0°$, where the path difference between the direct wave ψ_0 and the first order scattered wave ψ_1 is equal to twice the bond length. Intensity maxima occur for constructive interfere of ψ_0 and ψ_1, which, neglecting the phase shift from the scattering on the nuclei, is expected for

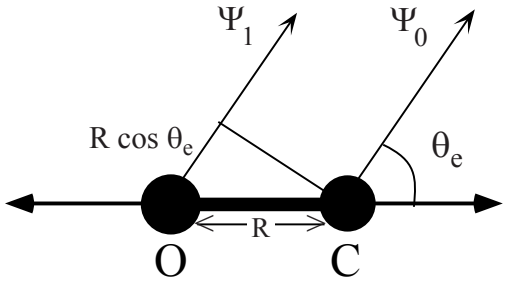

Figure 4.3: Schematic model of the scattering geometry in a heteronuclear molecule that can lead to interference.

$$2R = n\lambda_e\,,\ n = 1,2,3,\ldots \tag{4.6}$$

[e] In order to imitate the experimental normalization, the calculated molecule frame angular distributions were divided by the theoretically determined photoionization cross section. A better agreement was found if the influence of the β was corrected in the experimental data (see eq. 4.4) rather than including it in the calculations, since the theoretical β value differs quite substantially from the experimental value at some energies.

[f] For a more detailed description of the theoretical formalism, I refer the interested reader to the dissertation by Björn Zimmermann[103] as well as the above-mentioned references.

With an equilibrium internuclear distance of $R = 1.128$ Å for the molecular ground state respectively $R = 1.180$ Å for the core ionized CO molecule,[201] the *de–Broglie–wavelength* of the photoelectron given by

$$\lambda_e = \frac{h}{k} = \frac{h}{\sqrt{2Em_0}}\,, \quad \text{i.e. } \lambda\,[\text{Å}] \approx \frac{12}{\sqrt{E\,[\text{eV}]}}\,, \tag{4.7}$$

and the electron momentum

$$k = \frac{h}{\lambda}\,, \quad \text{i.e. } k[\text{Å}^{-1}] \approx 0.5123\,\sqrt{E\,[\text{eV}]}\,, \tag{4.8}$$

eq. (4.5) and (4.6) yield an estimated modulation period

$$\mathscr{P} = \pi\,\frac{1}{R} \;\approx\; 3\text{Å}^{-1}\,, \tag{4.9}$$

which is in good agreement with the experimental findings despite this rather simple model.

The experience from surface physics experiments shows that for a more precise analysis yielding a reliable value for the bond length, a rather sophisticated modeling of the background is necessary in order to perform a Fourier transformation of the modulations.[188] Moreover, both SEXAFS and PD measurements on small molecules suffer from the fact that the backscattering amplitude decays rapidly with increasing kinetic energy of the photoelectron, which, in conjunction with the relatively short bond length, reduces the number of observable, complete SEXAFS or PD oscillations and critically affects the reliability of

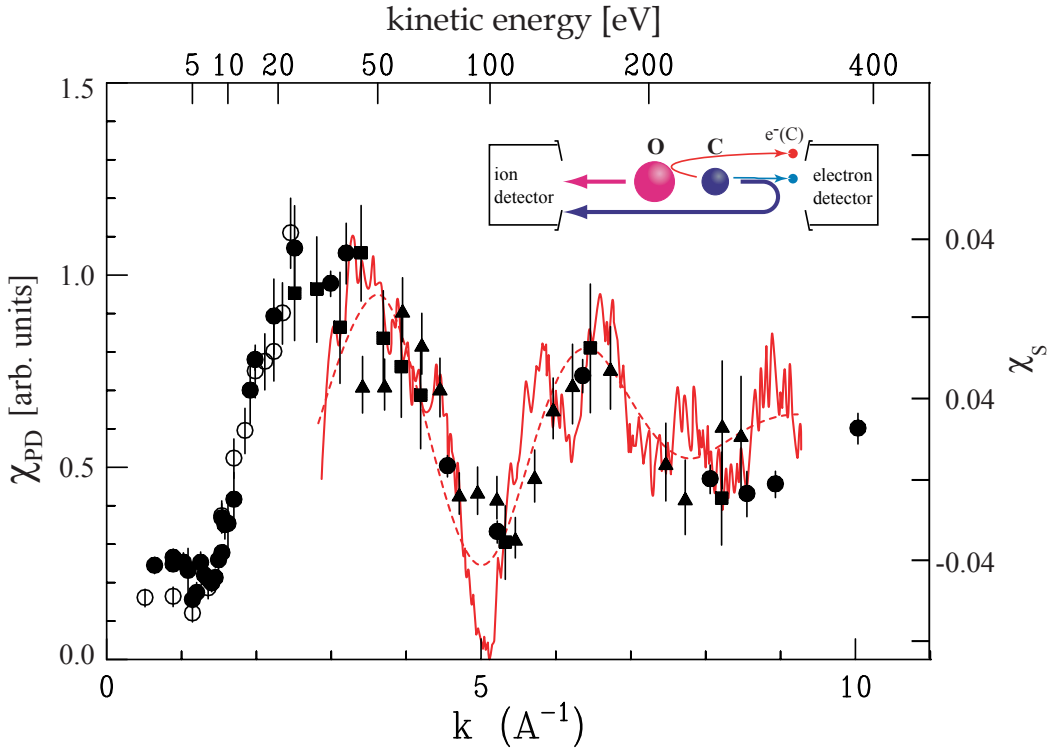

Figure 4.4: C(1s) photoelectron diffraction from free CO molecules in the backward scattering geometry (black) compared to SEXAFS measurement by Pangher *et al.* (red).[202] The dashed line is a fit to the SEXAFS data, which was used for a Fourier transformation.

the bond length determination. Despite these complications, Pangher *et al.* have shown that the determination of intramolecular bond length of small molecules through SEXAFS is possible for both gas phase as well as chemisorbed molecules.[202] Fig. 4.4 shows a comparison of the present backscattering diffraction data with their SEXAFS data obtained for CO molecules chemisorbed on a Cu(100) surface, from which a bond length of 1.15 ± 0.1 Å was determined.[202] The two data sets agree reasonably well, especially bearing in mind that the SEXAFS data were measured at the oxygen rather than the carbon K-edge, where the bond length is known to be slightly different.[44]

The present results and the comparison to the SEXAFS data demonstrate that a photoelectron diffraction measurement is not only possible for free molecules in the gas phase, but that it allows a direct determination of the molecular structure of the free molecule. Besides this more technical aspect, the gas phase measurement also allows to estimate the importance of higher order scattering effect. In that respect, it is interesting to note that the photoelectron diffraction in the forward channel shows only very weak structure except for the large peak at low kinetic energies which is discussed in chapter 4.3. If second or higher order scattering were a substantial contribution, there should also be oscillations in the forward scattering channel. Their absence thus proves that higher order scattering is negligible except for low kinetic energies.

4.2 Angular Dependence of the Photoelectron Diffraction

The energy dependent variation of the forward and backward intensity and the related redistribution of photoelectron intensity in the molecule frame is also clearly visible in the photoelectron angular distribution for fixed-in-space molecules shown in fig. 4.5, which were recorded simultaneously to the photoelectron diffraction presented above. From these distributions, the diffraction for electron emission angles of 22.5° and 45° respectively 135° and 157.5° with respect to the molecular axis can also be determined. It is presented in fig. 4.6, again corrected with the experimental β_e in order to compensate for laboratory frame angular distribution effects, and plotted together with the theoretical curves by Zimmermann *et al.*[195] Comparing the diffraction for the different angles, an angle dependent shift of the oscillations in the backward channel can be noted, which can also be explained by the scattering geometry shown in fig. 4.3. As mentioned in the preceding discussion, the first interference maximum occurs for $\Delta s = \lambda$, while the first minimum of *destructive* interference occurs if the path length difference is $\Delta s = \lambda/2$. For detection along the molecular axis, these conditions yield eq. (4.6)-(4.9). However, as the detector moves away from the axis, the path length difference between the direct and the first order scattered wave decreases with $\cos\theta_e$, where θ_e is the photoelectron emission angle with respect to the molecular axis. Consequently, the interference maxima and minima move to higher kinetic energies and the modulation period increases.

Based on this reasoning, for electron emission *perpendicular* to the molecular axis,

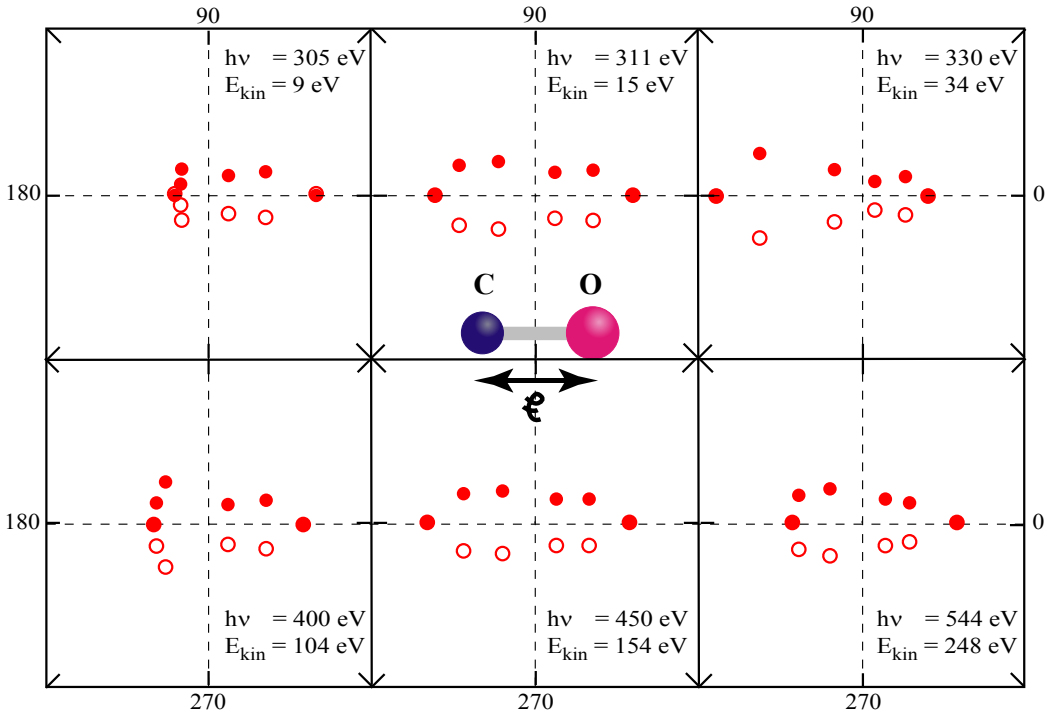

Figure 4.5: CO:C(1*s*) molecule frame photoelectron angular distribution at various photon energies for orientation of the molecular axis parallel to the polarization vector as measured in the photoelectron diffraction experiment. The open circles are the symmetric completion of the measured data points shown as full circles.

one might expect an oscillation with only half the frequency (i.e. twice the period) than in the parallel case, corresponding to a single bond length path length difference between the direct and first order scattered wave in this geometry. However, as the actual initial wave function of the emitted photoelectron before scattering is of course not spherical as assumed in the simple model but highly anisotropic, namely with the typical *p*-wave character of an *s* ionization, it has a node at 90°, and no intensity (and hence also no scattering) can be observed perpendicular to the molecule when the molecular axis is oriented parallel to the polarization vector (i.e. for so-called $\Sigma \rightarrow \Sigma$ transitions).[60,70,71] However, it is possible to analyze the diffraction at this angle for a different orientation of the molecular axis, namely *perpendicular* to the polarization vector, emission perpendicular to the molecular axis is allowed ("$\Sigma \rightarrow \Pi$ transitions").

Fig. 4.7 shows the resulting photoelectron diffraction for molecules oriented perpendicular to the polarization vector, with either the carbon or the oxygen atom pointing "up". For the extreme case of electron emission along the polarization vector, i.e. perpendicular to the molecular axis, the two orientation are, of course, identical. In this geometry, a very faint oscillation with twice the period than in the parallel case is consistent with the measured data, providing some evidence for single scattering in the electron emission perpendicular to the molecular axis. However, the oscillations are very weak since the influence of the scattering potentials is minimal for emission *perpendicular* to the molecular axis. In other words, the electrons in this geometry have almost pure *p*-wave character and

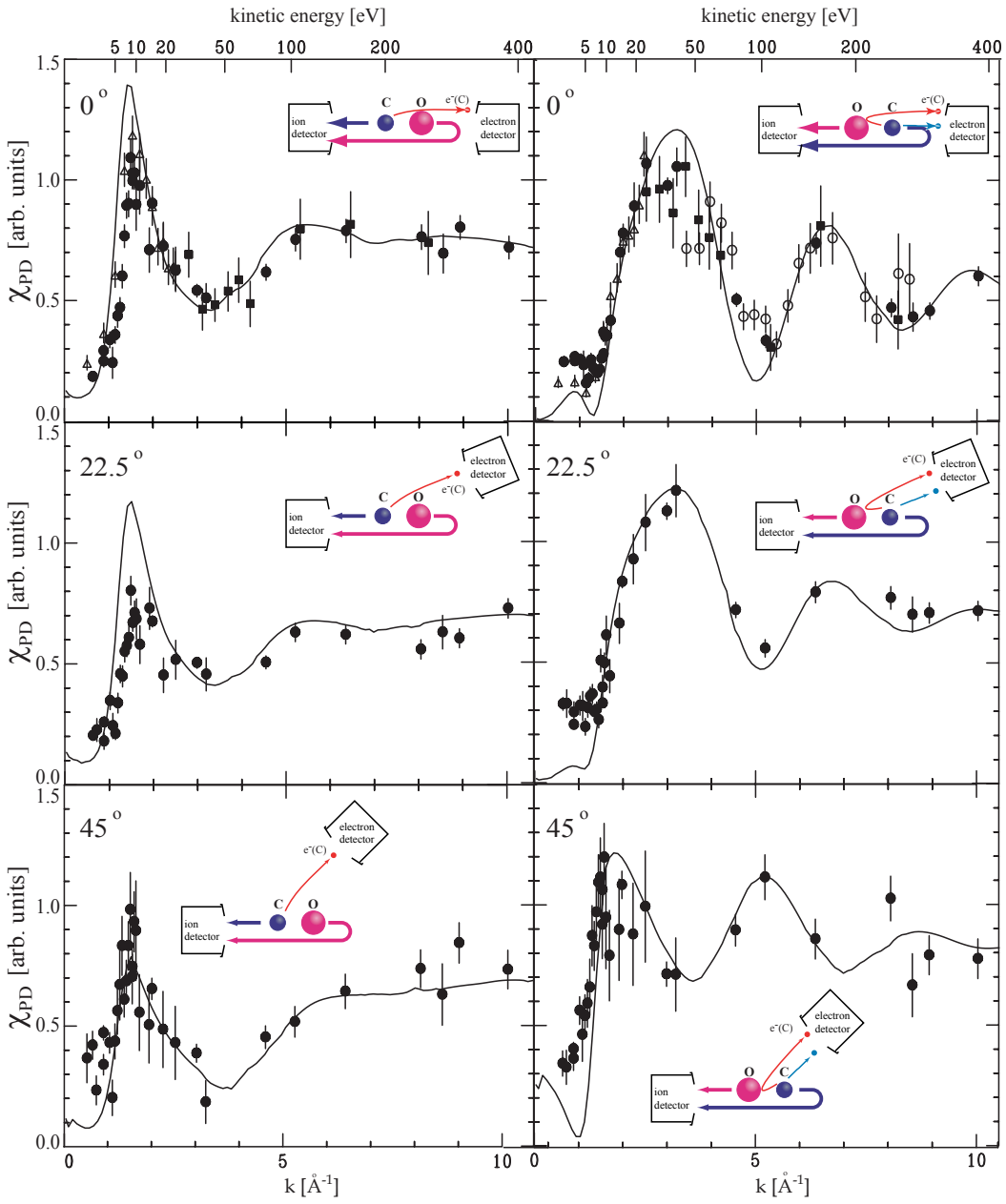

Figure 4.6: C(1*s*) photoelectron diffraction from free CO molecules for orientation of the molecular axis parallel to the polarization vector and different electron detection angles compared to the theoretical curves by Zimmermann *et al.*[195] (solid lines). An angle dependent shift of the maxima and minima can be observed in the backscattering channel, which is shown in the right-hand panels.

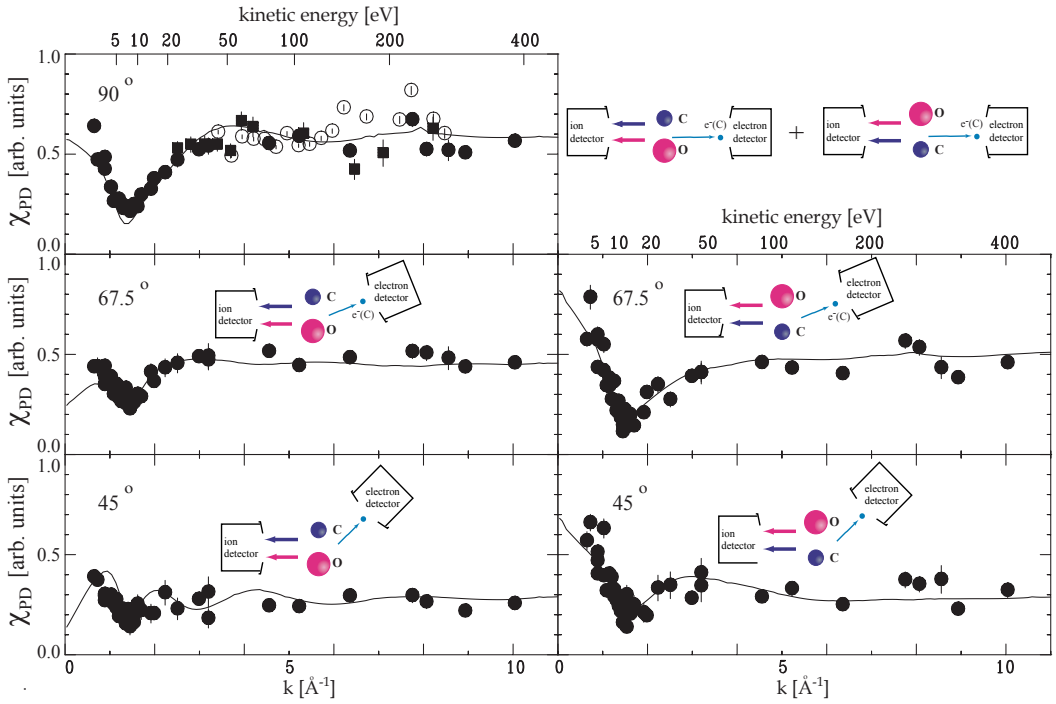

Figure 4.7: C(1*s*) photoelectron diffraction from free CO molecules for orientation of the molecular axis perpendicular to the polarization vector and different electron detection angles. Again, full circles represent data taken with the new setup while the squares are taken with the old apparatus (see text). The open circles are taken from the dissertation of Oliver Geßner,[108] and the solid lines are the theoretical curves by BjöZimmermann *et al.*[195]

are hardly modulated by diffraction. Only for low kinetic energies, where the electrons are more sensitive to the non-spherical nature of the molecular potential, the scattering yields higher order partial waves that distort the *p*-wave character. These higher order partial waves, which have also been observed and identified in the experimentally measured MPADs for low electron kinetic energies,[83,86,88,89,175,176] result in the low-energetic structure displayed in the diffraction curves in fig. 4.7.[g]

4.3 The Scattering Nature of the Shape Resonance

The appearance of a shape resonance and the rich structure of the photoelectron angular distributions in the neighboring energy region are a striking example of scattering and photoelectron diffraction effects in molecular photoionization and show in particular the sensitivity of the low-energy scattering to the details of the molecular potential. As an example, fig. 4.8 shows the molecule frame angular distributions for the C(1*s*) photoelectron measured by Landers[91,157] respectively Motoki *et al.*[89] for linearly polarized light

[g]The pronounced minimum at low kinetic energies, which can be seen at all electron emission angles for this axis orientation, is in parts also due to the normalization of the diffraction to the partial cross section. As the cross section of the $\Sigma \rightarrow \Pi$ channel is not affected by the shape resonance,[60] a normalization to the symmetry-unresolved, axis-averaged cross section, which does include this resonance, results in an artificial minimum at the resonance position.

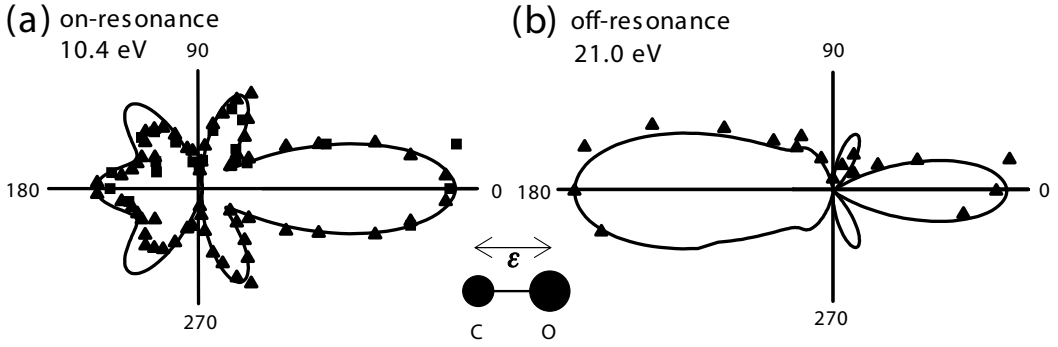

Figure 4.8: Angular distribution of photoelectrons emitted from the carbon K-shell in CO by linearly polarized light with the $\boldsymbol{\varepsilon}$-vector parallel to the molecular axis. The oxygen atom is at 0° (right side of the picture), the C atom at 180° (left side of the picture). The kinetic energy of the electrons is 10.4 eV in panel **(a)** and 21.0 eV in panel **(b)**. The solid line are theoretical calculations in the MSNSP approach, the black triangles and squares are experimental data from Landers *et al.*[91,157] and Motoki *et al.*[89] respectively. Arbitrary units are used.

with the polarization vector parallel to the molecular axis, together with a calculation in the *multiple scattering in non-spherical potentials (MSNSP)* method [157,179] (see Appendix B) which agree well with the experimental data.[h] Two different kinetic energies of the electron are shown: one at the shape resonance ($E = 10.4\,\text{eV}$), and a second one above it ($E = 21.0\,\text{eV}$). Above the shape resonance, the electron intensity in the direction of the carbon atom is higher than the electron intensity in the oxygen direction.[83] This behavior is reversed at the shape resonance, providing a first evidence that the resonance implies special conditions of scattering for which the directly emitted and the scattered waves combine to create constructive interference along the O direction. The situation is even more prominently displayed in the photoelectron diffraction (fig. 4.2(a)), where a large peak at the position of the shape resonance can be seen in the forward channel.

As mentioned in section 2.4.1, shape-resonances can be explained in terms of an interaction between the photoemitted electron and the surroundings of the photoemitter in the molecule. Because the molecule as a whole forms a potential well for the outgoing photoelectron, resonant, pseudo-bound states can form at certain energies, producing a strongly modified continuum wave function which causes this continuum resonance.[62,63] The symmetry and energy of the resonant state often resemble those of the lowest virtual (unoccupied) molecular orbital,[50,64–66] and shape resonances can therefore also be attributed to the trapping of the outgoing electron in an anti-bonding molecular orbital (MO), which subsequently decays into the molecular continuum. In the particular case of carbon monoxide, the C(1*s*) shape resonance is known to occur in the $\Sigma \rightarrow \Sigma$ channel[60,62] and corresponds to a trapping of the photoelectron in the anti-bonding σ^* molecular orbital. The equivalence of the scattering and the molecular orbital picture has been noted,[203] but both are sometimes still interpreted as competing explanations.

[h] The finite experimental resolution is included in the theoretical calculation by averaging over the respective energy range and angles.

Based on empirical evidence collected via photoabsorption studies of a large number of small molecules and inspired by the proposed scattering nature of the shape resonance as well as theoretically found bond length dependence of the resonance position,[204] it was suggested that the kinetic energy, at which the shape resonance occurs, could be used to determine the bond length respectively bond length changes of gas phase and chemisorbed molecules.[61,205–209] While this claim created a heated and long-lasting debate[193,210–214] and inspired a number of theoretical studies,[66,215] it was the origin of a new method in surface studies called *near-edge x-ray absorption fine structure* (NEXAFS).[206] Similar to PD and EXAFS, it is widely used to determine the bond length and geometry of molecules adsorbed on surfaces.[207,209,216]

In the course of the above-mentioned discussion, it was argued that the "special scattering conditions" evoked in the explanation of the shape resonance were little helpful to the understanding of the process, and their physical interpretation was implicitly questioned. However, the rich structure of the molecule frame angular distribution strongly suggested the existence of such "special scattering conditions" which lead to pronounced interference of the directly emitted and multiply scattered electron waves. The photoelectron diffraction experiments on free molecules clearly confirm this interpretation. The appearance of the prominent peak only in the forward channel suggests that a strong increase of *second order scattering* is responsible for the shape resonance. In that sense, the present gas-phase photoelectron diffraction measurements constitute a *direct* evidence for the multiple scattering character of the shape resonance, thereby confirm the usefulness and justification of the scattering picture.

Chapter 5

Photoionization of Homonuclear Molecules: Coherent versus Incoherent Electron Emission in N_2

As demonstrated in the previous chapter, electron scattering plays an essential role in the K-shell photoionization of small molecules. For heteronuclear molecules such as CO, the scattering picture can be employed rather straightforwardly since the lowest molecular orbitals are, to a very good approximation, identical to the respective atomic orbitals (see fig. 2.5(b)) and therefore highly localized. When the molecule is *homonuclear* as for instance N_2, the theoretical description of the photoionization process is more complex due to the *equivalence*, or *indistinguishability*, of the two atomic centers. As explained in section 2.3, the inversion symmetry of the molecule results in a splitting of the lowest, originally degenerate atomic orbital into two molecular orbitals with different symmetry and a binding energy difference proportional to the overlap between the atomic orbitals (see fig. 2.5(a)). These two orbitals are both *non-local* in the sense that they cannot be attributed to one of the two centers any more. Conceptually, this brings up the question if one has to describe the emitted photoelectron by *two* outgoing electron wave functions starting from *both* centers (i.e. one from each center) *coherently*, or if the angular distribution is simply the *incoherent* sum of *localized* emission from one *or* the other center.[85,217–219] A directly related and very debated question is whether the resulting core hole in a homonuclear molecule is *localized* or *delocalized*.[47,48,85,183,220–224] To answer these questions in the following chapters, the K-shell photoionization of N_2 is compared to the case of CO, and the conceptual differences as well as similarities between the photoemission of homonuclear versus heteronuclear molecules are discussed.

5.1 The Concept of Coherent Emission: A Molecular Two-Slit Experiment

The picture of *coherent electron emission* from both molecular centers in a diatomic homonuclear molecule has certain similarities with *Young's two-slit experiment*, although one has to keep in mind that the final state scattering of the photoelectron wave in the anisotropic molecular potential alters substantially the interference effects derived in a simple two-slit picture. Nevertheless, the analogy helps to gain a qualitative understanding and to point out the clear distinction from the electron emission process in a heteronuclear molecule where such *initial state* interference does not occur.

For the following discussion, let me first consider a *symmetric* break-up of the homonuclear molecule into two identical, singly charged fragments. In this case, the experiment does not give any indication from which atom the photoelectron is emitted, and the *indistinguishability* of the two possibilities "*emission from atom* A" and "*emission from atom* B" leads to quantum mechanical interference that depends on the *path length difference* between the two outgoing photoelectron waves.[a] In contrast to the diffraction caused by the interference of scattered waves in the heteronuclear CO, which is a pure final state effect, the interference effect discussed here is an *initial state* effect caused by the quantum mechanical indistinguishability of the two possible centers of origin.

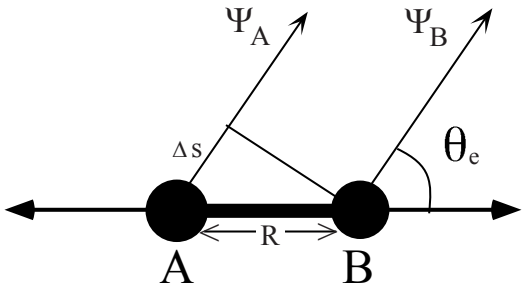

Figure 5.1: Schematic model of the geometry in a homonuclear molecule that can lead to interference in the case of coherent emission.

The fundamental idea of such interference effects in molecular photoionization was first brought up by Cohen and Fano in 1966 when discussing total absorption cross section data for H_2, N_2 and O_2 molecules.[217] In 1969, Kaplan and Markin predicted double slit-like interference effects in the photoionization and the photoelectron angular distributions of oriented H_2 molecules.[218] Their simple calculations did not account for any scattering of the photoelectrons (which is a reasonable first assumption for the case of H_2), and resulted in interference patterns which depend only on the bond length and the kinetic energy of the photoelectron, as shown schematically in fig. 5.1. However, the first multiple scattering calculations of K-shell photoionization performed by Dill *et al.* for N_2 concentrated on the role played by the scattering of the photoelectrons and the resulting *interference of different partial waves*,[62,63,79,80] but explicitly assumed an *incoherent* emission process

[a] As mentioned in chapter 2.4.3, an additional phase factor reflecting the path length difference of the incident radiation may have to be considered for a truly quantitative description. For molecules oriented along the light propagation direction, this phase factor should have the form $e^{\,i\mathbf{k}_{ph}\cdot(\mathbf{r}_A-\mathbf{r}_B)}$, where $\mathbf{k}_{ph}$ is the photon momentum and $\mathbf{r}_A$ and $\mathbf{r}_B$ are the positions of the two atoms.

for the calculations of the molecule frame photoelectron angular distributions.[80] This was most likely motivated by earlier works by Snyder[223] and Bagus *et al.*,[220] who had concluded from energy considerations that the core hole in certain molecules with equivalent sites should be localized. Subsequent work by Dill *et al.* explored this question further by calculating the N_2:N(1*s*) angular distribution parameter β in a localized and delocalized model and suggested *dynamic symmetry breaking* as reason for the localization of the core hole, which the calculations seemed to suggest.[183] However, later corrections to the calculations made the previous argument less convincing, despite the authors claim that their conclusion was still valid.

The original idea of coherent photoelectron emission have a revival, when first measurements of fixed-in-space N_2 by Shigemasa *et al.*[82,84] showed angular distributions that did *not* agree with the incoherent predictions by Dill *et al.*[80] In the region of the N_2:N(1*s*) σ-shape resonance, the measured MPAD for parallel orientation of the $\boldsymbol{\varepsilon}$-vector and the molecular axis shows prominent and distinct maxima at electron emission angles of roughly 60° and 120° with respect to the molecular axis, which are by far less pronounced in the incoherent Dill-calculations (fig. 5.2). Pavlychev *et al.* attributed the amplification of these maxima to interference effects and concluded that the photoelectron emission in N_2 had to be mainly coherent.[85] However, following discussions[225] suggested that these conclusion may have been somewhat ambiguous, as the calculations in the coherent and incoherent model did not include the same number of partial waves. Indeed, new calculations show that the quantitative deficiency of the Dill calculation is mostly due to the approximation of the scattering potential as a spherical muffin-tin potential.[286,288] The angular distribution of the unresolved N_2N:(1*s*) photo line on the shape resonance can be obtained with very good agreement also in the incoherent picture if a more realistic potential is used in the multiple scattering calculations (fig. 5.2).[179,286] In the following, these theoretical findings as well as new, more conclusive experimental results are presented and, based on this information, the question of coherent versus incoherent photoelectron emission as well as the related subject of core hole localization is revisited.

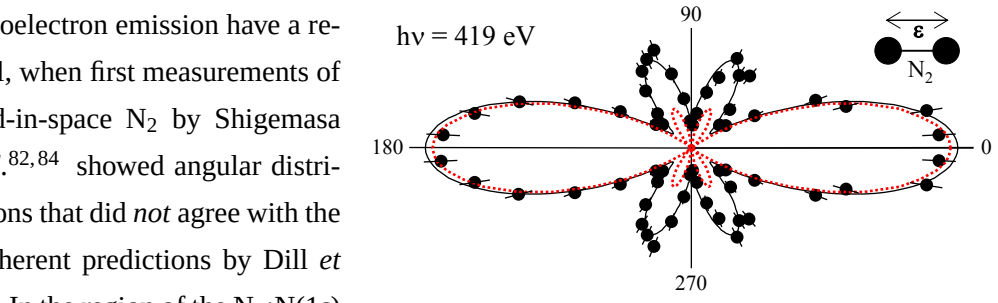

Figure 5.2: K-shell photoelectron angular distribution of N_2 at a photon energy of hν = 419 eV (the kinetic energy of the electrons is 10 eV).The solid black line is calculated in the MSNSP approach (see Appendix B), the red, dotted line is the multiple scattering calculation by Dill *et al.*[80], and the black squares are experimental data from Jahnke *et al.*[167] Arbitrary units are used.

Simultaneously to the photoionization studies presented here, interference effects in homonuclear molecules have also been discussed recently for the double-photoionization of H_2[227] as well as in the field of collision physics, where such effects have been reported

by Stolterfoht *et al.* in electron emission from H_2 colliding with heavy ions,[228–230] followed by a number of new theoretical works.[231–233] The discussion of coherence effects in photoemission also continued in the field of solid state and surface physics,[219,226] and the conclusions from the following chapters certainly impact these fields as well.

5.2 Coherence versus Incoherence

For the simplicity of the following discussion, I want to consider a *diatomic* homonuclear molecule and call the two (identical) atoms A and B.[b] If we describe the photoelectron emission from such homonuclear molecule in a *delocalized* picture by a *coherent* superposition of *two* outgoing electron wave functions starting from one of the two centers each (as illustrated in the two-slit model in fig. 5.1), we obtain two symmetrized solutions analogous to the symmetrized $1\sigma_g$ and $1\sigma_u$ core electron wave functions (see section 2.3):

$$\begin{aligned} I_g &\propto \frac{1}{2}|\Psi_\mathrm{A}+\Psi_\mathrm{B}|^2 \\ &= \frac{1}{2}(|\Psi_\mathrm{A}|^2+|\Psi_\mathrm{B}|^2)+(\mathrm{Re}\Psi_\mathrm{A}\mathrm{Re}\Psi_\mathrm{B}+\mathrm{Im}\Psi_\mathrm{A}\mathrm{Im}\Psi_\mathrm{B})\,, \qquad (5.1) \\ I_u &\propto \frac{1}{2}|\Psi_\mathrm{A}-\Psi_\mathrm{B}|^2 \\ &= \frac{1}{2}(|\Psi_\mathrm{A}|^2+|\Psi_\mathrm{B}|^2)-(\mathrm{Re}\Psi_\mathrm{A}\mathrm{Re}\Psi_\mathrm{B}+\mathrm{Im}\Psi_\mathrm{A}\mathrm{Im}\Psi_\mathrm{B})\,. \qquad (5.2) \end{aligned}$$

Here, I is the photoelectron intensity at the position of the detector, Ψ_A and Ψ_B are the wave functions of the outgoing electron emitted from center A respectively B, and $\mathrm{Re}\Psi$ and $\mathrm{Im}\Psi$ are the real and imaginary part of the wave function Ψ. Obviously, the angular distributions are different for emission from the *gerade* ($1\sigma_g$) and *ungerade* ($1\sigma_u$) state due to the fact that the coherently emitted waves Ψ_A and Ψ_B interfere as explained qualitatively in section 5.1.[c] The respective MPADs and the interference term $\mathrm{Re}\Psi_\mathrm{A}\mathrm{Re}\Psi_\mathrm{B}+\mathrm{Im}\Psi_\mathrm{A}\mathrm{Im}\Psi_\mathrm{B}$ calculated in the MSNSP formalism (see Appendix B) for electron emission on the shape resonance are shown in fig. 5.3.[d]

Due to the strict observation of the parity selection rule within the dipole approximation, the partial wave composition of the outgoing photoelectrons is limited to partial waves with *odd* angular momentum number l for emission from the $1\sigma_g$ state, and to partial waves with *even* l for emission from the $1\sigma_u$ state. As the Legendre polynomials $P_l(\cos\theta)$ with odd l are zero at $\theta = 90°$, the MPAD of the gerade state shown in fig. 5.3(a) reaches zero

[b] All formulas and concepts can, in principle, be generalized for an arbitrary number of identical atoms.

[c] For the energies considered here, the small difference in kinetic energy of $\approx 100\,\mathrm{meV}$ between the photoelectrons emitted from the $(1\sigma_g)$- and the $(1\sigma_u)$-state does not change their scattering noticeably. It may play a role for very low photoelectron kinetic energies below 1 eV.

[d] Other recent theoretical calculations of the K-shell photoionization of N_2 based on the *Random Phase Approximation* (RPA)[234–237] as well as the configuration interaction (CI) method[238,239] also show different angular distribution patterns for the gerade and ungerade state,[90,167,245] but do not explicitly mention the subject of coherent emission.

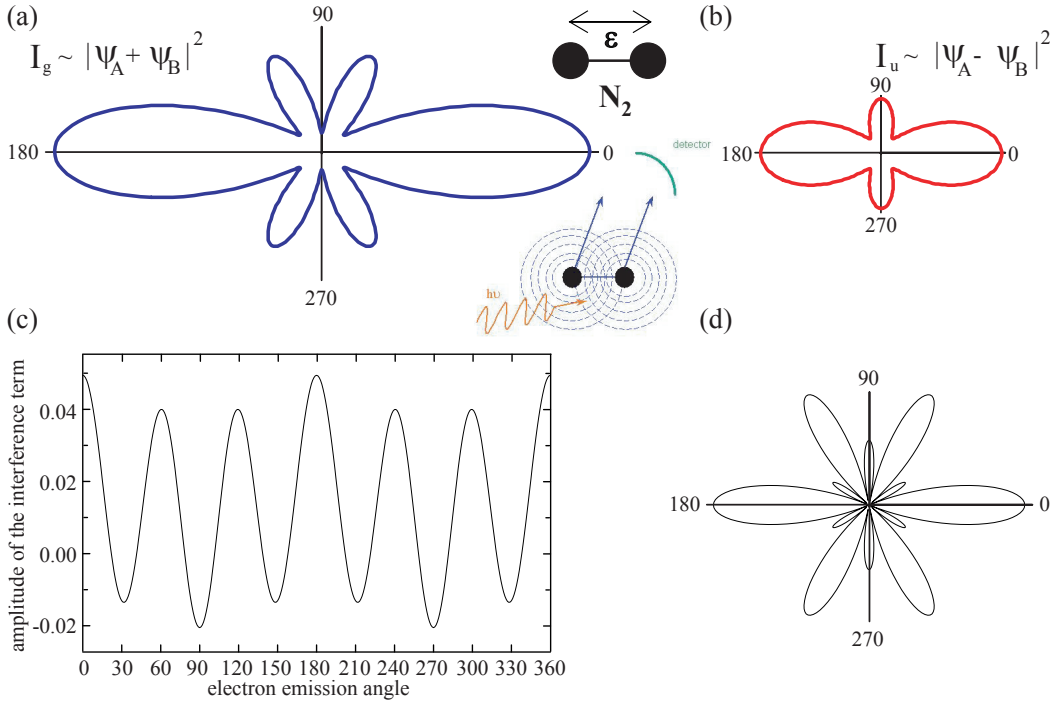

Figure 5.3: K-shell photoelectron angular distribution of N_2 at $h\nu$ = 419 eV (E_{kin} = 10 eV) with linearly polarized light with the $\boldsymbol{\varepsilon}$-vector parallel to the molecular axis calculated in the *coherent model*: **(a)** emission from the gerade state, **(b)** emission from the ungerade state; **(c)** interference term from eq. (5.1) and (5.2) marking the difference between emission from the gerade and ungerade initial state, **(d)** *absolute value* of the interference term as a polar plot.

for emission perpendicular to the molecular axis. Furthermore, a strong contribution of the f-partial wave to the shape resonance leads to the previously discussed pronounced maxima at 60° and 120° with respect to the molecular axis,[63,80] which occur only in the gerade pattern.

An experimental verification of these predictions by the coherent emission model is rather difficult since the kinetic energy difference between the photoelectrons from the $1\sigma_g$ and $1\sigma_u$ state is only $\approx 100\,\text{meV}$[46] compared to a total kinetic energy of roughly 10 eV when measuring on the shape resonance. Additionally, the core hole state has a very short life time due to the fast subsequent Auger decay, resulting in a natural line width of the $N_2N{:}(1s)$ photo line in the same order as the energy splitting.[46] Hence, none of the existing coincidence experiments have been able to resolve the splitting between those two states, and all existing experimental MPADs in the literature are the (incoherent)[e] *sum* of the patterns obtained for the gerade and the ungerade state:

$$\begin{aligned} I_{g+u} &= I_g + I_u \propto |\psi_g|^2 + |\psi_u|^2 \\ &= \frac{1}{2}|\psi_A + \psi_B|^2 + \frac{1}{2}|\psi_A - \psi_B|^2 \\ &= |\psi_A|^2 + |\psi_B|^2 \,. \end{aligned} \tag{5.3}$$

[e] Since every single electron is either emitted from the gerade *or* ungerade state, the sum of both contributions is incoherent.

As this simple equation shows, the interference term vanishes if the gerade and ungerade states are not resolved, and the resulting expression is identical to the *incoherent* sum of *localized* emission from site A and B:

$$I_{A+B} = I_A + I_B \propto |\Psi_A|^2 + |\Psi_B|^2 . \tag{5.4}$$

The equivalence of the two models in the case of *unresolved* photoemission is also illustrated in fig. 5.4, where the resulting MPADs are compared to the unresolved experimental patterns by Jahnke *et al.*[167] The theoretical angular distribution patterns for *localized* emission from atom A respectively B also calculated in the MSNSP formalism are shown as well. They look quite similar to the asymmetric MPADs of a heteronuclear molecule such as CO (see fig. 4.8), where the emission process is naturally localized.

These results prove that in contrast to the opposite conclusion by Pavlychev *et al.*,[85] a good agreement between calculations and experimental data is also possible in the incoherent model. The incoherent calculations by Dill *et al.* [80] underestimate the intensity for the 60° and 120° maxima mostly because of to the rather simple approximation of the scattering potential and *not* because they are based on an incoherent picture. As a matter of fact, as demonstrated above, the theoretical results from the coherent and incoherent model are mathematically identical *if*

1. the sum over both initial states, gerade and ungerade, is considered,
2. an identical scattering potential is used for the coherent and incoherent model,[f]
3. a symmetric ionic final state, e.g. N^+ - N^+ is assumed.

Exploring the last aspect further, it is theoretically possible that a localized emission might be observable when selecting an *asymmetric* break-up, e.g. a decay into a doubly charged N^{++} and a singly charged N^+ fragment or into a doubly charged N^{++} and a neutral N fragment rather than the symmetric fragmentation channel into two singly charged fragments. If one assumes that there is a higher probability that the photoelectron is emitted from the atom which ends up as a N^{++} ion, this should "switch off" the interference seen in the N^+ - N^+ channel by "pinning down" the core hole, i.e. the origin of the electron, to one of the two atoms and thereby destroying the indistinguishability, comparable to a two-slit experiment in which the observer knows the path of the particle. Measuring the MPAD of such an asymmetric fragmentation channel would yield an asymmetric angular distribution similar to the ones shown in fig. 5.4. However, experiments have shown that the *asymmetric* N^{++} - N^+ channel [g] has the same *symmetric* photoelectron distribution as the N^+ - N^+ fragmentation channel.[157] While this might seem surprising at first, it is easily explainable

[f] In the present calculations, a symmetric scattering potential was assumed.

[g] The N^{++} - N^+ events can be recorded in an ion-ion-electron *triple coincidence* experiment and are therefore clearly characterized.

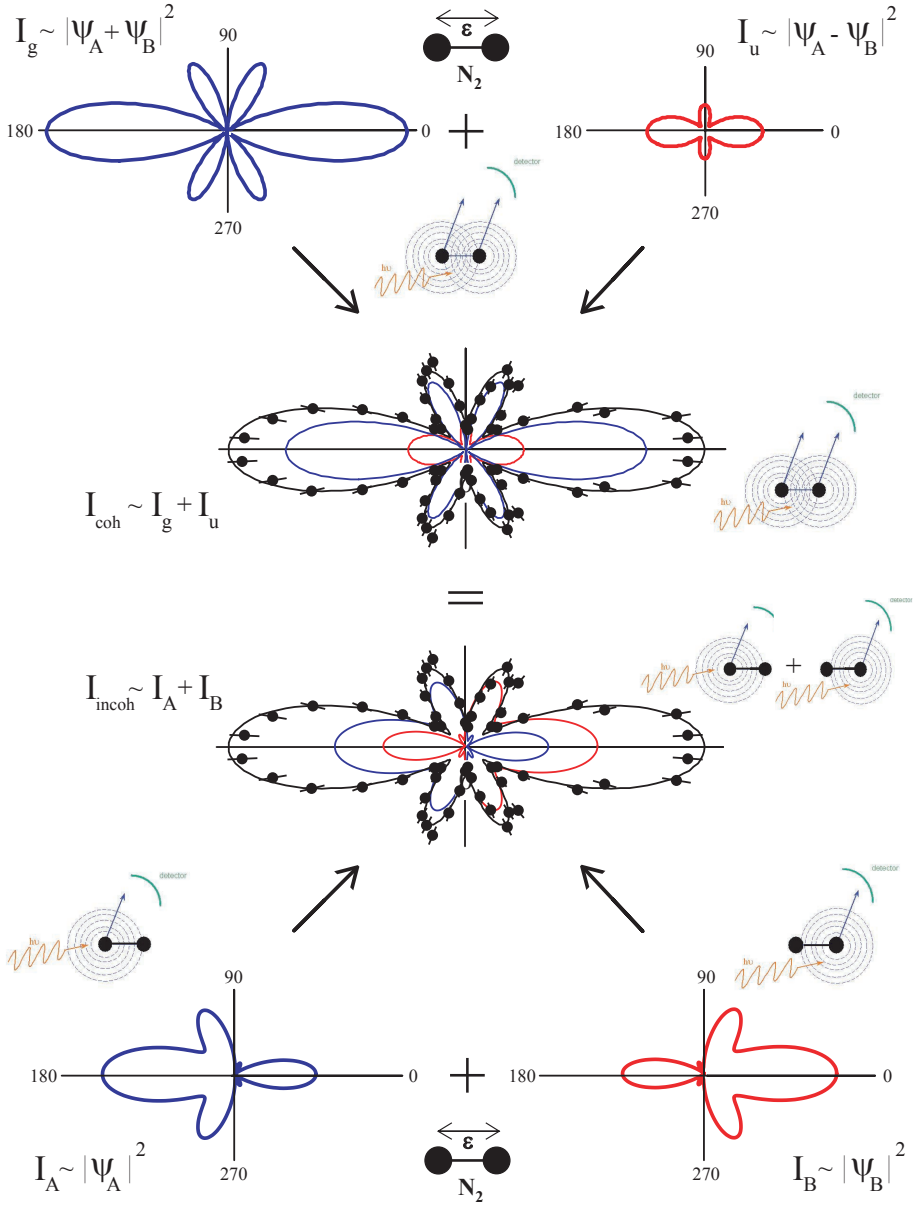

Figure 5.4: Calculated results in the incoherent as well as coherent model compared to the unresolved experimental patterns by Jahnke *et al.*[167] The orientation of the molecular axis is parallel to the $\boldsymbol{\varepsilon}$-vector and the kinetic energy of the photoelectrons is 10 eV.

when considering the fact that the Auger decay which fills the initial core hole happens *before* the molecule fragments and that the relaxing electron originates from a *delocalized, molecular* valence orbital. The final charge distribution consequently does *not* reflect the position of the initial core hole and a hole localization, or breaking of the coherence, via the Auger decay cannot be expected.

Having discussed all of the above, the very fundamental and conceptual, almost philosophical question of the *underlying reasons* for coherence and incoherence and how coherence can break down or is established in the first place still remains unsolved. Different models starting from quite *opposite first assumptions* have been proposed: One approach assumes that the photoionization process is *at the very first instant incoherent* and *localized*, and coherence can only be established depending on the time scale involved in the measurement. Gadzuk for instance started with this assumption and concluded that a *narrow energy window* connected to a long *characteristic time of the measurement* establishes coherence because the hole can delocalize via *hopping*.[219] Interpreting the experimental angular distributions for N_2, Pavlychev *et al.* also assumed an initially incoherent and localized process and claimed that the subsequent hole relaxation, i.e. Auger decay, re-establishes the symmetry of the molecule which was broken by the *localized* photoionization, thereby establishing the coherence if the *time scale of the relaxation* is fast compared to some characteristic *escape time* of the photoelectron.[85]

However, the opposite picture, in which the process *starts off coherently* and *delocalized* because of the non-local nature of the core orbitals, is also possible. In fact, this picture corresponds best to the previously described two-slit model, in which coherence and interference can be observed because the process is *a priori* indistinguishable, and coherence and interference only break down if this indistinguishability is destroyed.

5.3 Angle Resolved High-Resolution Photoelectron-Photoion Coincidence Experiments

In order to verify the prediction of the coherent electron emission model presented above, a high-resolution coincidence experiment is required, which is able to resolve the gerade and ungerade states and their splitting of only 100 meV, and to determine if they have indeed different angular distribution patterns.

Such measurement was performed in the single bunch mode at BESSY (UE56/2-PGM1 and UE56/1-PGM) and the two bunch mode at HASYLAB (BW 3) using an effusive nitrogen gas jet (99.999% purity) and five rotatable electron time-of-flight analyzers mounted in the "dipole plane" perpendicular to the light propagation direction opposite to a position-sensitive ion time-of-flight spectrometer (see fig. 5.5 as well as fig. 3.5 in chapter 3.3). Since the N_2:N(1*s*)-doublet with a splitting of less than 100 meV[46] had to be resolved while data were acquired over several hours or even days, the experiment required extremely high

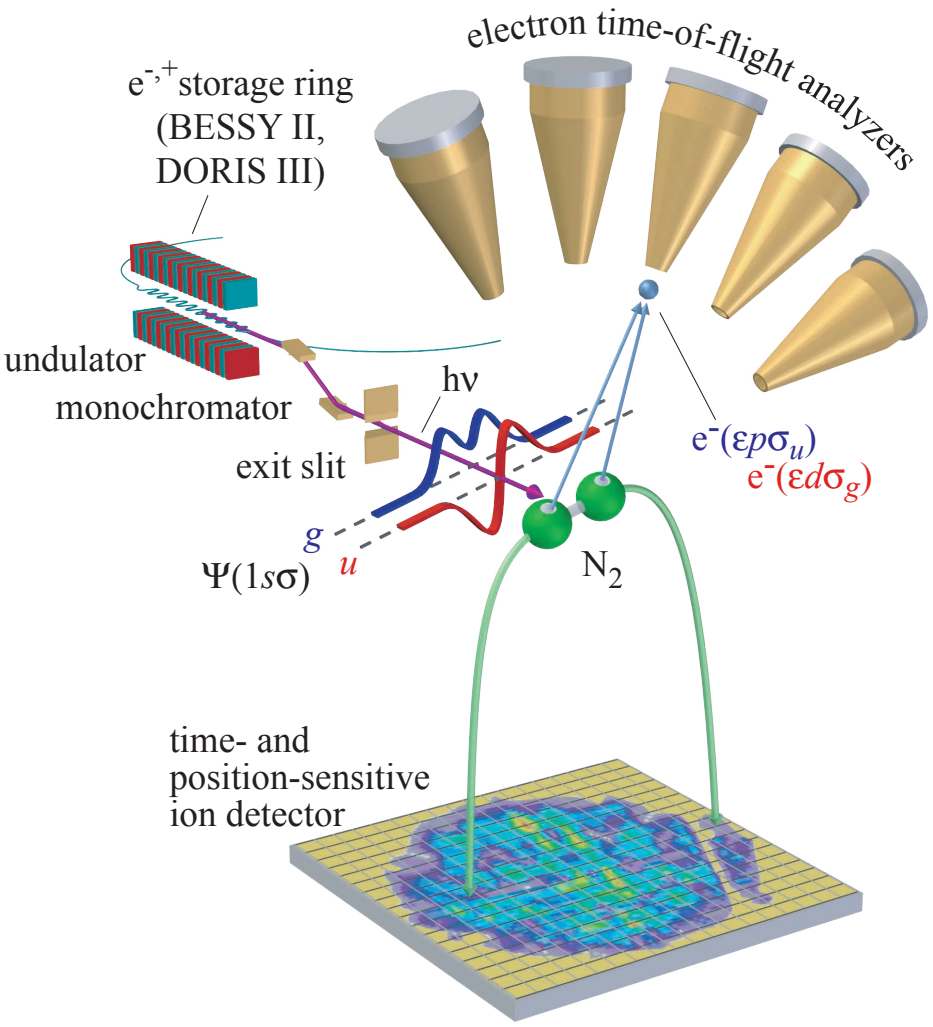

Figure 5.5: Schematics of the high-resolution photoelectron-photoion coincidence experiment resolving the gerade and ungerade core states of N_2.

energy resolution of both the beamline and the spectrometers as well as a very high photon beam stability. Thus, data were recorded for 30 minutes at a time while the long-term stability of the photon energy and beam position was monitored via repeated high-resolution scans of the N_2:N(1*s*) $\rightarrow$ π^* resonance and kept within a range of ± 5 meV of the nominal measurement energy. A retarding voltage was applied to the drift region of the electron analyzers in order to obtain high energy resolution (in the present case ≈ 40 meV for 10 eV electrons). The transmission and efficiency of the electron analyzers was determined using Ne and He calibration spectra covering the energy region of interest and normalizing the Ne(2*p*) and (2*s*) respectively He(1*s*) and n=2 satellite lines with the known cross sections and angular distributions.[240,241] Very similar results were obtained using a set of electron spectra of the Ar(2*p*) photoelectron line[242] and the corresponding Ar LMM Auger lines. The photon energy was calibrated using the literature values for the N_2:N(1*s*) $\rightarrow$ π^*, the He ($2,0_2$) and the Ar(2*p*) inner-shell resonances.[243,244] After the data collection, all spectra were converted from the time to the energy coordinate and corrected for transmission effects. The position of the N_2:N(1*s*) photo line in each of the 30-minute spectra was

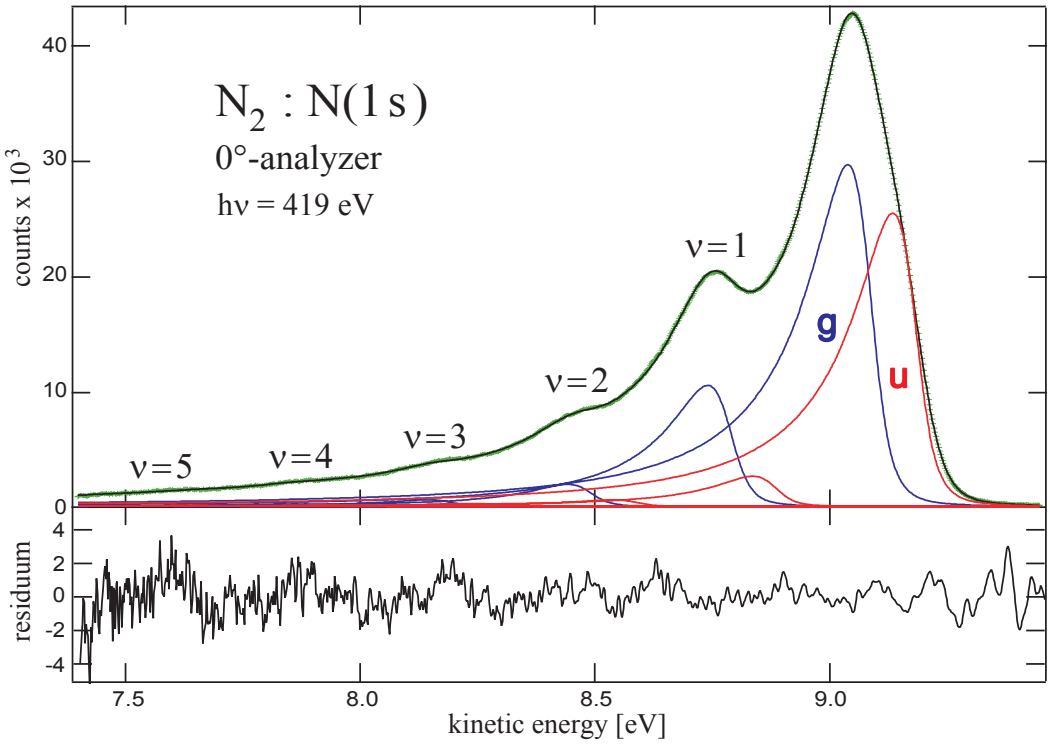

Figure 5.6: High-resolution photoelectron spectrum of N_2 recorded at a photon energy of $h\nu$ = 419 eV at 0° with respect to the polarization vector. The measured spectrum (green line) in the range of the 1*s* photo line is shown together with a least-square fit of the gerade (blue) and ungerade (red) components and their respective vibrational progression up to the fifth vibrational level. The black line shows the resulting fit curve convoluted with the photon energy and spectrometer resolution, while the individual components are shown before convolution with the apparatus profile.

analyzed and small shifts were compensated by shifting the spectrum accordingly, if necessary. For the coincidence spectra, random coincidences were subtracted via an algorithm using coincidence spectra triggered by a random pulse generator as explained in chapter 3.6. Finally, the intensities of the gerade and ungerade components of the N_2:N(1*s*) line were determined by means of a least-square fit of the final spectra with a doublet of PCI-deformed peaks including vibrational progression as done by Hergenhahn *et al.*[46] For the $1\sigma_g$-$1\sigma_u$ splitting, a value of 96 ± 3 meV was determined, and a value of 300 ± 3 meV was found for the vibrational energy. Both are in agreement with the measurements by Hergenhahn *et al.* as well as theoretical predictions by Kosugi[47,48] and Thiel *et al.*[258] A complete list of all relevant fit parameters and a comparison to the values of Hergenhahn *et al.* is given in table 6.1 in chapter 6.1. In order to obtain the angular distributions, i.e. the intensities in the different analyzers, the $1\sigma_g$-$1\sigma_u$ splitting, the natural line width and the shape of the PCI-profile were set to the same value for all angles, while the vibrational energy and the intensities of all vibrational components as well as the experimental resolution were allowed to vary individually.

Fig. 5.6 shows the measured N_2(1*s*) photo line in the 0°-analyzer together with the results of the least-square fit. The corresponding molecule frame angular distribution patterns are shown in fig. 5.7 for the two cases of the molecular axis parallel to the light polarization

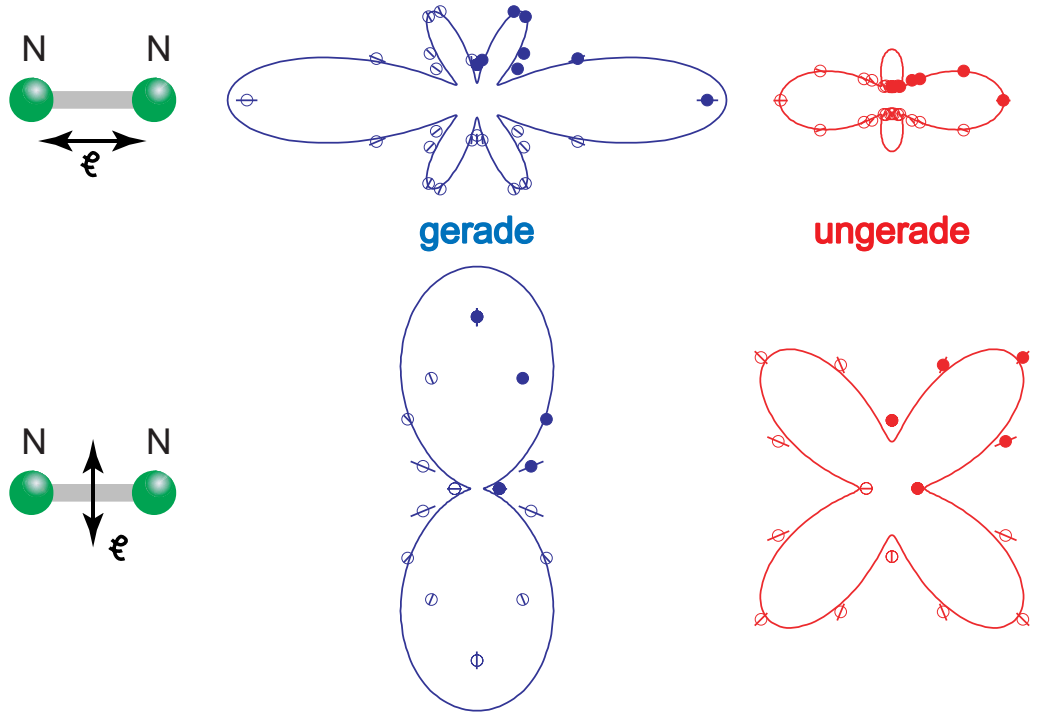

Figure 5.7: Molecule frame photoelectron angular distributions of the gerade (blue) and ungerade (red) symmetry components of the N_2:N(1*s*) photo line at a photon energy of hν = 419 eV measured in the plane perpendicular to the light propagation direction for molecules oriented parallel (top) and perpendicular (bottom) to the light polarization vector (the parallel and perpendicular patterns are not plotted on the same scale). The open circles are the mirror image of the measured data points (full circles) which are obtained by a least-square fit of the coincident spectra. The error bars reflect the statistical uncertainty of the fit. The solid lines are predictions for non-local, coherent electron emission calculated in the MSNSP approach (see section 5.2 and Appendix B).

as well as perpendicular together with predictions for coherent emission calculated in the MSNSP approach as discussed in section 5.2.

In order to account for interchannel coupling (IC) effects, which were found to be of importance for the core photoionization of N_2[46,90,245] but which are not included in the one-particle MSNSP calculation (see Appendix B), the relative intensity of g and u in the calculation was adjusted empirically to fit the experimental data. More precisely, the calculated ungerade MPAD was multiplied by a factor of 1.15, which, in turn, can be interpreted as a measure for the strength of the IC in this case. The value supports the conclusions by Lin *et al.*[245] and Hergenhahn *et al.*[46] who found that the size of the IC is considerably smaller than initially predicted by Cherepkov *et al.*,[90] who had reported an IC induced increase of the ungerade cross section at the shape resonance by almost 100%.

Apart from some differences at certain emission angles, in particular at 90° with respect to the molecular axis, the molecule frame angular distribution patterns shown in fig. 5.7 agree very well with the coherent prediction, proving that the emission process is indeed coherent and delocalized, or - more precisely - non-localized in a quantum mechanical sense, and that it can therefore be interpreted as a molecular two-slit experiment. The indistinguishability of the emission pathways caused by the inversion symmetry of

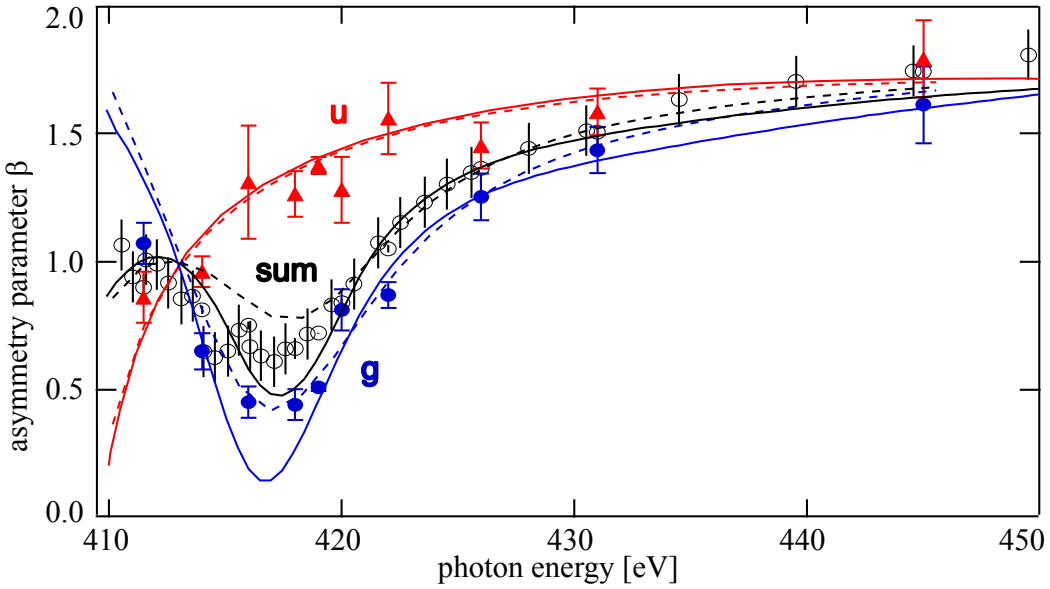

Figure 5.8: Photoelectron angular distribution asymmetry parameter β for the N_2:N(1*s*) photo line. The symbols represent the experimental data for the gerade (blue circles) and ungerade (red triangles) state as well as their unresolved sum (open black circles). The results are compared to calculations in the partially relaxed core Hartree-Fock (RCHF)[196] (solid lines) and the Kohn-Sham Density Functional Theory (KS-DFT) approach (dashed line).[246]

the molecule leads to coherent emission of photoelectron waves from both molecular centers and to the resulting characteristic interference patterns in the $1\sigma_g$ and $1\sigma_u$ molecule frame photoelectron angular distributions reflecting the pure *l*-odd or *l*-even character of the gerade and ungerade core hole state imposed by the parity selection rules (see section 5.2).

Additionally, the measurements also allows to determine for the first time the photoelectron angular distribution parameter β of the gerade and ungerade components of the N_2:N(1*s*) photo line (see chapter 2.4.2). Their symmetry-specific difference is particularly pronounced in the region of the shape resonance because of the dominance of the f-partial wave in the gerade channel (fig. 5.8).[63,80]

The gerade/ungerade-resolved measurement of both the angular distribution parameter and, in particular, the molecule frame angular distributions clearly demonstrate the coherent nature of the electron emission. While the angular distribution of the unresolved 1*s* photo line can also be explained in an incoherent model, the behavior of the two individual symmetry components requires a coherent description of the emission process.

5.4 Photoelectron Diffraction from Free Homonuclear Molecules

Having established the coherent emission model for the N_2 core photoelectron emission by the experiments described above, the question arises how the coherent nature of the process affects the *photoelectron diffraction*, which was discussed for the heteronuclear molecule CO in chapter 4. Contrary to the case of CO, where only one initial wave is

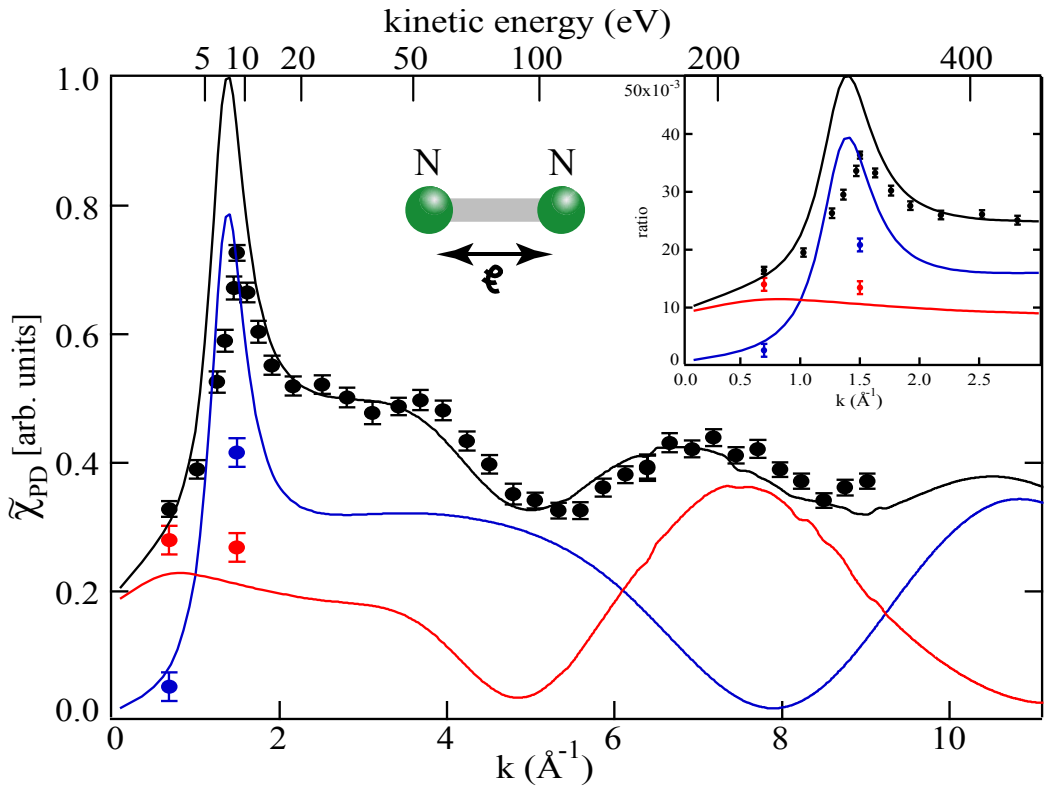

Figure 5.9: N(1*s*) photoelectron diffraction from free N_2 molecules. The blue circles are the gerade component, the red circles ungerade, and the black circles the unresolved photo line. The lines are calculations in the partially relaxed-core Hartree-Fock (RCHF) approximation.[195]

emitted and then scattered on the neighboring atom, *two* electron waves starting from one of the two centers of the molecule each have to be taken into account. The interference described in the previous sections can thus be expected to also affect the photoelectron diffraction behavior. This effect is particularly interesting since it cannot be observed easily for molecules adsorbed on a surface, where the bond to the surface breaks the symmetry of the molecule by inducing a chemical shift on the core orbital of the atom which is closest to the surface. Hence, the photoelectron diffraction of an undisturbed homonuclear molecule is best studied in a gas phase experiment. Fig. 5.9 shows the results of such an experiment together with calculations in the RCHF model.[h] Similar to the case of CO, strong oscillations occur with a period that is related to the bond length of the molecule. However, due to the non-local electron emission and the equivalence of the two atomic constituents, it is impossible to distinguish between forward and backward scattering channels. Instead, two different curves for emission from the *gerade* and *ungerade* states appear, both with a pronounced modulation, but shifted by approximately half an oscillation period with respect to each other. The modulation period of these g/u-resolved curves is roughly twice as long as in CO, i.e. it reflects only the *single* bond length rather than twice the bond length

[h] Note that the depicted photoelectron diffraction ratio $\tilde{\chi}^0_{PD}$ as defined in eq. (4.3) in section 4.1 still includes a photon energy dependent angular effect introduced by the normalization to the non-coincident photoelectron intensity.

as in the case of CO. Because of the required photon and electron kinetic energy resolution, it is very challenging to experimentally resolve the gerade and ungerade components for electron kinetic energies above 10 eV, and the g/u-resolved data are therefore currently limited to two data points at low kinetic energy. As can be seen in the unresolved sum, the calculation overestimates the effect of the shape resonance at these energies. Neglecting this effect which affects mostly the gerade channel, at least a qualitative agreement between theory and experiment can be noted. In particular, both theory and experiment show an inversion of the gerade-ungerade intensity ratio for low photoelectron kinetic energies. With the exception of a small offset, the agreement between theory and experiment for the *g/u-unresolved* line is excellent above the shape resonance.

The doubling of the modulation period of the g/u-resolved curves compared to the case of CO can easily be explained considering the geometry of the coherent electron emission (see fig. 5.1). As described in section 5.1, the electron waves emitted coherently from the two centers of the molecule pick up an angle dependent path length difference. Contrary to the case of CO, where only one initial wave is emitted and then scattered on the neighboring atom, picking up a path length difference of twice the bond length for emission along the molecular axis (see chapter 4.1), the maximum path length difference between the two simultaneously emitted waves in N_2 is only the single bond length. The shift between the gerade and ungerade is mainly due to the fact that the two coherent emitters emit either in phase (gerade) or with a phase difference of π (ungerade). When the unresolved photo line, i.e. the sum of g and u, is considered, an oscillation with twice the period is displayed, and a situation similar to the diffraction on CO, which is based on a localized electron emission, is mimicked. This is in agreement with the previous findings that the interference effect based on the coherent electron emission in N_2 cancel and that the emission process can be described in a localized picture when only the unresolved photo line is observed. Only a study of the *resolved* gerade and ungerade components reveals the conceptual difference between the emission process in CO and N_2. The resolved case demonstrates that while the diffraction in CO is a pure final state scattering effect, the equivalent process in N_2 is dominated by the coherence and interference of the inversion symmetric initial state.

Based on these findings, the question arises whether the coherent and non-local photoelectron emission and the non-local character of the core hole can be affected if the symmetry of the system is destroyed. While the selection of an *asymmetric* fragmentation channel as discussed in section 5.2 does not affect the emission character, a different approach, namely symmetry breaking by isotope substitution, is discussed in the following chapter.

Chapter 6

Isotope Substitution: From Homo- to Heteronuclear via Symmetry Breaking

Isotope substitution is a powerful, yet sensitive way to alter certain quantum mechanical properties of a molecule in a clearly characterizeable and well defined manner. It is therefore commonly used in a wide range of physical, chemical and biological applications, e.g. to study nuclear spin effects, or to label certain molecules or molecular sites. Isotope effects are hence extensively studied in molecular spectroscopy on a vast range of systems from the simple hydrogen molecule to large organic and bio-molecules.

In the field of photoelectron spectroscopy, most studies are done on H_2, HD and D_2[247] and on the valence shell of some other molecules.[248–252] Generally speaking, one can group the consequences of isotope substitution in four classes:

- pure mass effects, which affect the vibrational and rotational constants, the position of the photo line, as well as the Franck-Condon factors,[247,253]
- nuclear spin effects on the hyperfine structure,[254]
- symmetry effects on the rotational structure,[255,256]
- possibly effects on the electronic wave function due to the symmetry breaking.

The first three are well known and widely studied, and are discussed only briefly in the following. However, isotope effects on the electronic wave function due to the symmetry breaking are much less explored, and the results and discussion presented in chapter 6.2 through 6.4 represent the first observation of such an effect in the photoelectron spectrum of a diatomic homonuclear molecule.

6.1 Isotope Effects on the Nuclear Dynamics

Replacing one or both atoms in a molecule by a different isotope changes the reduced mass μ of the system and consequently leads to an altered vibrational energy $\hbar\omega$. For the hydrogen molecule and for hydrogen compounds, this is a drastic change, while the relative size of the effect reduces rapidly for heavier molecules. For the case of N_2, a simple harmonic oscillator model (see Appendix C) predicts a change of the vibrational energy from 300 meV in $^{14}N_2$ to 295 meV in $^{14,15}N_2$ respectively 290 meV in $^{15}N_2$. This agrees very well with the experimental values determined by a least-square fit of the high-resolution electron spectra of the three isotopomers (see table 6.1).[a]

	Hergenhahn	present experiment		
(all values in meV)	$^{14}N_2$	$^{14}N_2$	$^{14,15}N_2$	$^{15}N_2$
g-u splitting	97 ± 3	96 ± 3	96 ± 3	96 ± 3
vib. energy ($\hbar\omega$)	295 ± 5	300 ± 3	295 ± 3	290 ± 3
exp. resolution	55 ± 5	(65 ± 5)[a]	(68 ± 5)[a]	(65 ± 5)[a]
lifetime broadening	102 ± 10	(128 ± 5)[a]	(125 ± 5)[a]	(128 ± 5)[a]

Table 6.1: Results of the least square fit of the N_2:N(1*s*) photoelectron spectra of the three N_2 isotopomers compared to the results obtained for $^{14}N_2$ by Hergenhahn *et al.*[46] The errors given here represent the uncertainties of the absolute values, which reflect mostly the uncertainty of the kinetic energy scale. When comparing the values for the different isotopomers, e.g. the different vibrational energies $\hbar\omega$, the error of the values relative to each other is in the order of 1 meV. The experimental results agree well with the theoretical values of 96.3 meV[47] respectively 101 meV[258] for the g-u splitting and the predicted vibrational energies $\hbar\omega_g$ = 302.5 meV and $\hbar\omega_u$ = 302.1 meV[258] in $^{14}N_2$.

The relative change of the vibrational energy is in the order of a few percent and is barely visible in the photoelectron spectrum (fig. 6.1, top panels), but it can be nicely displayed in the *ratio* of the photoelectron spectra of the regular and the isotope substituted species, as shown for example for "normal" $^{14,14}N_2$ and isotope substituted $^{14,15}N_2$ in the bottom panel of fig. 6.1. The smaller vibrational constant in $^{14,15}N_2$ leads to pronounced oscillations in the intensity ratio, which coincide with the position of the vibrational progression. The effect can be simulated by shifting the fitted $v > 0$ vibrational components of $^{14,14}N_2$ by 5, 10, 15, etc. meV respectively, and then taking the ratio of the original and the modified spectrum. This simulated ratio (dashed line) reproduces the oscillations for

[a] The fit was performed with the same fit model and the fit routine as used by Hergenhahn *et al.*[46] In addition to the intensities of all vibrational components, which were allowed to vary independently from each other, the g-u line splitting, the vibrational energy, the experimental resolution (a Gaussian representing both photon energy resolution as well as spectrometer resolution), and the lifetime broadening (with Lorentzian line shape) were fitted. While the quality of the fit is excellent, an interdependence of the parameters "experimental resolution" and "lifetime broadening" can be observed. Consequently, these two fit parameters lose their original physical interpretation. Apparently, the total apparatus resolution function has the shape of a Voigt profile rather than a pure Gaussian, which is compensated in the fit by an unrealistically high value of the Lorentzian "lifetime broadening". Such a Voigt shape of the apparatus function was also found by previous high-resolution studies on the BESSY plane grating monochromators.[257] However, apart from the falsified values for the "lifetime broadening", the fit model is still very well suited to describe the line shape of the photo line, and the values obtained for the other parameters are in very good agreement with the previous measurement as well as with the theoretical predictions.

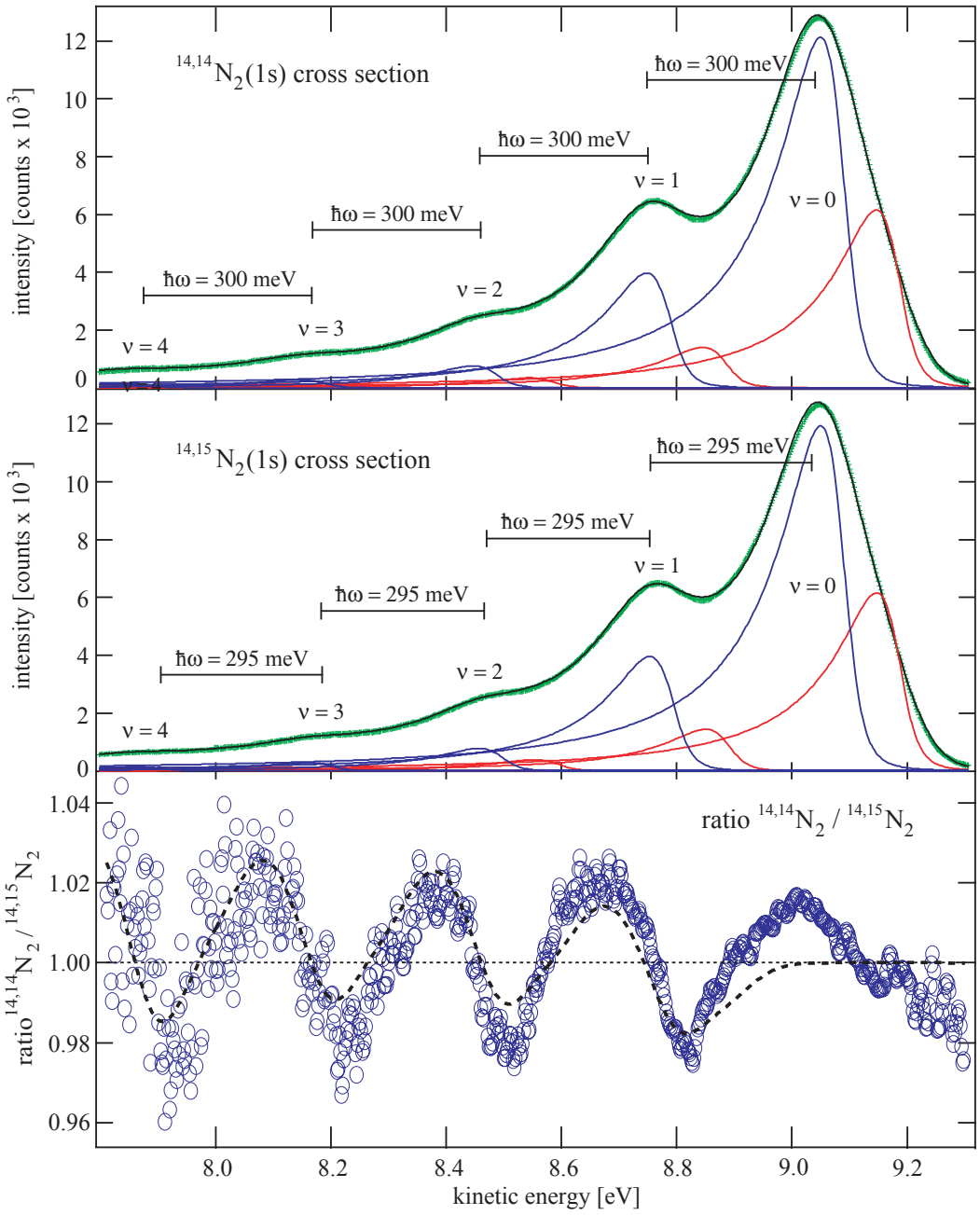

Figure 6.1: $^{14,14}N_2$:N(1s) and $^{14,15}N_2$:N(1s) photoelectron spectra measured at a photon energy of hν = 419 eV at the quasi-magic angle (θ_e = 54.7° with respect to polarization vector), where all angular effects cancel and the measured photoelectron intensities are equal to the partial cross sections. The ratio of the two spectra in the range of the N_2:N(1s) photo line is shown at the bottom. The oscillations in the ratio below 9 eV are caused by a decrease of the vibrational energy $\hbar\omega$ in the isotope substituted species. The dashed black line in the bottom panel is a model calculation of this vibrational effect (see text). It describes the oscillations for the $\nu > 0$ components very well, but fails to reproduce the additional "wiggle" at the position of the $\nu = 0$, which therefore cannot be explained by the change of the vibrational energy.

the $v > 0$ components very well, but fails to explain the additional "wiggle" at the position of the $v = 0$, which is discussed in the following section.

The altered reduced mass also leads to an altered zero-point vibrational energy and thereby to an absolute energy shift of the photo line, which can sometimes even be observed in core electron spectroscopy.[253] For molecular nitrogen, this shift is in the order of less than a tenth of a meV (see Appendix C) and is far beyond the reach even of this high-resolution and high-precision measurement.

A change of the reduced mass can also affect the Franck-Condon factors, or, in other words, the intensity distribution of the vibrational components with respect to each other. In addition to the smaller vibrational energy, the *offset* between the potential curves of the ground and excited state, which is expressed in the normal coordinate $Q = \sqrt{\mu}R$, increases in the substituted molecule due to the higher reduced mass. Higher vibrational excitations hence become stronger compared to the non-substituted case, while the $v = 0$ loses some intensity (see chapter 2.2.1).[253] This effect is analyzed quantitatively in section 6.3.

On the rotational level, isotope substitution can have dramatic effects: In a diatomic molecule with identical nuclei, symmetry constraints influence the statistical weight of the rotational lines in such a way that every other line is relatively weak or even missing, a phenomenon known as *alternating intensities*.[255,256,259,260] If the indistinguishability of the nuclei is destroyed, the symmetry selection rules collapse and all forbidden or suppressed rotational transitions become equally allowed.[255,256] Apart from this drastic effect, a change in the reduced mass due to isotope substitution also changes the rotational constant, of course. However, as rotational resolution is beyond the reach of present-day core level photoelectron spectroscopy, both effects remain hidden in the present experiment. This is also true for the isotope induced changes in the hyperfine structure (HFS).[254]

6.2 Isotope Effects on the Electronic Wave Function

As isotope substitution does not affect the nuclear charges and therefore does not alter the Coulomb potential in which electrons move, the Born-Oppenheimer approximation of complete decoupling between nuclear and electronic motion suggests that no change should occur on the electronic wave function.[b] However, the discussion of non-locality and coherence effects in the previous chapter raises the question whether a breaking of the symmetry constraints that lead to the non-locality and coherence could also break the non-local and coherent emission character and thus affect the electronic wave function. In order to study this hypothesis, the high resolution photoelectron spectra of the N(1*s*) photo line of the naturally abundant $^{14}N_2$ and the two isotopomers $^{14,15}N_2$ ("single label nitrogen"

[b] Known violations of the symmetry rules for the ground vibrational and electronic state of homonuclear diatomic molecules are miniscule,[261] and a symmetry breaking has been observed for highly excited states only.[254,262–265]

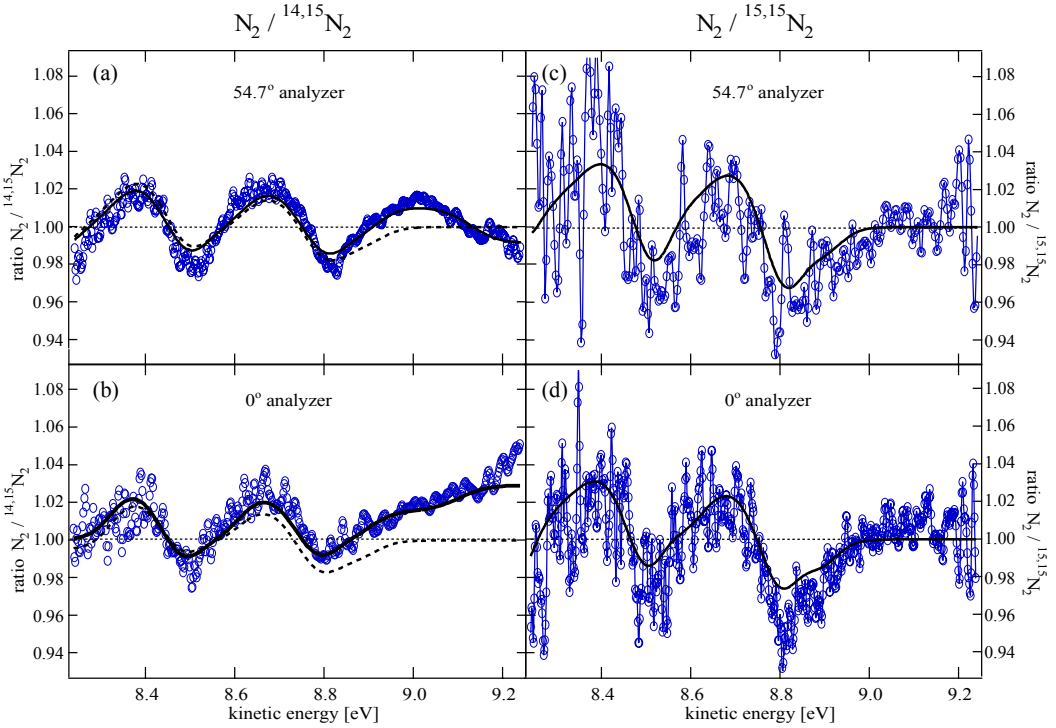

Figure 6.2: Spectral ratio between the naturally abundant $^{14,14}N_2$ and isotope substituted $^{14,15}N_2$ (left) respectively $^{15,15}N_2$ (right) for the photoelectron intensity at the quasi-magic angle (top) and at 0° to the light polarization (bottom) measured at $h\nu = 419$ eV. The solid lines are model calculations which include the vibrational effect and, for $^{14,15}N_2$, also the effect of the symmetry breaking (see text). For $^{14,15}N_2$, the dashed line shows a modeling of the vibrational effect only.

with 99 % purity purchased from ICON Isotopes) and $^{15}N_2$ (99 % purity purchased from Sigma Aldrich) were measured. The experiments were performed at beamline BW3 of HASYLAB and beamlines UE56/2-PGM1 and UE56/1-PGM at BESSY; the experimental setup and the data taking and analysis procedure was similar to the one described in the previous chapter, except that the (coincident) detection of the fragment ions was switched off in order to be able to use higher gas pressures and higher count rates. Moreover, the sample gas was changed from the isotope substituted to the normal species or vice versa at least once during each fill of the storage ring, so that medium and long term drifts and instabilities would affect both measurements to the same degree.

Again, the effects of the isotope substitution are best illustrated in the ratios of the photoelectron spectra of normal and substituted nitrogen (scaled to the same total intensity), which are shown in fig. 6.2 and 6.3 (in the latter, the experimental data are strongly rebinned). In addition to the previously discussed change of the vibrational energy, the additional "wiggle" at the high-energy end of the $N_2/^{14,15}N_2$ ratio is visible both in the ratio at the quasi-magic angle (fig. 6.2(a)) as well as at 0° to the light polarization (fig. 6.2(b)), but does *not* appear in the $N_2/^{15,15}N_2$ ratio (fig. 6.2(c)+(d)). This can only be explained by a change in both cross section as well as angular distribution of the g and u components in the singly-substituted $^{14,15}N_2$ compared to the two other isotopomers. A simulation including these changes (solid lines) reproduces the experimental data even at the high-energy

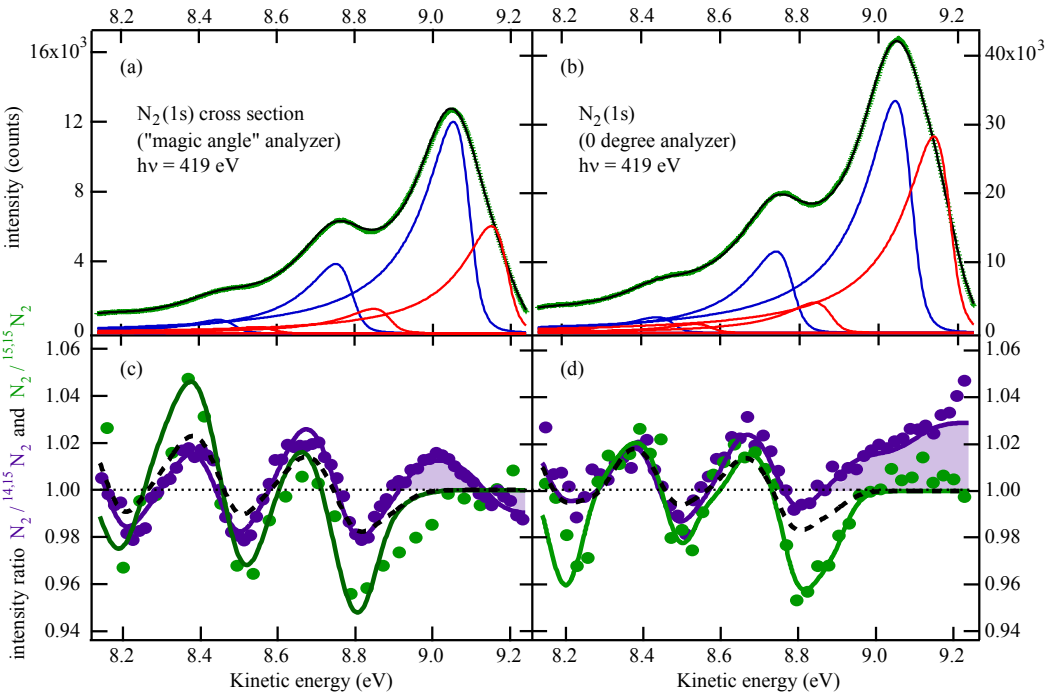

Figure 6.3: N_2:N(1s) photoelectron spectrum at hν = 419 eV measured (a) at the quasi-magic angle and (b) at 0° with respect to the light polarization and fitted with a doublet of PCI-deformed peaks including vibrational progression. (c) Spectral ratio between normal N_2 and isotope substituted $^{14,15}N_2$ (purple) respectively $^{15,15}N_2$ (green) for the photoelectron intensity at the quasi-magic angle and (d) at 0° to the light polarization with more rebinning than in fig. 6.2. The solid lines are again the model calculations which include the vibrational effect and, for $^{14,15}N_2$, also the effect of the symmetry breaking (shaded areas). For $^{14,15}N_2$, the (mostly hidden) dashed lines show a modeling of the vibrational effect only.

end of the N_2:N(1s) photo line. The details of this simulation are shown in fig. 6.6 and are explained in section 6.3.

The cross section and angular distribution effect can be attributed to the *broken inversion symmetry* in the singly substituted species, as derived in a more quantitative way in section 6.4. While the inversion symmetry of N_2 is maintained in the doubly substituted species $^{15,15}N_2$, the electron wave function in $^{14,15}N_2$ is slightly modified due to the broken symmetry of the singly substituted molecule, where the center of symmetry of the electric charges, situated in the geometrical center of the molecule, no longer coincides with the shifted center of mass (see figure 6.7).[263,264] The modified wave functions in the molecule with broken inversion symmetry lose their character as parity eigenfunctions and can be described by a *linear combination* of the original gerade and ungerade wave functions. At the energy considered here, right on top of the shape resonance, the cross section and angular distribution of gerade and ungerade are maximally different (see fig. 5.8). Thus, already a small intermixture leads to noticeable changes, namely an increase of the ungerade and a decrease of the gerade cross section combined with a decrease of the ungerade and an increase of the gerade β-parameter. As described in more detail in the following, a change of σ by 1.5% and β by roughly 5% is able to qualitatively and quantitatively explain the additional wiggle of the ratio in the region of the ν=0 components.

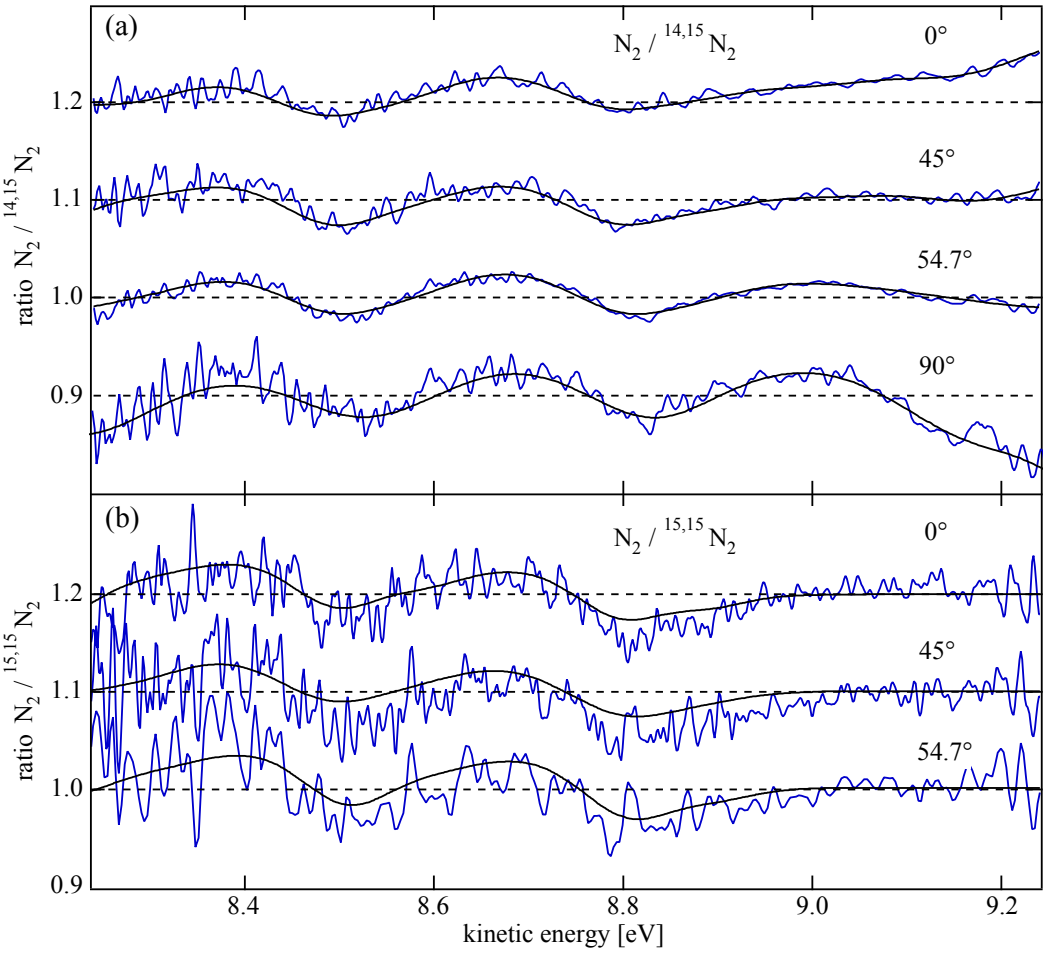

Figure 6.4: Ratios of regular and singly (a) respectively regular and doubly isotope substituted nitrogen (b) for different electron emission angles showing the angular dependence of the symmetry-induced isotope effect (for better visibility, the curves for the different angles are plotted with a vertical offset). The blue curves are the ratios of the measured spectra while the black curves are the ratios of the corresponding fit curves.

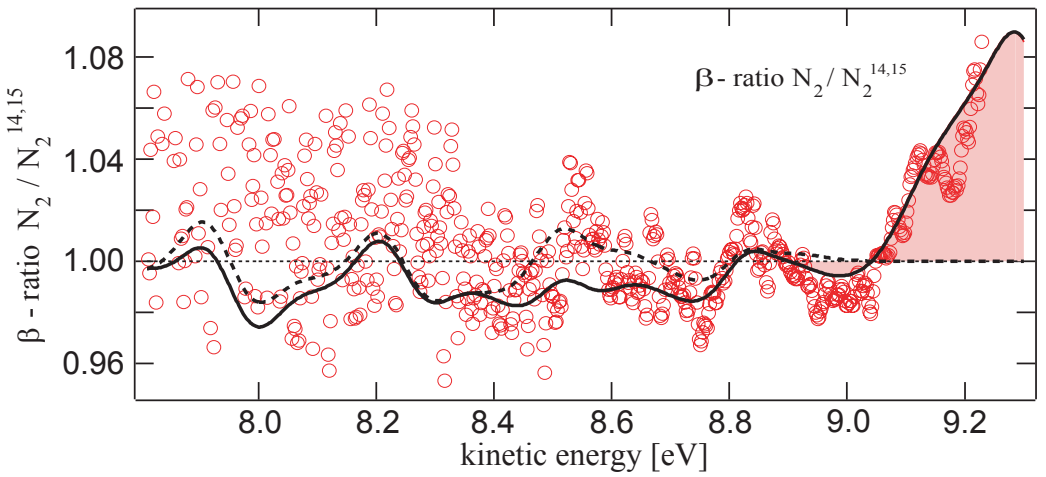

Figure 6.5: Ratio between normal N_2 and isotope substituted $^{14,15}N_2$ for the photoelectron angular distribution parameter β in the range of the N_2:N(1s) photo line together with model calculations of the symmetry effect (solid) and those including the vibrational effect only (dashed). The shaded areas highlight the changes which cannot be explained by a simple shift, but only by a change in the β-parameters of the g and u components as simulated by the solid black line.

While a wiggle in the v=0 region could, in principle, also be due to a shift in the binding energy or a change of the gerade-ungerade splitting, such changes are neither supported by the experimental observation nor would they explain the pronounced *angular dependency* observed in the experiment, which is demonstrated in the ratios at the different electron emission angles (fig. 6.4(a)) as well as in the ratio of the spectral β-parameter (fig. 6.5). Other than the suggested symmetry effect, only a shift of the shape resonance position, e.g. due to a change of the bond length in the isotope substituted molecule, would cause both an angular as well as cross section effect. However, a change of the bond length, e.g. due to the increased rotational inertia, should be even more pronounced in the doubly-substituted molecule, where the effect in question does not appear at all (see fig. 6.4(b)).

6.3 Franck-Condon Analysis

In order to determine the size of the symmetry effect and to disentangle it from the pure mass effects, the change of the Franck-Condon factors due to the isotope substitution need to be analyzed quantitatively. As mentioned in section 6.1, the offset between the potential curves of the ground and excited state increases in the heavier (substituted) molecule due to the higher reduced mass.[c] Higher vibrational excitations consequently become stronger compared to the non-substituted case while the v=0 loses some intensity.[253] In order to estimate the size of this effect, a Franck-Condon analysis of the measured $^{14,14}N_2$ spectra was performed, from which a quantitative description of the complete Morse potential can be derived.[266] The knowledge of this potential allows to calculate the mass-induced changes on the Frank-Condon factors upon isotope substitution. For the v=0 components, a 0.2% respectively 0.4% decrease of the ungerade component and a 0.7% respectively 1.5% decrease of the gerade component was calculated for $^{14,15}N_2$ respectively $^{15,15}N_2$. In turn, a 1.5% respectively 3.0% increase of the ungerade and a 1.0% respectively 2.0% increase of the gerade v=1 is predicted. This is in very good agreement with the experimentally observed changes of the Franck-Condon factors, which can be estimated empirically by comparing the simulation curves in fig. 6.6 to the experimental ratios (see below). It also shows that the change of the Franck-Condon factors does affect the v=0 components considerably, but does not account entirely for the observed intensity changes of 2% for the gerade and 1.4% for the ungerade v=0 component. The Franck-Condon effect by itself is therefore not sufficient to fully explain the observed isotope effect, and an influence of the symmetry breaking, which is motivated further in the following section, can indeed be identified as the only remaining, plausible explanation. However, the Franck-Condon analysis reveals that out of the total effect, only $\approx$ 1% is due to the symmetry breaking while the rest is due to change of the Franck-Condon factors.

[c] The offset is expressed in the normal coordinate $Q = \sqrt{\mu}R$ and therefore scales with the square root of the reduced mass μ.

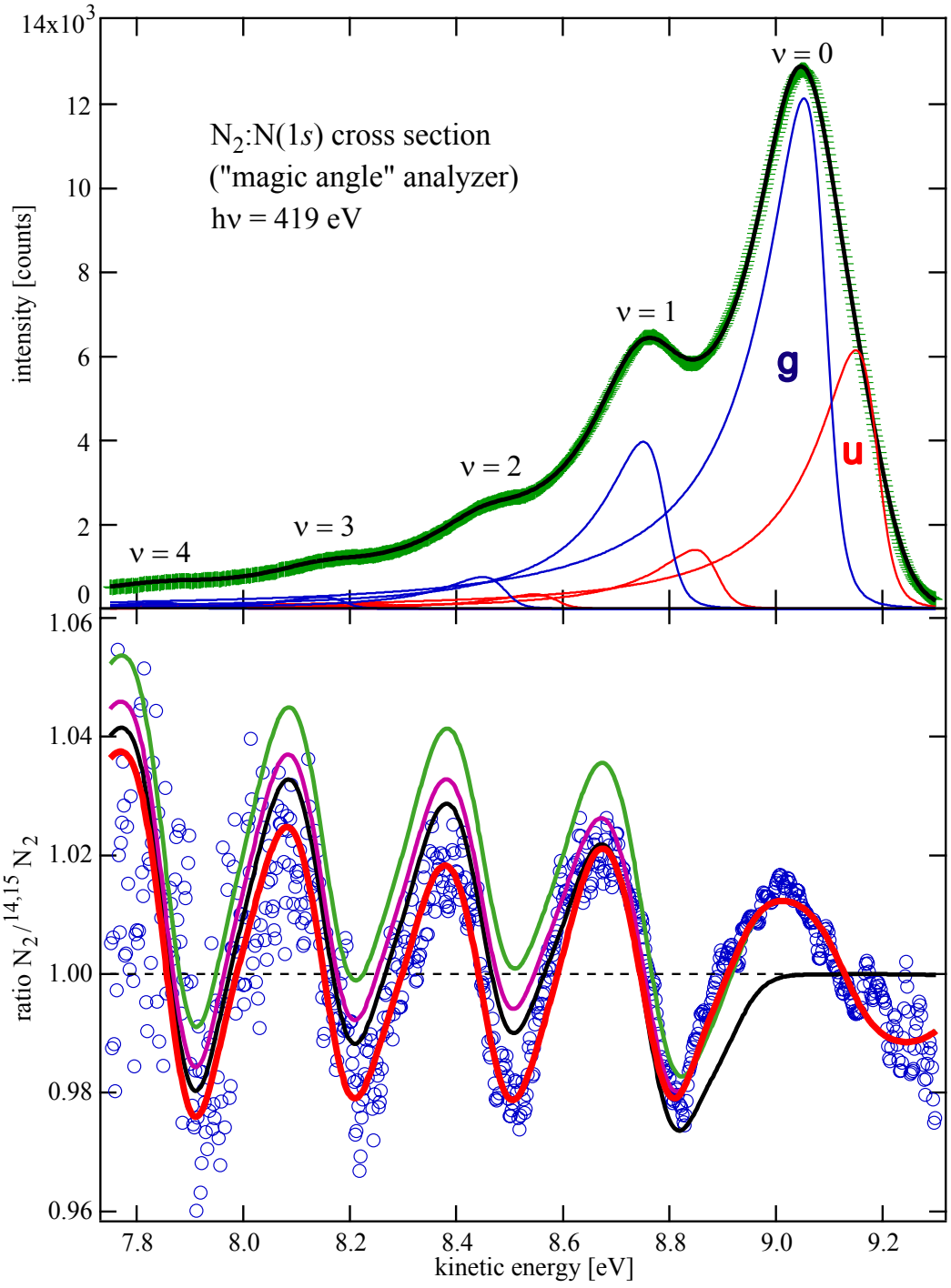

Figure 6.6: Model calculation of the effects of isotope substitution on the N_2:N(1*s*) photo line. Black line: effect of the smaller vibrational energy only (the vibrational components are shifted by 4.5 meV, 9 meV, 13.5 meV and 18 meV); purple line: change of the vibrational energy plus cross-section effect on the v=0 only (empirical fit: g reduced by 2%, u increased by 1.4%); green line: vibrational effect plus identical cross-section change on all v's; red line: vibrational effect plus cross-section change *including* a change of the Franck-Condon factors (empirical fit: v=0 as before, gerade v=1 increased by 1%, gerade v=2 by 2.5%, and gerade v=3 by 2%; ungerade v=1 decreased by 1%, ungerade v=2 increased by 1%, and ungerade v=3 increased by 4%).

The changes of the Franck-Condon factors can also be estimated directly from the measured cross-section ratios with the help of the empirical model calculations, which are shown in detail in fig. 6.6, broken down into the different contributions. The black line is the effect of the smaller vibrational energy as explained in section 6.1. The purple line, which is covered by the red line at the high energy end, includes the cross section effect on the v = 0 component, namely a decrease of the gerade intensity by 2% and an increase of the ungerade intensity by 1.4%, chosen such that the extra wiggle is simulated correctly. Both the frequency and the amplitude of the oscillation, including the extra wiggle, are reproduced perfectly, but line drifts too far up for lower kinetic energies. The reason is that already by shifting the vibrational components towards higher energy, the low energy tail of the photo line in the substituted case decreases and the ratio therefore increases. Reducing the intensity of the gerade component emphasizes the upward trend of the ratio since it also reduces the strong gerade contribution to the tail at low energies. Simulating the 2% respectively 1.4% change of intensity for all v-components (green line) reinforces the trend even more. However, an increase of the higher vibrational components due to an increase of the Franck-Condon factors in the isotope substituted molecule compensates the upward trend. A simulation with increased Franck-Condon factors to match the data is shown by the red curve. From this empirical fit of the ratio, the change of the Franck-Condon factors can be estimated. In order to match the experimental ratio, the gerade v=1 component has to be increased by 1% compared to regular nitrogen. According to the least-square fit of the photo line shown in the top panel of fig. 6.6, the gerade v=1 has 33% of the intensity of the gerade v=0, so 1% intensity gain in the v=1 corresponds to 0.33% intensity loss in the v=0. However, taking into account that the symmetry breaking should have actually lowered the intensity of the gerade v=1 by about 1%, the intensity gain of the v=1 due to the Franck-Condon effect has to be in the order of 2% and the loss of the v=0 roughly 0.66%.[d] These numbers are consistent with the predictions based on the proper Franck-Condon analysis described above.

6.4 Symmetry Breaking via Asymmetric Vibrational Motion

Having established a strong empirical link between the symmetry breaking and the observed isotope effect on the electronic wave function in the previous sections, two questions arise: How can one understand the size of the observed effect, and why has it not been seen in any photoelectron spectrum of a diatomic homonuclear molecule so far? Both questions are closely related and require a consideration of the energy scales of the unperturbed system and its perturbation. Applying first order perturbation theory, the modified wave

[d] The intensity changes of the v>1 can be neglected for a first approximation since their total intensity is less than 10% of the v=0 component and their total intensity change therefore makes up less than 0.1% of the v=0 intensity. However, the percentages of the changes are marked in the plot.

functions $\hat{\psi}_g$ and $\hat{\psi}_g$ in the symmetry-broken system can be expressed as

$$\hat{\psi}_g \;=\; \psi_g \;+\; \frac{\Delta E_{asym}}{\Delta E_{g/u}}\;\psi_u \tag{6.1}$$

respectively

$$\hat{\psi}_u \;=\; \psi_u \;+\; \frac{\Delta E_{asym}}{\Delta E_{g/u}}\;\psi_g\;. \tag{6.2}$$

where ψ_g and ψ_u are the wave functions of the unperturbed system, $\Delta E_{asym} = <\psi_g|H_{asym}|\psi_u>$ is the *asymmetry energy*, and $\Delta E_{g/u}$ is the energy difference between the $1\sigma_g$ and $1\sigma_u$ states.[267 e]

Considering all energy effects caused by isotope substitution, only the energy of the asymmetric vibrational motion due to the shifted center of mass is of non-negligible size. All other effects, in particular hyperfine perturbations, which cause g/u symmetry breaking in highly excited states,[254, 262] and isotope shifts, which induce predissociation in isotopomers,[263–265] are in the μeV range.

In order to estimate the size of the asymmetry energy ΔE_{asym}, the shift of the center of mass has to be considered. If the origin of the coordinate system is placed at the geometrical center of the molecule, the center of mass of the singly-substituted molecule is given by

$$\frac{14\,r+15\,r}{14+15} \;=\; \frac{r}{29} \;\approx\; 0.034r\;, \tag{6.3}$$

where r is the distance of the two nuclei from the geometrical center. In other words, the center of mass of the isotope substituted molecule is shifted by 3.4% away from the symmetry center of the Coulomb potential of the molecule, resulting in an *asymmetric vibrational motion* of the nuclei with respect to the symmetry center of the potential. This asymmetric motion leads to an asymmetric contribution to the total vibrational energy in the order of 3% of 300 meV, i.e. 10 meV. Therefore, according to eq. (6.1) and (6.2), the modified wave functions in the isotope substituted molecule have a 10% contribution of the wave function of opposite parity (see fig. 6.7).[f]

In order to obtain the resulting relative change of the intensities, the square of the mixing coefficient $\frac{\Delta E_{asym}}{\Delta E_{g/u}}$ has to be multiplied by the normalized intensity difference of the gerade and ungerade channels $\frac{I_g - I_u}{I_g + I_u}$ at the given energy. At the considered photon energy, this results in an estimated relative change of the cross section in the order of 1%, which is consistent with the size of the experimentally observed cross-section effect determined in section 6.3.[g] The breaking of the inversion symmetry is thus coupled to the electronic

[e] The associated energies can also be called *nondiagonal* and *diagonal* energies, referring to the respective contributions to total Hamiltonian, which appear as off-diagonal respectively diagonal elements when the origin of coordinates is chosen at equal distance from the two nuclei rather than at the center of mass.[264]

[f] This is also true for the vibrational ground state $v = 0$ which is equally affected by the asymmetric vibrational motion due to the vibrational ground state motion ("zero-point vibration") (see Appendix C).

[g] The angle-dependent, i.e. β-effect is enlarged due to the role of the phase shift between the partial photoelectron waves coming into play for all other emission directions besides the magic angle.

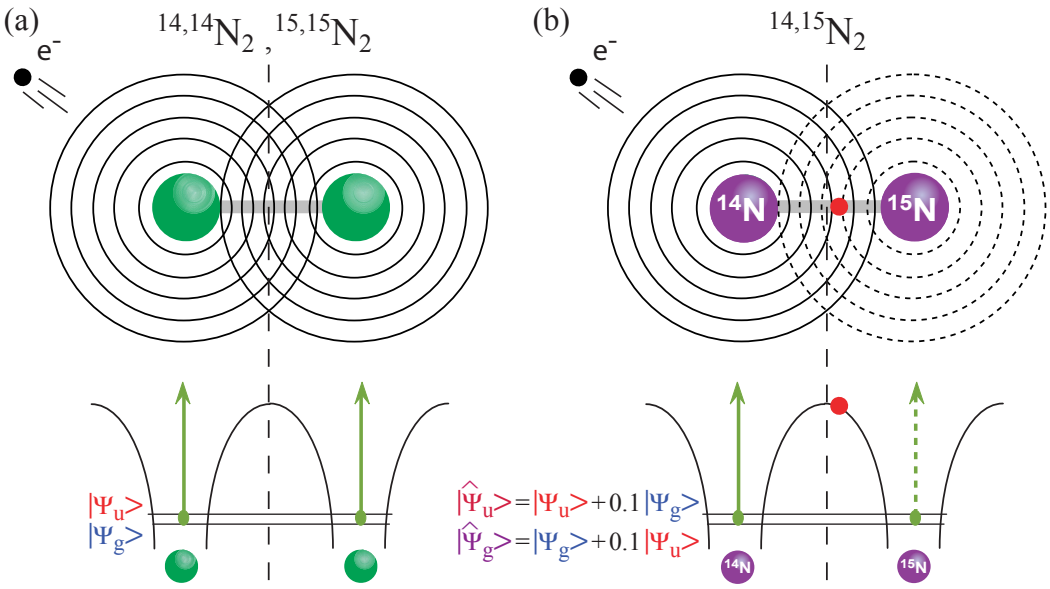

Figure 6.7: (a) $^{14}N_2$ respectively $^{15}N_2$: Coherent and delocalized electron emission from two indistinguishable molecular centers into gerade and ungerade final states. (b) $^{14,15}N_2$: Partial core hole localization due to symmetry breaking - mixing between gerade and ungerade final states.

wave function via an asymmetric vibration with respect to the geometric midpoint between the two nuclei. In this sense, the observed effect can be seen as the diatomic analog to symmetry breaking via vibronic coupling in triatomic molecules,[270] and as the inverse effect of symmetry restoration by detuned excitation observed in resonant inelastic x-ray scattering.[268]

The above energy consideration also explains why an isotope induced symmetry-breaking effect has never been observed in valence photoionization, where the gerade-ungerade splitting is in the range of several electron volts due to the strong delocalization of most valence electrons, and the *fractional size* $\frac{\Delta E_{asym}}{\Delta E_{g/u}}$ of the symmetry breaking is more than an order of magnitude smaller than for the core level. Such small absolute changes of less than one per thousand are inaccessible to present day photoelectron spectroscopy. In particular, the valence effect would have to be measured on an absolute scale rather than on a relative scale as in the present measurement, because there are no close-lying gerade and ungerade lines showing effects in opposite directions.

For core levels of other molecules, the effect is not observable either since the gerade-ungerade splitting is too *small*. In a system of identical but non-overlapping, i.e. completely localized, core orbitals, the gerade and ungerade states are degenerate, and their symmetry-specific character is inaccessible to experimental exploration by photoelectron spectroscopy because the incoherent sum of gerade and ungerade states and left and right hand states are, by definition, identical (see chapter 5.2). A small overlap between the two core orbitals and hence a minimal delocalization are required for the two symmetry-adapted states to become non-degenerate with a separation in the order of the natural line width due to the lifetime broadening. While this is just the case for N_2:N(1*s*) photoe-

mission, other core level photoelectron spectra of diatomic homonuclear molecules do not fulfill this requirement,[47,48] and possible symmetry effects are hidden by the (near-) degeneracy.

Further insight can be obtained when interpreting the energy separation between the gerade and ungerade core state in the *core hole hopping* picture, i.e. as the *tunneling rate* of the hopping core hole.[219] In nitrogen, the size of the overlap corresponds to roughly 1% probability of the electrons from one site at the other atomic site, mainly mediated by a core-to-valence coupling.[47,48] The tunneling and the resulting size of the g/u-splitting *stabilizes* the non-local, coherent character of the electronic state against asymmetric left/right distortions such as a shifted center of mass, similar to the role of tunneling versus correlation energy in a superfluidity to Mott insulator transition for instance.[269]

In summary, it was shown that the non-local and coherent behavior of the electron emission and the remaining core hole in a homonuclear molecule is neither conserved nor completely destroyed by a distinct symmetry distortion such as isotope substitution; instead, it changes in a continuous way into partially localized behavior due to the gradual inversion symmetry breakdown, reflected by the parity mixing of the outgoing photoelectron waves. The modified wave functions lose their purity as parity eigenstates, resulting in a change of their relative cross sections and photoelectron angular distribution by several percent. This isotope effect on the electronic structure of a diatomic molecule, probed here by photoelectron spectroscopy, is the first experimentally observed effect of its kind. It demonstrates the onset of the transition from non-local to local behavior, corresponding to the origin of the decoherence process in macroscopic two-slit experiments.[4]

Chapter 7

Conclusion

Coherence, interference, and scattering phenomena play an essential part in molecular photoionization, as was shown for the showcase molecules CO and N_2. Their study reveals the conceptual difference between the photoionization of hetero- and homonuclear molecules and the role played by quantum mechanical non-locality and indistinguishability.

In the heteronuclear CO molecule, the scattering of the carbon core photoelectron on the neighboring oxygen atom leads to photoelectron diffraction which contains information about the geometrical structure of the molecule. Two distinct scattering channels, *forward* and *backward* scattering, exist, reflecting the clear distinguishability of the localized carbon and oxygen core levels.

The complementary case of two indistinguishable and non-local core levels is realized in a homonuclear molecule such as N_2. Photoelectron waves are emitted coherently from both molecular centers, giving rise to characteristic interference-like patterns in the molecule frame photoelectron angular distributions of the nitrogen $1\sigma_g$ and $1\sigma_u$ core hole states. They represent a direct evidence of the quantum mechanical *non-locality* of the remaining core hole in the molecule and suggest that the photoelectron emission from such a molecule can be interpreted as a two-slit experiment. The coherent electron emission with a well defined phase determined by the non-local initial state in a homonuclear molecule replaces the forward-backward scattering character of the electron emission in the heteronuclear CO.

The intermediate regime, i.e. the transition from non-localization to localization, coherence to incoherence, and gerade-ungerade symmetry to forward-backward asymmetry, is probed for the first time in the study of isotope substituted nitrogen. Isotope substitution leads to partial decoherence associated with a partial localization of the core hole, *if* the substitution breaks the inversion symmetry of the molecule. The partial localization should also be reflected in a subtle change of the molecule frame interference pattern from the strictly symmetric gerade-ungerade towards the asymmetric forward-backward case, which would be an interesting effect and a further confirmation to be tested in a future

experiment.

More importantly though, the continuous nature of the transition from coherence to incoherence suggests that it is possible to control the character of a macroscopic quantum state as being either local or non-local by applying distinct forces which either stabilize or destabilize the non-locality. While such a macroscopic quantum phase transition has recently been demonstrated for a Bose-Einstein condensate in an optical lattice,[269] the knowledge gained on molecular systems may build a bridge towards more practical, yet more complex, systems with a greater technical potential, such as double quantum dots which are envisaged as storage elements for quantum information and as future building blocks of quantum gates.[272–275]

With the advent of free electron lasers (FEL),[276–280] which will allow time-resolved pump-probe experiments in the VUV region, new experiments will become feasible that can probe the transition from complete localization of the electrons at individual atomic sites to complete non-localization at identical sites and vice versa, a decoherence process similar to the situation in single-particle interference experiments with macroscopic par-

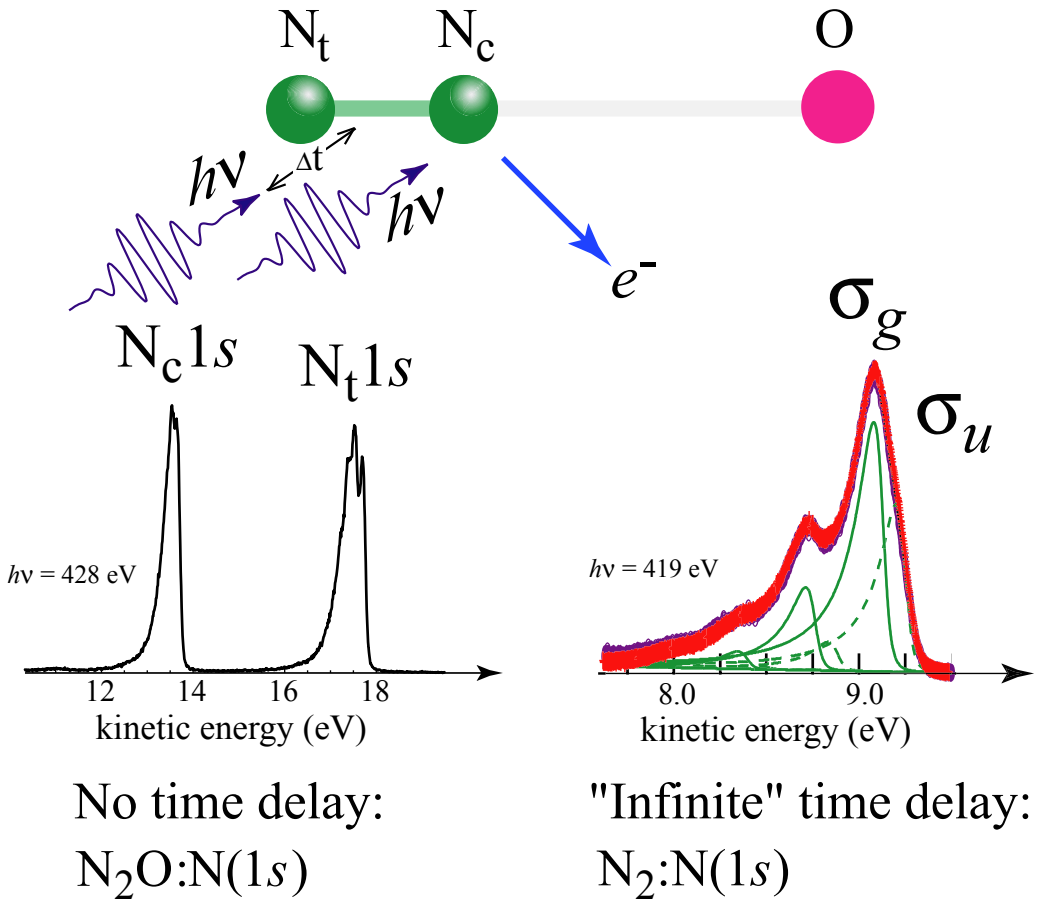

Figure 7.1: Schematics of a time-resolved core-level pump-probe experiment on N_2O probing the continuous transition from localization to non-localization and coherence. An initial light pulse from a VUV free electron laser (FEL) breaks the N_2O molecule into an oxygen and a N_2 fragment. The latter is then probed for various time delays as the oxygen moves further and further away and the system evolves from the distinguishable case of N_2O (left) towards the non-local, indistinguishable case of N_2 (right).

ticles.[4] For that purpose, one could envision an experiment where a nitrous oxide (N_2O) molecule is broken into an oxygen and a N_2 fragment by an initial light pulse and the core photoionization of the N_2 fragment is then probed for various time delays as the oxygen moves further and further away (see fig.7.1). With increasing distance, the emission characteristics should change from the localized case of N_2O, where the two nitrogen atoms are distinguishable due to the chemical shift induced by the oxygen, to the non-local, indistinguishable case of N_2.

In order to observe the full transition, a time resolution of a few hundred femtoseconds together with an energy resolution of the probe pulse of 100 meV or better is necessary. While a certain trade-off between time and energy resolution cannot be avoided, both requirements are within the specifications of the high-resolution beamline at the proposed BESSY VUV-FEL.[280] The suggested experiment may therefore be feasible within the next few years.

In summary, this work has demonstrated that the experimental techniques for studying the photoelectron angular distribution of fixed-in-space molecules have moved beyond mere proofs of principle and feasibility and are now developing into a reliable tool for qualitative and quantitative studies of the molecular photoionization process, allowing detailed insights into the electronic structure and the dynamics of the photoionization process that were inaccessible to previous studies. Together with the high energy resolution that can be achieved with state-of-the-art electron spectrometers and third generation light sources, new types of symmetry-resolved, and soon also time-resolved, measurements are possible. The results of these studies may have implications far beyond the field of atomic and molecular physics and apply to chemistry, solid state and surface physics, quantum optics and even the emerging quantum information technology.

Appendix A

Electronic Setup for Coincidence Measurements

A coincidence measurement requires precise timing and gating of several components in order to reduce electronically created false coincidences and to guarantee an unambiguous and complete recording of true coincidence events. While the function of all main components and the slightly simplified electronic setup is explained in chapter 3.4, the complete setup necessary for the actual experiment is shown in fig. A.1. For purely technical reasons, an additional signal input of so-called "fake ions" created by a 50 Hz pulse generator is required. The reason is that in order to prevent a possible time-stamp mismatch between electron and ion TDC, at least one ion event has to be detected per time stamp overflow, which corresponds to roughly 1-2 Hz for the experiments in the reduced-bunch modes at BESSY or HASYLAB. In order to guarantee this minimum ion detection rate even for very low count rate, the "fake ions" are constantly generated at a rate higher than this minimum rate and added into the signal pathway. Since an ion can only be recorded when the ion cycle is initialized (usually by an electron), the fake ions have to initialize their own ion cycle which is done at the logic OR in front of the ion TDC and position buffer. The delay for the fake ions makes it possible move them to a position in the ion spectrum where no physical ions can appear (e.g. at the very end of the spectrum).

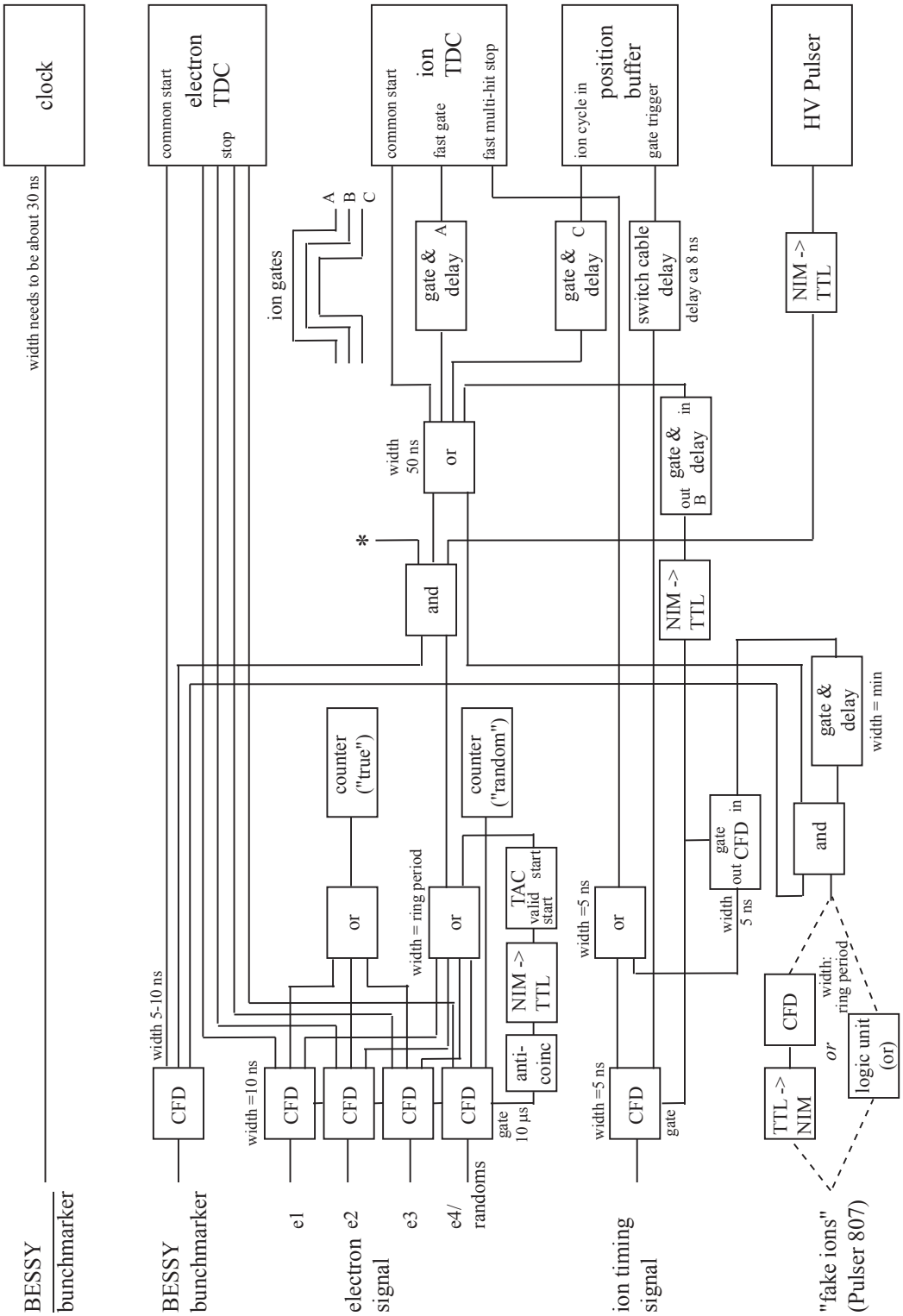

Figure A.1: Schematics of the electronics and signal pathway for photoelectron-photoion coincidence experiments with synchrotron radiation using the ARFMADS and several electron time-of-flight spectrometers.[164]

Appendix B

Multiple Scattering in Non-Spherical Potentials (MSNSP)

The multiple scattering (MS) formalism provides a very "natural" way of describing electron scattering and diffraction processes and is thus widely used in condensed matter and surface physics, e.g. to understand and explain photoelectron diffraction (PD),[129,133,136] low-energy electron diffraction (LEED),[281–283] Auger electron diffraction (AED),[284] x-ray-absorption fine structure (XAFS)[285] and related techniques.[a] It is also often used for molecular systems as it allows to transfer many ideas from the atomic photoionization to the study of molecules and provides very illustrative explanations as well as qualitative results for the behavior of the partial photoionization cross section and the photoelectron angular distributions.[62,63,80,157,167,168,172,179,286–293] However, the details of the photoelectron scattering for low kinetic energies ($E < 30\,\mathrm{eV}$) are not adequately represented by standard multiple scattering theory in spherically symmetric *muffin-tin* potentials. Although it provides a correct physical picture of the photoionization process, it requires rough approximations of the scattering potentials and is consequently unable to reproduce accurately the measured photoelectron angular distributions in the region of the shape resonance.

For this reason, a new theoretical approach has been developed based on the multiple scattering of the photoemitted electron in non-spherical space-filling potentials. The Multiple Scattering in Non-Spherical Potentials (MSNSP) method allows to keep the advantages of the multiple scattering picture and to overcome its limitations by including full molecular, non-spherical scattering potentials through nondiagonal scattering matrices.[157,167,171,179,286–289] The scattering formalism is based on the *MS Xα method* developed for bound molecular states by Johnson and Slater[52,197,294,295] and extended to continuum states by Dill, Dehmer and Siegel with their *Continuum Multiple Scattering Model (CMSM)*.[62,63,79,80,290,296–305]

In MSNSP, the molecular ionic potential is split into two touching roughly hemispherical cells in which the full self-consistent potential is present (see fig. B.1). This allows to include regions of space neglected by standard multiple scattering theory, and to avoid the usual spherical symmetrization of the potentials around each atomic scattering center. The inclusion of non-spherical effects has been found to be crucial in the calculation of the photoelectron angular distributions for kinetic energies of the electron lower than approximately 30 eV.[286–288] MSNSP very accurately predicts the photoelectron angular distributions of oriented diatomic molecules like CO and N_2 in the gas-phase.[157,167,179,286,289] This is true even for energies close to the shape resonance, for which the angular distributions are extremely sensitive to the details of the theoretical description. For *very* low electron kinetic energy (roughly < 3 eV), the electron scattering is too sensitive to the potential cutoff at long distances, and MSNSP theory does not provide reliable results.

Fig. B.1 illustrates the difference between the *muffin-tin* multiple scattering methods[298] and the new *Multiple Scattering in Non-Spherical Potentials (MSNSP)*. The muffin-tin multiple scattering uses spherical, non-overlapping cells $V_\alpha(\mathbf{r})$ and treats the potential in the *interstitial* regions V_{III}

[a] For a broader historical overview of the development and application of the multiple scattering formalism, I refer the interested reader to the references mentioned throughout this chapter.

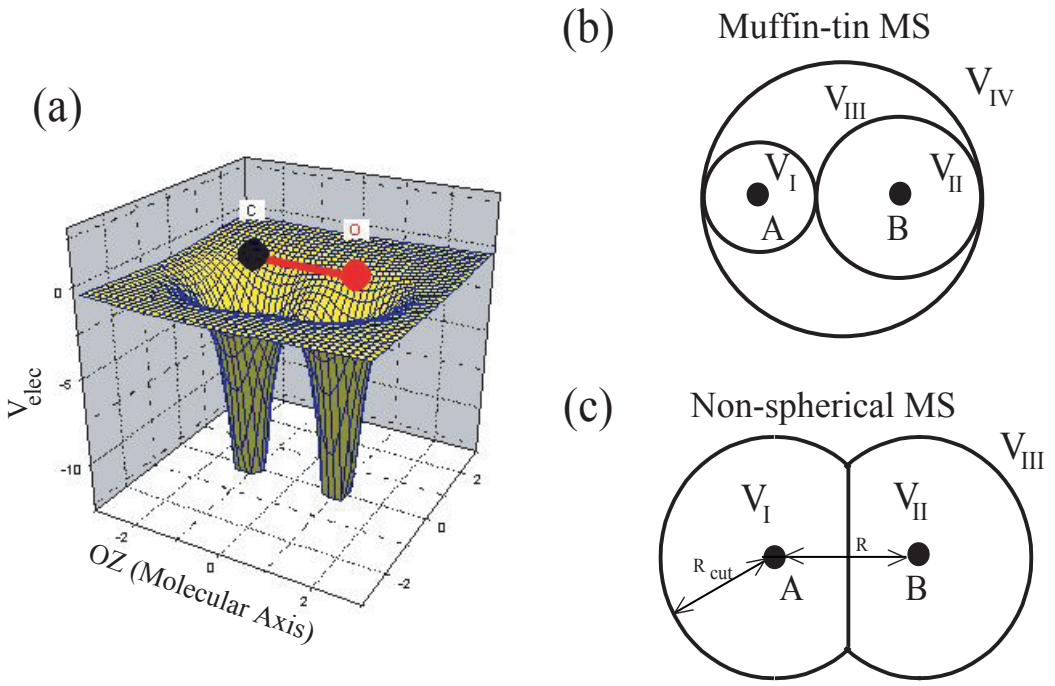

Figure B.1: (a) Electrostatic potential of a CO molecule obtained from the quantum chemistry program *Gaussian 98*.[306] **(b)** Approximation of the scattering potential for *muffin-tin* multiple scattering as applied by Dill *et al.*:[298] region I and II contain the spherically-symmetric atomic potentials of atom A respectively B; region III is constant and region IV is again spherical (for photoionization calculations, it includes mostly the long-range Coulomb potential of the hole). **(c)** Splitting of the total molecular potential $V^{mol}(\mathbf{r})$ for non-spherical multiple scattering (MSNSP) as it is done in this work (see Diplomarbeit and papers): region I and II contain the full molecular potential, region III is considered a pure Coulomb potential.

as constant. However, the spatial variation of the potential in these regions of space is often *not* negligible, especially in the case of photoionization of small systems (like diatomic molecules) where the long range Coulomb potential of the remaining hole is not efficiently screened. One advantage of allowing non-spherical potentials is therefore that one can split $V(\mathbf{r})$ into *space filling* cells and omit the interstitial regions of constant potential (fig. B.1(c)). Furthermore, the scattering potential can be *identical* to the original (e.g. molecular) potential within the cells $V_\alpha(\mathbf{r})$, whereas the necessity of $V_\alpha(\mathbf{r})$ to be spherical in the standard multiple scattering approach only allows to consider the purely atomic part.

In other words, the use of non-spherical potentials allows to improve the description of the intramolecular scattering in two ways:

1. The spatial region in which the potential is well defined is much larger.

2. Molecular effects (i.e. the deviation of the potentials $V_\alpha(\mathbf{r})$ from spherical symmetry due to the molecular bond) are included.

As model calculations have shown, the combination of both effects is crucial in the description of the scattering of low energy photoelectrons.[286]

In the following a brief introduction into multiple scattering is given along with the outline of its application to molecular photoionization. For further details, I refer to the detailed description in my Diplomarbeit.[286]

Consider an electron of energy $E = k^2/2$ described by the wave function $\psi^0(\mathbf{r})$ that satisfies the free-electron Schrödinger equation

$$(\hat{H}_0 - E)\,\psi^0 = 0\,, \tag{B.1}$$

with the Hamilton operator

$$\hat{H}_0 = -\frac{\nabla^2}{2} . \tag{B.2}$$

The presence of a solid or a molecule introduces a strong perturbation that can be represented by the potential

$$V(\mathbf{r}) = \sum_\alpha V_\alpha(\mathbf{r}) , \tag{B.3}$$

where the sum is extended over all atoms α. In order to apply multiple scattering theory, it is important that each potential $V_\alpha(\mathbf{r})$ *vanishes* outside a given region around the atomic position $\mathbf{r}_\alpha$ (see fig. B.1 on the facing page).[b]
The wave function Ψ that satisfies the full Schrödinger equation

$$(\hat{H}_0 + \hat{V} - E)\,\Psi = 0 \tag{B.4}$$

can then be written as

$$\Psi = \psi^0 + \psi^{\text{scat}} , \tag{B.5}$$

where ψ^{scat} is the scattered part. Using operator notation, the latter can be expressed in terms of the *scattering operator* $\hat{T}$ of the full system (also called $\hat{T}$ *matrix*) as

$$\psi^{\text{scat}} = \hat{G}_0 \hat{T} \psi^0 , \tag{B.6}$$

with $\hat{G}_0$ being the *free-electron propagator* (or *free-electron Green operator*) that satisfies $(E - \hat{H}_0)\hat{G}_0 = 1$.
Defining the full system Green operator $\hat{G}$ via $(E - \hat{H}_0 - \hat{V})\hat{G} = 1$, the scattering operator $\hat{T}$ can formally be expressed as $\hat{T} = \hat{V} + \hat{V}\hat{G}\hat{V}$.[c]
The key ingredient of multiple scattering theories is the reduction of the $\hat{T}$ matrix of the full system to the scattering operators $\hat{T}_\alpha$ of the individual potentials $\hat{V}_\alpha$,[307,308] which can be defined by the self-consistent relation

$$\hat{T}_\alpha = \hat{V}_\alpha + \hat{V}_\alpha \hat{T}_\alpha \hat{V}_\alpha . \tag{B.7}$$

$\hat{T}$ can be written as a series expansion whose terms represent all possible electron scattering paths:[307]

$$\hat{T} = \sum_\alpha \hat{\Lambda}_\alpha , \tag{B.8}$$

where $\hat{\Lambda}_\alpha$ accounts for the multiple scattering paths in which the first scattering event occurs at atom α and two consecutive scattering events take place always at different atoms of the system:

$$\hat{\Lambda}_\alpha = \underbrace{\hat{T}_\alpha}_{1^{st}\ order} + \underbrace{\sum_{\beta\neq\alpha} \hat{T}_\beta \hat{G}_0 \hat{T}_\alpha}_{2^{nd}\ order} + \underbrace{\sum_{\gamma\neq\beta} \sum_{\beta\neq\alpha} \hat{T}_\gamma \hat{G}_0 \hat{T}_\beta \hat{G}_0 \hat{T}_\alpha}_{3^{rd}\ order\ scattering} + \underbrace{\ldots}_{higher\ orders} \tag{B.9}$$

From eq. (B.9), $\hat{T}$ can alternatively be defined as

$$\hat{T} = \sum_\alpha (\hat{T}_\alpha + \sum_{\beta\neq\alpha} \hat{\Lambda}_\beta \hat{G}_0 \hat{T}_\alpha) \tag{B.10}$$

$$= \hat{T}_{\alpha_0} + \sum_{\beta\neq\alpha_0} (\hat{\Lambda}_\beta + \hat{\Lambda}_\beta \hat{G}_0 \hat{T}_{\alpha_0}) \tag{B.11}$$

for any atom α_0. Inserting eq. (B.11) into eq. (B.6), the scattered wave ψ^{scat} reduces to

$$\psi^{\text{scat}} = \sum_\alpha (\psi^0_\alpha + \sum_{\beta\neq\alpha} \hat{G}_0 \hat{\Lambda}_\beta \psi^0_\alpha) , \tag{B.12}$$

where

$$\psi^0_\alpha = \hat{G}_0 \hat{T}_\alpha \psi^0 \tag{B.13}$$

[b] In solid state physics, potentials of this type with *non-overlapping spheres* $V_\alpha(\mathbf{r})$ and a constant potential in the interstitial regions are very often used and called "muffin-tin" potentials.
[c] An implicit dependence on E is understood in these expressions.

represents the first-order contribution to the multiple scattering. The second term on the right hand side of eq. (B.12) can be understood as the propagation of the results of scattering at atom α to every other atom β of the system, followed by subsequent multiple scattering starting at the latter.

When applying the multiple scattering method to molecular photoionization, the final state wave function Ψ of the photoelectron is obtained from time-dependent first-order perturbation theory:

$$\Psi = \hat{G}\hat{H}_{rad}\phi_i \,, \tag{B.14}$$

where ϕ_i is the initial state wave function of the electron in the molecule, $\hat{H}_{rad}$ is the incident-light operator and $\hat{G}$ is the Green operator of the full system. $\hat{G}$ can be expressed in terms of the scattering operator of the entire molecule $\hat{T}^{mol}$ by

$$\hat{G} = \hat{G}_0 + \hat{G}_0\hat{T}^{mol}\hat{G}_0 \,, \tag{B.15}$$

where $\hat{G}_0$ is the free-electron Green operator. $\hat{T}^{mol}$ can be calculated from the total molecular potential $\hat{V}^{mol}$ in which the photoelectron moves: The molecular potential in real space $V^{mol}(\mathbf{r})$ is split into different individual potentials $V_\alpha(\mathbf{r})$ (see fig. B.1), from which the scattering operators $\hat{T}_\alpha$ are calculated as explained above. Using eq. (B.11), eq. (B.14) becomes

$$\begin{aligned}\Psi \;=\; & \hat{G}_0\hat{H}_{rad}\phi_i + \hat{G}_0\hat{T}_{\alpha_0}\hat{G}_0\hat{H}_{rad}\phi_i \\ & + \sum_{\beta\neq\alpha_0}\hat{G}_0\hat{\Lambda}_\beta\hat{G}_0\hat{H}_{rad}\phi_i + \sum_{\beta\neq\alpha_0}\hat{G}_0\hat{\Lambda}_\beta\hat{G}_0\hat{T}_{\alpha_0}\hat{G}_0\hat{H}_{rad}\phi_i \,,\end{aligned} \tag{B.16}$$

where α_0 is the atom from which the photoelectron is emitted.

When calculating the photoionization dynamics in the MSNSP approach, one has to be aware that it is a one-electron model and that there can be effects beyond this approach. For instance, *many-body effects* like *interchannel-coupling* (IC) may be important in certain cases and can be particularly strong if there is only a small energy difference between two states, as it is the case in N_2.[90] However, close lying initial states are only a *necessary* condition for this type of coupling, and the actual magnitude of IC effects often varies considerably as a function of the photon energy. While Cherepkov *et al.* pointed out that IC effects are a substantial contribution to the photoelectron dynamics of N_2 at the shape resonance,[90] Hergenhahn *et al.* concluded in their recent measurements that these effects were overestimated in the previous work.[46] This finding is confirmed by the present results shown in chapter 5.3.

Other contributions which might additionally affect the emission process but are disregarded in the present MSNSP calculations are *nondipole effects*.[d] Going beyond the dipole approximation can be particularly important when studying coherence effects in homonuclear molecules, as the approximation of a *small initial state* (*small* compared to the wavelength of the incident light) is not necessarily fulfilled if the initial state is delocalized over two atoms.[77] This would mean in particular that one has to add an additional phase $e^{\,i\mathbf{k}_{ph}\cdot(\mathbf{r}_A-\mathbf{r}_B)}$ to the double slit-like phase shift discussed in section 5.1, where $\mathbf{k}_{ph}$ is the photon momentum[e] and $\mathbf{r}_A$ and $\mathbf{r}_B$ are the positions of the two atoms. Hence, nondipole effects could be non-negligible in quantities that are particularly sensitive, e.g. the ratio between gerade and ungerade amplitudes, especially since they can result in a small deviation from the dipole selection rule. First experimental observations of nondipole effects in the photoelectron angular distribution of randomly oriented as well as fixed-in-space N_2 have been reported recently.[73,78] However, their exact origins remain an interesting question to be answered by theory and future experiments.

[d] While it is possible to include nondipole effects into the MSNSP formalism, the current implementation used for the calculations in this work does *not* include these effects.

[e] Its direction is equal to the light propagation and it has the modulus $h\nu/c$, where c is the speed of light.

Appendix C

Isotope Effects in the Harmonic Oscillator Model

To a first approximation, the nuclear motion of a diatomic molecule can be described by a quantum mechanical harmonic oscillator with a potential energy that depends upon the square of the displacement from the equilibrium distance *R*. The quantized energy levels

$$E_v = \left(v + \frac{1}{2}\right)\hbar\omega \qquad v = 1,2,3,... \tag{C.1}$$

correspond to the vibrationally exited states of the molecule (see chapter 2.2.1). Similarly to the classical harmonic oscillator, the frequency ω is given by

$$\omega = \sqrt{\frac{k}{\mu}}\,, \tag{C.2}$$

where k is the *spring* or *bond force constant* and μ is the reduced mass

$$\mu = \frac{m_1 \cdot m_2}{m_1 + m_2}\,. \tag{C.3}$$

Note that even the $v = 0$ ground state has a non-zero energy leading to the so-called *zero-point vibration*.

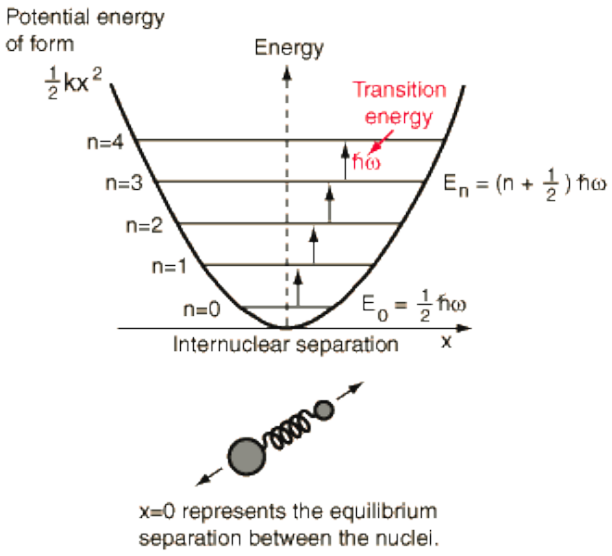

Figure C.1: Quantum mechanical harmonic oscillator

For the case of molecular nitrogen, the harmonic oscillator model is well suited to illustrate the two main effects of isotope substitution, namely a change of the vibrational energy and a total line shift due to the zero-point vibration.

In non-substituted $^{14}N_2$, the vibrational energy $\hbar\omega_{14,14}$ of the core-ionized state is roughly 300 meV (Hergenhahn *et al.*:[46] (295±5) meV , present measurement: (300±2) meV). Replacing one or both of the ^{14}N atoms by a heavier isotope of atomic mass 15 increases the reduced mass μ from $\mu_{14,14} = 7$ to $\mu_{14,15} \approx 7.24$ respectively $\mu_{15,15} = 7.5$, or, in other words, by a factor of 1.034 respectively 1.071. According to eq. (C.2), this leads to a decrease of the frequency ω to

$$\omega_{14,15} = \sqrt{\frac{\mu_{14,14}}{\mu_{14,15}}}\,\omega_{14,14} \quad \text{respectively} \quad \omega_{15,15} = \sqrt{\frac{\mu_{14,14}}{\mu_{15,15}}}\,\omega_{14,14}\,, \tag{C.4}$$

thereby decreasing the vibrational energy to $\bar{h}\omega_{14,15} \approx 295\,\text{meV}$ respectively $\bar{h}\omega_{15,15} \approx 290\,\text{meV}$, a change of 5 meV or 1.7% in the singly substituted and 10 meV or 3.5% in the doubly substituted nitrogen.

In addition to shifting the position of the $v > 0$ vibrational components in the photoelectron spectrum (see chapter 6.1), the smaller vibrational energy also affects the position of the $v = 0$ components due to the associated change of the zero-point vibrational energy $\frac{1}{2}\bar{h}\omega$ of both the neutral molecular ground state as well as the core-ionized state (see fig. C.2). According to Püttner *et al.*,[253] this isotope shift δ can thus be calculated as

$$\delta = \Delta E_{14,15} - \Delta E_{14,14} = \frac{1}{2}[\bar{h}\omega_{14,15} - \bar{h}\omega'_{14,15} - \bar{h}\omega_{14,14} + \bar{h}\omega'_{14,14}] , \qquad \text{(C.5)}$$

where $\bar{h}\omega$ is the vibrational energy of the core-ionized state and $\bar{h}\omega'$ the vibrational energy of the neutral ground state.

Using $\bar{h}\omega'_{14,14} = 292.36\,\text{meV}$ as the vibrational constant of the neutral molecular ground state for non-substituted molecular nitrogen,[309] the respective constant for the isotope substituted molecules can again be calculated according to eq. (C.4), yielding $\bar{h}\omega'_{14,15} = 287.45\,\text{meV}$ and $\bar{h}\omega'_{15,15} = 282.45\,\text{meV}$. While the vibrational energy $\bar{h}\omega$ thus changes by roughly 5 meV respectively 10 meV, and the zero-point vibrational energy $\frac{1}{2}\bar{h}\omega$ changes by roughly 2.5 meV respectively 5 meV upon isotope substitution, the absolute shift of the $v = 0$ line amounts to only

$$\delta_{14,15} \approx \frac{1}{2}\,[290.04\,\text{meV} - 287.45\,\text{meV} - 295\,\text{meV} + 292.36\,\text{meV}] \approx -0.02\,\text{meV} \qquad \text{(C.6)}$$

for the singly substituted, and

$$\delta_{15,15} \approx \frac{1}{2}\,[285.00\,\text{meV} - 282.45\,\text{meV} - 295\,\text{meV} + 292.36\,\text{meV}] \approx -0.04\,\text{meV} \qquad \text{(C.7)}$$

for the doubly substituted nitrogen, which is too small to be detected even in the present high-resolution experiment.

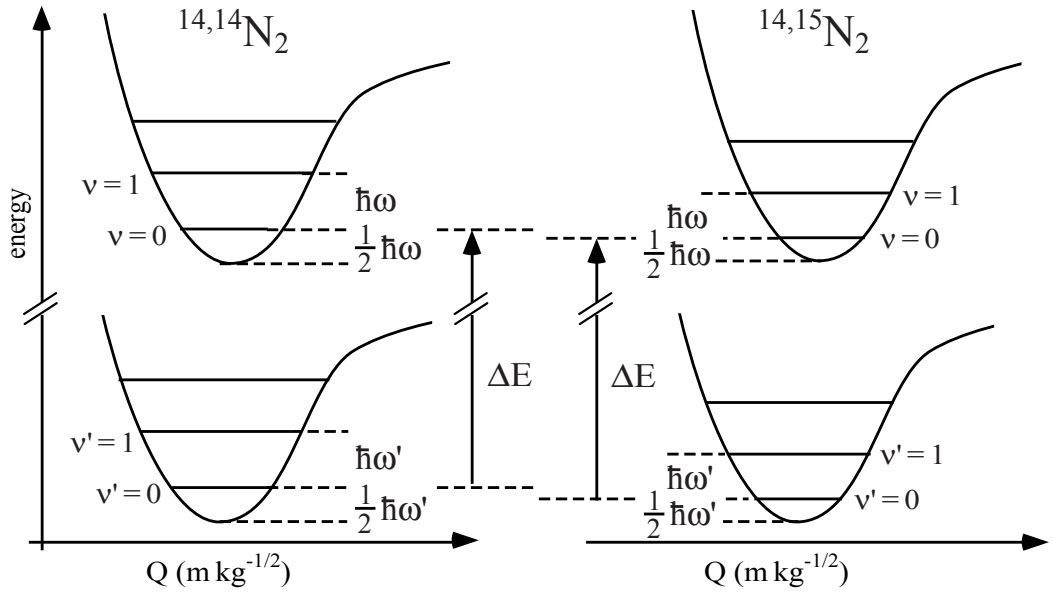

Figure C.2: Schematics of the molecular potential curves for the ground and core-ionized states of $^{14}N_2$ and $^{14,15}N_2$ as a function of the normal coordinate $Q = \sqrt{\mu}R$.[253] The mass-induced change of the vibrational energy as well as the zero-point energy are illustrated schematically.

Appendix D

List of Symbols and Abbreviations

Symbols

a_0	the Bohr radius, $a_0 = 5.29177 \times 10^{-11}$m
A_{lm}	angular expansion coefficients
A^*	(electronically) excited state of atom A
A^+	singly charge ion of atom A
α	fine structure constant, $\alpha = 137.0359895$
β_e	photoelectron angular distribution asymmetry parameter
β_m	molecular alignment parameter
c	(vacuum) speed of light, $c = 2.99792458 \times 10^8 \frac{\mathrm{m}}{\mathrm{s}}$
CO	carbon monoxide
D_e	dissociation energy
e	the elementary charge, $e = 1.60217733 \times 10^{-19}$C
e^-	photo (or Auger) electron
E	kinetic energy of the photoelectron
E_{ion}	ionization energy
$\hat{\boldsymbol{\varepsilon}}$	polarization (unit) vector of the light
ϕ_i	(bound) initial state wave function of the electron in the molecule
Φ_{1s}	atomic 1*s* wave function
$\hat{G}_0$	free-electron propagator (or free-electron Green operator)
h	Planck's constant, $h = 6.6260755 \times 10^{-34}$Js, $\overline{h} = \frac{h}{2\pi} = 1.05457266 \times 10^{-34}$Js
$h\nu$	photon energy
$\hat{H}_0$	free electron Hamilton operator
$\hat{H}_{rad}$	Hamilton operator of the electromagnetic field
i	imaginary unit, $i^2 = -1$
$\mathbf{k}$	momentum vector; $k = \sqrt{2E}$
l	orbital angular momentum quantum number/angular momentum (in atomic units)
λ_e	de–Broglie–wavelength of the electron
$\hat{\Lambda}_\alpha$	multiple scattering paths in which the first scattering event occurs at atom α
m_0	the rest mass of the electron, $m_0 = 9.1093897 \times 10^{-31}$kg
m_l	angular momentum component with respect to quantization axis
μ	reduced mass
N_2	molecular nitrogen
ν	frequency of the electromagnetic radiation *or* vibrational quantum number
Ω	solid angle
$P_l(\cos\theta)$	l^{th}-order Legendre polynomial
Ψ_i	wave function of (a general) initial state
$< \Psi_f \vert \sum_\mu \mathbf{r}_\mu \vert \Psi_i >$	dipole matrix element (in length form)
$\mathbf{r}_\alpha$	position of atom α
R	internuclear distance
S	overlap integral

σ_{if}	partial cross section
$d\sigma_{if}(h\nu)/d\Omega$	differential cross section/angular distribution)
σ_g	molecular σ-orbital with gerade symmetry
σ_u	molecular σ-orbital with ungerade symmetry
θ_e	photoelectron emission angle (measured with respect to the polarization vector of the light $\boldsymbol{\varepsilon}$
θ_m	angle between the molecular axis and the polarization vector of the light $\boldsymbol{\varepsilon}$ (or the photon momentum in the case of circularly polarized light)
$\hat{T}_\alpha$	scattering operator describing the scattering in the potential V_α
T^{mol}	(nondiagonal) scattering matrix of the entire molecule
V_α	potential (cell) around atom α
χ_{PD}^{θ}	normalized photoelectron diffraction measured at the angle θ
$Y_{lm}(\Omega)$	spherical harmonics

Abbreviations

ADC Analogue to Digital Converter

ALS Advanced Light Source

ARFMADS Angular Resolved Fixed Molecule Angular Distribution Spectrometer

ARPEPICO Angle Resolved Photoelectron Photoion Coincidence Spectroscopy

BESSY Berliner Speicherring Gesellschaft für Synchrotronstrahlung

CFD Constant Fraction Discriminator

CMSM Continuum Multiple Scattering Model

COLTRIMS Cold Target Recoil Ion Momentum Spectroscopy

DFT Density Functional Theory

EXAFS Extended X-ray-Absorption Fine Structure

FEL Free Electron Laser

FT Fourier Transformation

HASYLAB Hamburger Synchrotronstrahlungslabor

HF Hartree-Fock

HV High Voltage

IC Interchannel Coupling

KER Kinetic Energy Release

LCAO Linear Combination of Atomic Orbitals

MCA Multichannel Analyzer

MCP Multichannel Plate

MPAD Molecule Frame Photoelectron Angular Distribution

MS Multiple Scattering

MSNSP Multiple Scattering in Non-Spherical Potentials

NEXAFS Near Edge X-ray-Absorption Fine Structure

PD Photoelectron Diffraction

PES Photoelectron Spectroscopy

PGM Plane Grating Monochromator

RPA Random Phase Approximation

RCHF Relaxed Core Hartree-Fock

SCF Self Consistent Field

TAC Time to Amplitude Converter

TDC Time to Digital Converter

TDCS Triply Differential Cross Section

TOF Time-of-Flight

UHV Ultra High Vacuum

VUV Vacuum Ultra Violet (radiation)

Appendix E

List of Publications

D. Rolles, R. Díez Muiño, F.J. García de Abajo, C.S. Fadley, and M.A. Van Hove, *Elastic scattering of low-energy electrons by randomly oriented and aligned molecules: Influence of full non-spherical potentials*, J. Electron Spectrosc. Relat. Phenom. **114-116**, 107 (2001).

R. Díez Muiño, D. Rolles, F.J. García de Abajo, F. Starrost, W. Schattke, C.S. Fadley, and M.A. Van Hove, *Multiple scattering theory for non-spherical potentials: Application to photoelectron angular distributions from oriented diatomic molecules and the study of shape resonances*, J. Electron Spectrosc. Relat. Phenom. **114-116**, 99 (2001).

T. Weber, O. Jagutzki, M. Hattass, A. Staudte, A. Nauert, L. Schmidt, M.H. Prior, A.L. Landers, A. Bräuning-Demian, H. Bräuning, C.L. Cocke, T. Osipov, I. Ali, R. Díez Muiño, D. Rolles, F.J. García de Abajo, C.S. Fadley, M.A. Van Hove, A. Cassimi, H. Schmidt-Böcking, and R. Dörner, *K-shell photoionization of CO and N_2: Is there a link between photoelectron angular distribution and molecular decay dynamics?*, J. Phys. B. **34**, 3669 (2001).

R. Díez Muiño, D. Rolles, F.J. García de Abajo, C.S. Fadley, and M.A. Van Hove, *Angular Distributions of Electrons Photoemitted from Core Levels of Oriented Diatomic Molecules: Multiple Scattering Theory in Non-Spherical Potentials*, J. Phys. B. **35**, L359 (2002).

R. Díez Muiño, D. Rolles, F.J. García de Abajo, C.S. Fadley, and M.A. Van Hove, *Multiple Scattering Theory of Photoelectron Angular Distributions*, Surf. Rev. Lett. **9**, 1213 (2002).

T. Jahnke, Th. Weber, A.L. Landers, A. Knapp, S. Schössler, J. Nickles, S. Kammer O. Jagutzki, L. Schmidt, A. Czasch, T. Osipov, E. Ahrenholz, A.T. Young, R. Díez Muiño, D. Rolles, F.J. García de Abajo, C.S. Fadley, M.A. Van Hove, S.K. Semenov, N.A. Cherepkov, J. Rösch, M.H. Prior, H. Schmidt-Böcking, C.L. Cocke, and R. Dörner, *Circular Dichroism in K-shell Ionization from Fixed-in-Space CO and N_2 Molecules*, Phys. Rev. Lett. **88**, 073002 (2002).

O. Hemmers, R. Guillemin, E.P. Kanter, B. Krässig, D.W. Lindle, S.H. Southworth, R. Wehlitz, J. Baker, A. Hudson, M. Lotrakul, D. Rolles, W.C. Stolte, I.C. Tran, A. Wolska, S.W. Yu, M.Ya. Amusia, K.T. Cheng, L.V. Chernysheva, W.R. Johnson, and S.T. Manson, *Dramatic Nondipole Effects in Low-Energy Photoionization: Experimental and Theoretical Study of Xe 5s*, Phys. Rev. Lett. **91**, 053002 (2003).

G. Prümper, J. Viefhaus, S. Cvejanovic, D. Rolles, O. Geßner, T. Lischke, R. Hentges, C. Wienberg, W. Mahler, U. Becker, B. Langer, T. Prosperi, N. Zema, S. Turchini, B. Zada, F. Senf, *Upper Limits for Stereoselective Photodissociation of Free Amino Acids in the Vacuum Ultraviolet Region and at the C1s-Edge*, Phys. Rev. A **69**, 062717 (2004); Virtual Journal of Biological Physics Research **8** (2004).

J. Viefhaus, S. Cvejanovic, B. Langer, T. Lischke, G. Prümper, D. Rolles, A.V. Golovin, A.N. Grum-Grzhimailo, N.M. Kabachnik, and U. Becker, *Energy and Angular Distributions of Electrons Emitted by Direct Double Auger Decay*, Phys. Rev. Lett. **92**, 083001 (2004).

R. Guillemin, O. Hemmers, D. Rolles, S. W. Yu, A. Wolska, I. Tran, A. Hudson, J. Baker, and D. W. Lindle, *Nearest-Neighbor-Atom Core-Hole Transfer in Isolated Molecules*, Phys. Rev. Lett. **92**, 223002 (2004).

O. Kugeler, G. Prümper, R. Hentges, J. Viefhaus, D. Rolles, U. Becker, S. Marburger, and U. Hergenhahn, *Intramolecular Electron Scattering and Electron Transfer Following Autoionization in Dissociating Molecules*, Phys. Rev. Lett. **93**, 033002 (2004).

O. Hemmers, R. Guillemin, D. Rolles, A. Wolska, D.W. Lindle, K.T. Cheng, W.R. Johnson, H.L. Zhou, and S.T. Manson, *Nondipole Effects in the Photoionization of Xe $4d_{5/2}$ and $4d_{3/2}$: Evidence for Quadrupole Satellites*, Phys. Rev. Lett. **93**, 113001 (2004).

S. Korica, D. Rolles, A. Reinköster, B. Langer, J. Viefhaus, S. Cvejanovic, and U. Becker, *Partial Cross Sections and Angular Distributions of Resonant and Non-Resonant Valence Photoemission of C_{60}*, Phys. Rev. A **71**, 013203 (2005) and Virtual Journal of Nanoscale Science and Technology **11**, Issue 4 (2005).

O. Hemmers, R. Guillemin, A. Wolska, D.W. Lindle, D. Rolles, K.T. Cheng, W.R. Johnson, H.L. Zhou, and S.T. Manson, *Nondipole Effects in Xe 4d Photoionization*, submitted to J. Electron Sprectrosc. Relat. Phenom. (2004).

O. Hemmers, R. Guillemin, D. Rolles, A. Wolska, D.W. Lindle, E.P. Kanter, B. Krässig, S.H. Southworth, R. Wehlitz, P.W. Langhoff, V. McKoy, B. Zimmermann, *Nondipole Effects in Nitrogen Valence Shell Photoionization just above Threshold*, submitted to J. Electron Sprectrosc. Relat. Phenom. (2004).

E. Sokell, A.A. Wills, M. Wiedenhoeft, X. Feng, D. Rolles, and N. Berrah, *An Investigation of Dissociative Resonant Photoionisation in HCl and DCl Using Two-dimensional Photoelectron Spectroscopy*, submitted to J. Phys. B (2005).

D. Rolles, M. Braune, S. Cvejanovic, R. Hentges, S. Korica, B. Langer, T. Lischke, G. Prümper, A. Reinköster, J. Viefhaus, B. Zimmermann, V. McKoy, and U. Becker, *Symmetry Breakdown of Nitrogen Core Electrons by Isotope Substitution*, in preparation.

B. Zimmermann, D. Rolles, O. Geßner, R. Hentges, S. Korica, T. Lischke, G. Prümper, A. Reinköster, J. Viefhaus, M. Polcik, E. Moler, D. Shirley, R. Dörner, V. McKoy, and U. Becker, *Photoelectron Diffraction From Free CO Molecules*, in preparation.

D. Rolles, O. Geßner, R. Hentges, G. Prümper, J. Viefhaus, and U. Becker, *A Multi-TOF Aparatus for High-Resolution Electron-Ion Coincidence Experiments*, in preparation.

O. Hemmers, W. Stolte, R. Guillemin, D. Rolles, and D. Lindle, *First measurement of macroscopic drag currents caused by nondipole photoelectron emission in the VUV*, in preparation.

List of Figures

Bibliography

[1] R.P. Feynman, *Lectures on Physics, Vol. 3*, (Addison Wesley, Reading, Massachusetts, 1965).

[2] M. Arndt, O. Nairz, J. Vos-Andreae, C. Koller, G. van der Zouw, and A. Zeilinger, Nature **401**, 680 (1999).

[3] L. Hackmüller, S. Uttenthaler, K. Hornberger, E. Reiger, B. Brezger, A. Zeilinger, and M. Arndt, Phys. Rev. Lett. **91**, 090408 (2003).

[4] L. Hackmüller, K. Hornberger, B. Brezger, A. Zeilinger, and M. Arndt, Nature. **427**, 711 (2004).

[5] `http://www.wyp2005.org/`.

[6] A. Zeilinger, G. Weihs, T. Jennewein, and M. Aspelmeyer, Nature **433**, 230 (2005).

[7] A. Zeilinger, Nature **408**, 639 (2000).

[8] H. Walther, Phys. Blätter **56**, Nr. 12, 57 (2000).

[9] A. Einstein, Ann. Phys. **17**, 132 (1905).

[10] K. Siegbahn, C. Nordling, A. Fahlman, R. Nordberg, K. Hamrin, J. Hedman, G. Johansson, T. Bergmark, S.-E. Karlsson, I. Lindgren, and B. Lindberg, *ESCA - Atomic, Molecular and Solid State Structure Studied by Means of Electron Spectroscopy*, (Almquist and Wiksells, Uppsala, Sweden, 1967).

[11] K. Siegbahn, C. Nordling, G. Johansson, J. Hedman, P.F. Heden, K. Hamrin, U. Gelius, T. Bergmark, L.O. Werme, R. Manne, and Y. Baer, *ESCA Applied to Free Molecules*, (North-Holland, Amsterdam, 1969).

[12] C. Kunz, in *Synchrotron Radiation*, edited by C. Kunz, (Springer-Verlag, Berlin, 1979).

[13] *Synchrotron Radiation Research*, edited by H. Winnick and S. Doniach, (Plenum Press, New York, 1980).

[14] For a brief overview of the history of synchrotron radiation, see also `http://xdb.lbl.gov/Section2/Sec_2-2.html`.

[15] H. Hertz, Wied. d. Ann. Phys. u. Chem. **31**, 983 (1887).

[16] T.A. Koopmans, Physica **1**, 104 (1934).

[17] J. Berkowitz, *Photoabsorption, Photoionization, and Photoelectron Spectroscopy*, (Academic Press, New York, 1979).

[18] *Electron Spectroscopy: Theory, Techniques and Applications, Vol. 1-5*, edited by C.R. Brundle, A.D. Baker, (Academic Press, London, 1977-1984).

[19] *VUV and Soft X-Ray Photoionization*, edited by U. Becker and D.A. Shirley, (Plenum Press, New York, 1996).

[20] M. Kutzner, in *VUV and Soft X-Ray Photoionization*, edited by U. Becker and D.A. Shirley, (Plenum Press, New York, 1996), p. 47.

[21] J. Viefhaus, L. Avaldi, F. Heiser, R. Hentges, O. Geßner, A. Rüdel, M. Wiedenhöft, K. Wieliczek, and U. Becker, J. Phys. B **29**, L729 (1996).

[22] J. Viefhaus, *Emissionsrichtungskorrelationen bei der Untersuchung von Mehrelektronenprozessen*, (Verlag Oberhofer, Berlin, 1997).

[23] I. Nenner and P. Morin, in *VUV and Soft X-Ray Photoionization*, edited by U. Becker and D.A. Shirley, (Plenum Press, New York, 1996), p. 291.

[24] P. Auger, J. Phys. Radium **6**, 205 (1925).

[25] H. Aksela, S. Aksela, and N. Kabachnik, in *VUV and Soft X-Ray Photoionization*, edited by U. Becker and D.A. Shirley, (Plenum Press, New York, 1996), p. 401.

[26] A. Messiah, *Quantum Mechanics*, (North-Holland, New York, 1966).

[27] T. Mayer-Kuckuk, *Atomphysik, 3. Aufl.*, (Teubner, Stuttgart, 1985).

[28] H. Haken, H.C. Wolf, *Atom- und Quantenphysik, 5. Aufl.*, (Springer Verlag, Berlin, 1993).

[29] R. Hentges, N. Müller, J. Viefhaus, U. Heinzmann and U. Becker, J. Phys. B **37**, L267 (2004).

[30] A. De Fanis, G. Prümper, U. Hergenhahn, M. Oura, M. Kitajima, T. Tanaka, H. Tanaka, S. Fritzsche, N.M. Kabachnik, and K. Ueda, Phys. Rev. A **70**, 040702(R) (2004).

[31] R. Guillemin, E. Shigemasa, K. Le Guen, D. Ceolin, C. Miron, N. Leclercq, P. Morin, and M. Simon, Phys. Rev. Lett. **87**, 203001 (2001).

[32] Th. Weber, M. Weckenbrock, M. Balser, L. Schmidt, O. Jagutzki, W. Arnold, O. Hohn, M. Schöffler, E. Arenholz, T. Young, T. Osipov, L. Foucar, A. De Fanis, R. Díez Muiño, H. Schmidt-Böcking, C.L. Cocke, M.H. Prior, and R. Dörner, Phys. Rev. Lett. **90**, 153003 (2003).

[33] B. Langer, *Zur Energieabhängigkeit von Photoelektronensatelliten*, (AMS Press, New York, 1992).

[34] R. Wehlitz, *Winkelaufgelöste Elektronenspektrometrie von Mehrelektronenprozessen bei der Photoionisation*, (Dissertation, TU Berlin, 1991).

[35] O. Hemmers, *Korrelationseffekte in kleinen Molekülen*, (AMS Press, New York, 1993).

[36] O. Geßner, *Photoelektronenspektroskopie orientierter Moleküle am Beispiel von CO*, (Diplomarbeit, TU Berlin, 1996).

[37] P. Zimmermann, *Einführung in die Atom- und Molekülphysik*, (Akademische Verlags-Gesellschaft, Wiesbaden, 1978).

[38] H. Haken, H.C. Wolf, *Molekülphysik und Quantenchemie, 5. Aufl.*,(Springer Verlag, Berlin, 1994); English edition: *Molecular Physics and Elements of Quantum Chemistry, 2nd edition*,(Springer Verlag, Berlin, 2003).

[39] F. Engelke, *Aufbau der Moleküle*, (Teubner, Stuttgart, 1992).

[40] P.W. Atkins, *Molecular Quantum Mechanics*, (Oxford University Press, Oxford, 1982).

[41] W.L. Jorgensen and L. Salem, *The Organic Chemist's Book of Orbitals*, (Academic Press, New York, 1973).

[42] R.S. Berry, S.A. Rice, J. Ross, *Physical Chemistry*, (Wiley, New York, 1980).

[43] W. Demtröder, *Molekülphysik*, (Oldenbourg, München, 2003).

[44] U. Hergenhahn, J. Phys. B **37**, R89 (2004).

[45] M. Born and R. Oppenheimer, Ann. Phys. **84**, 457 (1927).

[46] U. Hergenhahn, O. Kugeler, A. Rüdel, E. E. Rennie, and A. M. Bradshaw, J. Phys. Chem. A **105**, 5704 (2001).

[47] N. Kosugi, Chem. Phys. **289**, 117 (2003).

[48] N. Kosugi, J. Electron Spectrosc. Relat. Phenom. **137-140**, 335 (2004).

[49] D. Hartree, *The Calculation of Atomic Structures*, (Wiley, New York, 1957).

[50] V. McKoy, T.A. Carlson, and R. Lucchese, J. Phys. Chem. **88**, 3188 (1984).

[51] M.Ya. Amusia, in *VUV and Soft X-Ray Photoionization*, edited by U. Becker and D.A. Shirley, (Plenum Press, New York, 1996), p. 1.

[52] J.C. Slater and K.H. Johnson, Phys. Rev. B **5**, 844 (1972).

[53] D. A. Verner, D. G. Yakovlev, Astron. Astrophys. **109**, 125 (1995).

[54] E. Fermi, Rev. Mod. Phys. **4**, 87 (1932).

[55] U. Becker and D.A. Shirley, in *VUV and Soft X-Ray Photoionization*, edited by U. Becker and D.A. Shirley, (Plenum Press, New York, 1996), p. 135.

[56] T. Hayaishi and P. Zimmermann, in *VUV and Soft X-Ray Photoionization*, edited by U. Becker and D.A. Shirley, (Plenum Press, New York, 1996), p. 465.

[57] M. Domke, C. Xue, A. Puschmann, T. Mandel, E. Hudson, D. A. Shirley, and G. Kaindl, Chem. Phys. Lett. **173**, 122 (1990).

[58] C.T. Chen, Y. Ma, and F. Sette, Phys. Rev. A **40**, 6737 (1989).

[59] E. Shigemasa, K. Ueda, Y. Sato, T. Sasaki, and A. Yagishita, Phys. Rev. A **45**, 2915 (1992).

[60] E. Shigemasa, T. Hayaishi, T. Sasaki, and A. Yagishita, Phys. Rev. A **47**, 1824 (1993).

[61] F. Sette, J. Stöhr, and A.P. Hitchcock, Chem. Phys. Lett. **110**, 517 (1984); J. Chem. Phys. **81**, 4906 (1984).

[62] J.L. Dehmer and D. Dill, Phys. Rev. Lett. **35**, 213 (1975).

[63] J.L. Dehmer, D. Dill, J. Chem. Phys. **65**, 5327 (1976).

[64] F.A. Gianturco, M. Guidotti, and U. Lamanna, J. Chem. Phys. **57**, 840 (1972).

[65] T.N. Rescigno, P.W. Langhoff, Chem. Phys. Lett **51**, 65 (1977).

[66] J.A. Sheehy, T.J. Gil, C.L. Winstead, R.E. Farren, and P.W. Langhoff, J. Chem. Phys. **91**, 1796 (1989).

[67] C.N. Yang, Phys. Rev. **74**, 764 (1948).

[68] J. Cooper and R.N. Zare, J. Chem. Phys. **48**, 942 (1968).

[69] S.K. Semenov, N.A. Cherepkov, A. De Fanis, Y. Tamenori, M. Katajima, H. Tanaka, and K. Ueda, Phys. Rev. A **70**, 052504 (2004).

[70] J.L. Dehmer, D. Dill, Phys. Rev. A **18**, 164 (1978).

[71] D. Dill, J.R. Swanson, S. Wallace, and J. L. Dehmer, Phys. Rev. Lett. **45**, 1393 (1980).

[72] O. Hemmers, R. Guillemin, D.W. Lindle, Rad. Phys. Chem. **70**, 123 (2004).

[73] O. Hemmers, H. Wang, P. Focke, I.A. Sellin, D.W. Lindle, J.C. Arce, J.A. Sheehy, and P.W. Langhoff, Phys. Rev. Lett. **87**, 273003 (2001).

[74] J. W. Cooper, Phys. Rev. A **42**, 6942 (1990); **45**, 3362 (1992); **47**, 1841 (1993).

[75] M. Ya. Amusia, A.S. Baltenkov, L.V. Chernysheva, Z. Felfli, A.Z. Msezane, and J. Nordgren, Phys. Rev. A **65**, 052512 (2001).

[76] O. Hemmers, W. Stolte, R. Guillemin, D. Rolles, and D. Lindle, *to be published*.

[77] J.D. Mills, J.A. Sheehy, T.A. Ferrett, S.H. Southworth, R. Mayer, D.W. Lindle, and P.W. Langhoff, Phys. Rev. Lett. **79**, 383 (1997).

[78] R. Guillemin, O. Hemmers, D.W. Lindle, E. Shigemasa, K. Le Guen, D. Ceolin, C. Miron, N. Leclercq, P. Morin, M. Simon, and P.W. Langhoff, Phys. Rev. Lett. **89**, 033002 (2002).

[79] D. Dill, J. Chem. Phys. **65**, 1130 (1976).

[80] D. Dill, J. Siegel, and J.L. Dehmer, J. Chem. Phys. **65**, 3158 (1976).

[81] J.W. Davenport, Phys. Rev. Lett. **36**, 945 (1976).

[82] E. Shigemasa, J. Adachi, M. Oura, and A. Yagishita, Phys. Rev. Lett. **74**, 359 (1995).

[83] F. Heiser, O. Geßner, J. Viefhaus, K. Wieliczek, R. Hentges, and U. Becker, Phys. Rev. Lett. **79**, 2435 (1997).

[84] N. Watanabe, J. Adachi, K. Soejima, E. Shigemasa, A. Yagishita, N. G. Fominykh, A.A. Pavlychev, Phys. Rev. Lett. **78**, 4910 (1997).

[85] A.A. Pavlychev, N.G. Fominykh, N. Watanabe, K. Soejima, E. Shigemasa, and A. Yagishita Phys. Rev. Lett. **81**, 3623 (1998).

[86] E. Shigemasa, J. Adachi, K. Soejima, N. Watanabe, A. Yagishita, and N. A. Cherepkov, Phys. Rev. Lett. **80**, 1622 (1998).

[87] K. Ito, J. Adachi, Y. Hikosaka, S. Motoki, K. Soejima, A. Yagishita, G. Raseev, and N.A. Cherepkov, Phys. Rev. Lett. **85**, 46 (2000).

[88] N.A. Cherepkov, G. Raseev, J. Adachi, Y. Hikosaka, K. Ito, S. Motoki, M. Sano, K. Soejima, and A. Yagishita, J. Phys. B **33**, 4213 (2000).

[89] S. Motoki, J. Adachi, Y. Hikosaka, K. Ito, M. Sano, K. Soejima, A. Yagishita, G. Raseev, and N. A. Cherepkov, J. Phys. B **33**, 4193 (2000).

[90] N.A. Cherepkov, S.K. Semenov, Y. Hikosaka, K. Ito, S. Motoki, and A. Yagishita, Phys. Rev. Lett. **84**, 250 (2000).

[91] A.Landers, Th. Weber, I. Ali, A. Cassimi, M. Hattass, O. Jagutzki, A. Nauert, T. Osipov, A. Staudte, M. H. Prior, H. Schmidt-Böcking, C. L. Cocke, and R. Dörner, Phys. Rev. Lett. **87**, 013002 (2001).

[92] U. Fano, Rev. Mod. Phys. **29**, 74 (1957).

[93] H. Klar and H. Kleinpoppen, J. Phys. B **15**, 933 (1982).

[94] C. Heckenkamp, F. Schäfers, G. Schönhense, and U. Heinzmann, Z. Phys. D **2**, 257 (1986).

[95] U. Heinzmann and N.A. Cherepkov, in *VUV and Soft X-Ray Photoionization*, edited by U. Becker and D.A. Shirley, (Plenum Press, New York, 1996), p. 521.

[96] B. Bederson, Comment. At. Mol. Phys. **1**, 65 (1969).

[97] U. Heinzmann, J. Phys. B, **13**, 4367 (1980).

[98] J. Kessler, Comment. At. Mol. Phys. **10**, 47 (1981).

[99] N.A. Cherepkov, Adv. At. Mol. Phys. **19**, 395 (1983).

[100] F. Schäfers, C. Heckenkamp, M. Müller, V. Radojevic, and U. Heinzmann, Phys. Rev. A **42**, 2603 (1990).

[101] K.L. Reid, D.J. Leahy, and R.N. Zare, Phys. Rev. Lett. **68**, 3527 (1992).

[102] D.J. Leahy, K.L. Reid, H. Park, and R.N. Zare, J. Chem. Phys. **97**, 4948 (1992).

[103] B. Zimmermann, *Vollständige Experimente in der atomaren und molekularen Photoionisation*, (Wissenschaft und Technik Verlag, Berlin, 2000).

[104] S. Motoki, J. Adachi, K. Ito, K. Ishii, K. Soejima, A. Yagishita, S.K. Semenov, and N.A. Cherepkov, J. Phys. B **35**, 3801 (2002).

[105] M. Lebech, J.C. Houver, A. Lafosse, D. Dowek, C. Alcaraz, L. Nahon, and R.R. Lucchese, J. Chem. Phys. **118**, 9653 (2003).

[106] O. Geßner, Y. Hikosaka, B. Zimmermann, A. Hempelmann, R.R. Lucchese, J.H.D. Eland, P.-M. Guyon, and U. Becker, Phys. Rev. Lett. **88**, 193002 (2002).

[107] F. Heiser, *Winkelaufgelöste Spektroskopie ionischer Fragmente kleiner Moleküle*, (Dissertation, TU Berlin, 1997).

[108] O. Geßner, *Untersuchung der Photoionisationsdynamik räumlich orientierter Moleküle in der Gasphase*, (Wissenschaft und Technik Verlag, Berlin, 2002).

[109] U. Becker, J. Electron Spectrosc. Relat. Phenom. **112**, 47 (2000).

[110] C. Larsson, A. Beutler, O. Björneholm, F. Federmann, U. Hahn, A. Rieck, S. Verbin, T. Möller, Nucl. Instr. Meth., A **337**, 603 (1994).

[111] K.J.S. Sawhney, F. Senf, M. Scheer, F. Schäfers, J. Bahrdt, A. Gaupp, W. Gudat, Nucl. Instr. and Meth. A **390**, 395 (1997).

[112] M.R. Weiss, R. Follath, K.J.S. Sawhney, F. Senf, J. Bahrdt, W. Frentrup, A. Gaupp, S. Sasaki, M. Scheer, H.-C. Mertins, D. Abramsohn, F. Schäfers, W. Kuch, W. Mahler, Nucl. Instr. and Meth. A **467-468**, 449 (2001).

[113] F. Heiser, O. Geßner, U. Hergenhahn, J. Viefhaus, K. Wieliczek, N. Saito, and U. Becker, J. Electron Spectrosc. Relat. Phenom. **79**, 415 (1996).

[114] O. Hemmers, S.B. Whitfield, P. Glans, H. Wang, D.W. Lindle, R. Wehlitz, and I.A. Sellin, Rev. Sci. Instr. **69**, 3809 (1998).

[115] A.V. Golovin, in *Proc. of the 8th All-Union Conf. on VUV Radiation Physics, Vol. 2*, (Irkutsk, USSR, 1989), p. 396; Opt. Spectrosc. (USSR) **71**, 833 (1991).

[116] A.V. Golovin, V.V. Kuznetsov, N.A. Cherepkov, Sov. Tech. Phys. Lett. **16**, 363 (1990); Z. Physik D **24**, 371 (1992).

[117] J.H.D. Eland, F.S. Wort, and R.N. Royds, J. Electron Spectrosc. Relat. Phenom. **41**, 297 (1986).

[118] J.H.D. Eland, A.H. Pearson, Meas. Sci. Technol. **1**, 36 (1990).

[119] S. Hsieh and J.H.D. Eland, J. Chem. Phys. **103**, 1006 (1995).

[120] P. M. Guyon, A.V. Golovin, C.J.K. Quayle, M. Vervloet, M. Richard-Viard, Phys. Rev. Lett. **76**, 600 (1996).

[121] W.C. Wiley and I.H. McLaren, Rev. Sci. Instrum. **26**, 1150 (1955).

[122] See `http://www.gpta.de` for technical details.

[123] R.J. Smith, J. Anderson, and G.J. Lapeyre, Phys. Rev. Lett. **37**, 1081 (1976).

[124] C.L. Allyn, T. Gustafsson, and E.W. Plummer, Chem. Phys. Lett. **47**, 127 (1977).

[125] E.W. Plummer and W. Eberhardt, Adv. Chem. Phys. **49**, 533 (1982).

[126] D. Rieger, R.D. Schnell, W. Steinman, Surf. Sci. **143**, 157 (1984).

[127] C. Westphal, J. Bansmann, M. Getzlaff, and G. Schönhense, Phys. Rev. Lett. **63**, 151 (1989).

[128] C. Westphal, J. Bansmann, M. Getzlaff, G. Schönhense, N. A. Cherepkov, M. Braunstein, V. McKoy, and R.L. Dubs, Surf. Sci. **253**, 205 (1991).

[129] D.P. Woodruff, D. Norman, B.W. Holland, N.V. Smith, H.H. Farewell, and M.M. Traum, Phys. Rev. Lett. **41**, 1130 (1978).

[130] S. Kono, C.S. Fadley, N.F.T. Hall, and Z. Hussain, Phys. Rev. Lett. **41**, 117 (1978).

[131] S. Kono, S.M. Goldberg, N.F.T. Hall, and C.S. Fadley, Phys. Rev. Lett. **41**, 1831 (1978).

[132] C. F. McConville and D. P. Woodruff,K. C. Prince, G. Paolucci, V. Chab, M. Surman and A. M. Bradshaw, Surf. Sci. **166**, 221 (1986).

[133] C. Westphal, A. Kaduwela, C. Fadley, and M. Van Hove, Phys. Rev. B **50**, 6203 (1994).

[134] O. Schaff and A.M Bradshaw, Phys. Bl. **10**, 997 (1996).

[135] T. Gießel, O. Schaff, C.J. Hirschmugl, V. Fernandez. K.-M. Schindler, A. Theobald, S. Bao, R. Lindsay, W. Berndt, A.M. Bradshaw, C. Baddeley, A.F. Lee, R.M. Lambert, D.P. Woodruff, Surface Science **406**, 90 (1998).

[136] R. Lindsay, P. Baumgärtel, R. Terborg, O. Schaff, A.M. Bradshaw, D.P. Woodruff, Surf. Sci. **425**, L401 (1999).

[137] S. H. Xu, M. Keeffe, Y. Yang, C. Chen, M. Yu, G. J. Lapeyre, E. Rotenberg, J. Denlinger, and J. T. Yates, Jr., Phys. Rev. Lett. **84**, 939 (2000).

[138] R. Terborg, M. Polcik, R.L. Toomes, P. Baumgärtel, J.-T. Hoeft, A.M. Bradshaw, D.P. Woodruff, Surface Science **473**, 203 (2001).

[139] A. Liebsch, Phys. Rev. Lett. **32**, 1203 (1974).

[140] A. Liebsch, Phys. Rev. B **13**, 544 (1976).

[141] B. Budau, G. Raseev, Phys. Rev. B **51**, 16993 (1995).

[142] J.H.D. Eland and V. Schmidt, in *VUV and Soft X-Ray Photoionization*, edited by U. Becker and D.A. Shirley, (Plenum Press, New York, 1996), p. 495.

[143] J.H.D. Eland, J. Chem. Phys. **70**, 2926 (1979).

[144] K.G. Low, P.D. Hampton, and I. Powis, Chem. Phys. **100**, 401 (1985).

[145] P.A. Hatherly, J. Adachi, E. Shigemasa, and A. Yagishita, J. Phys. B **28**, 2643 (1995).

[146] E. Shigemasa, J. Adachi, M. Oura, N. Watanabe, K. Soejima, and A. Yagishita, in *Atomic and Molecular Photoionization*, edited by A. Yagishita and T. Sasaki (Universal Academy Press, Tokyo, 1996), p. 69.

[147] R.J. Beuhler, R.B. Bernstein, J. Chem. Phys. **51**, 5305 (1969).

[148] S. Kaesdorf, G. Schönhense, and U. Heinzmann, Phys. Rev. Lett. **54**, 885 (1985).

[149] F. Harren, D.H. Parker, and S. Stolte, Comments At. Mol. Phys. **26**, 109 (1991).

[150] M. Volkmer, Ch. Meier, A. Mihill, M. Fink, and N. Böwering, Phys. Rev. Lett. **68**, 2289 (1992).

[151] O. Björneholm, M. Bässler, A. Ausmees, I. Hjelte, R. Feifel, H. Wang, C. Miron, M.N. Piancastelli, S. Svensson, S.L. Sorensem, F. Gel'mukhanov, and H. Agren, Phys. Rev. Lett. **84**, 2826 (2000).

[152] M. Kitajima, K. Ueda, A. De Fanis, T. Furuta, H. Shindo, H. Tanaka, K. Okada, R. Feifel, S.L. Sorensen, F. GelŠmukhanov, A. Baev, and H. Ågren, Phys. Rev. Lett. **91**, 213003 (2003).

[153] I.V. Litvinyuk, K.F. Lee, P.W. Dooley, D.M. Rayner, D.M. Villeneuve, and P.B. Corkum, Phys. Rev. Lett. **90**, 233003 (2003).

[154] R.N. Zare, J. Chem. Phys. **47**, 204 (1967).

[155] R.N. Zare, Molecular Photochem. **4**, 1 (1972).

[156] R.W. Wood, Q. Zheng, A.K. Edwards, and M.A. Mangan, Rev. Sci. Instrum. **68**, 1382 (1997).

[157] T. Weber, O. Jagutzki, M. Hattass, A. Staudte, A. Nauert, L. Schmidt, M.H. Prior, A.L. Landers, A. Bräuning-Demian, H. Bräuning, C.L. Cocke, T. Osipov, I. Ali, R. Díez Muiño, D. Rolles, F.J. García de Abajo, C.S. Fadley, M.A. Van Hove, A. Cassimi, H. Schmidt-Böcking, and R. Dörner, J. Phys. B. **34**, 3669 (2001).

[158] A.V. Golovin, F. Heiser, C.J.K. Quayle, P. Morin, M. Simon, O. Geßner, P. M. Guyon, and U. Becker, Phys. Rev. Lett. **79**, 4554 (1997).

[159] R. Dörner, V. Mergel, O. Jagutzki, L. Spielberger, J. Ullrich, R. Moshammer, and H. Schmidt-Böcking, Physics Reports **330**, 95 (2000).

[160] O. Kugeler, S. Marburger, and U. Hergenhahn, Rev. Sci. Instrum. **74** 3955 (2003).

[161] O. Kugeler G. Prümper, R. Hentges, J. Viefhaus, D. Rolles, U. Becker, S. Marburger, and U. Hergenhahn, Phys. Rev. Lett. **93**, 033002 (2004).

[162] G. Prümper, Y. Tamenori, A. De Fanis, U. Hergenhahn, M. Kitajima, M. Hoshino, H. Tanaka and K. Ueda, J. Phys. B **38**, 1 (2005).

[163] J. Viefhaus, O. Geßner, H. Haak, R. Hentges, D. Rolles, G. Prümper, U. Becker, B. Langer, O. Kugeler, and U. Hergenhahn, in *The 7th European Conference on Atomic and Molecular Physics*, europhysics conference abstracts **25 B**, 54 (2001).

[164] D. Rolles, O. Geßner, R. Hentges, G. Prümper, J. Viefhaus, and U. Becker, *to be published*.

[165] R. Dörner, H. Bräuning, O. Jagutzki, V. Mergel, M. Achler, R. Moshammer, J. M. Feagin, T. Osipov, A. Bräuning-Demian, L. Spielberger, J.H. McGuire, M.H. Prior, N. Berrah, J.D. Bozek, C.L. Cocke, and H. Schmidt-Böcking, Phys. Rev. Lett. **81**, 5776 (1998).

[166] A. Lafosse, M. Lebech, J. C. Brenot, P. M. Guyon, O. Jagutzki, L. Spielberger, M. Vervloet, J. C. Houver, and D. Dowek, Phys. Rev. Lett. **84**, 5987 (2000).

[167] T. Jahnke, Th. Weber, A.L. Landers, A. Knapp, S. Schössler, J. Nickles, S. Kammer O. Jagutzki, L. Schmidt, A. Czasch, T. Osipov, E. Ahrenholz, A.T. Young, R. Díez Muiño, D. Rolles, F.J. García de Abajo, C.S. Fadley, M.A. Van Hove, S.K. Semenov, N.A. Cherepkov, J. Rösch, M.H. Prior, H. Schmidt-Böcking, C.L. Cocke, and R. Dörner, Phys. Rev. Lett. **88**, 073002 (2002).

[168] P. Downie and I. Powis, Phys. Rev. Lett. **82**, 2864 (1999).

[169] K. Ito, J. Adachi, R. Hall, S. Motoki, E. Shigemasa, K. Soejima, and A. Yagishita, J. Phys. B **33**, 527 (2000).

[170] K. Ito, J. Electron Spectrosc. Relat. Phenom. **114-116**, 15 (2001).

[171] D. Rolles, M. Braune, S. Cvejanovic, R. Hentges, S. Korica, B. Langer, T. Lischke, G. Prümper, A. Reinköster, J. Viefhaus, B. Zimmermann, V. McKoy, and U. Becker, *to be published*.

[172] Y. Hikosaka, J.H.D. Eland, T.M. Watson, and I. Powis, J. Chem. Phys. **115**, 4593 (2001).

[173] T. Weber, A.O. Czasch, O. Jagutzki, A. K. Müller, V. Mergel, A. Kheifets, E. Rotenberg, G. Meigs, M. H. Prior, S. Daveau, A. Landers, C.L. Cocke, T. Osipov, R. Diez Muino, H. Schmidt-Böcking, and R. Doörner, Nature **431**, 437 (2004).

[174] N. Saito, F. Heiser, O. Hemmers, K. Wieliczek, J. Viefhaus, and U. Becker, Phys. Rev. A **54**, 2004 (1996).

[175] J. Adachi, K. Hosaka, S. Furuya, K. Soejima, M. Takahashi, A. Yagishita, S.K. Semenov, N.A. Cherepkov, Phys. Rev. Lett **91**, 163001 (2003)

[176] J. Adachi, K. Hosaka, S. Furuya, K. Soejima, M. Takahashi, A. Yagishita, S.K. Semenov, N.A. Cherepkov, J. Electron Spectrosc. Relat. Phenom. **137-140**, 243 (2004).

[177] N.A. Cherepkov, S.K. Semenov, A.V. Golovin, J. Adachi, A. Yagishita, J. Phys. B. **37**, 4803 (2004).

[178] T. Jahnke, L. Foucar, J. Tietze. R. Wallauer, T. Osipov, E.P. Benis, A. Alnaser, O. Jagutzki, W. Arnold, S. K. Semenov, N.A. Cherepkov, L.Ph.H. Schmidt, A. Czasch, A. Staudte, M. Schöffler, C.L. Cocke, M.H. Prior, H. Schmidt-Böcking, and R. Dörner, Phys. Rev. Lett. **93**, 083002 (2004).

[179] R. Díez Muiño, D. Rolles, F.J. García de Abajo, C.S. Fadley, and M.A. Van Hove, J. Phys. B **35**, L359 (2002).

[180] J.H.D. Eland, E.J. Duerr, Chem. Phys. **229**, 13 (1998).

[181] O. Geßner, F. Heiser, N. A. Cherepkov, B. Zimmermann, and U. Becker, J. Electron Spectrosc. Relat. Phenom. **101-103**, 113 (1999).

[182] J.L. Dehmer, J. Chem. Phys. **56**, 4496 (1972).

[183] D. Dill, S. Wallace, J. Siegel, J.L. Dehmer, Phys. Rev. Lett. **41**, 1230 (1978); *erratum:* D. Dill, S. Wallace, J. Siegel, J.L. Dehmer, Phys. Rev. Lett. **42**, 411 (1978).

[184] C.S. Fadley and S.A.L. Berström, Phys. Lett. A **35**, 375 (1971).

[185] S.D. Kevan, D.H. Rosenblatt, D. Denley, B.-C. Lu, and D.A. Shirley, Phys. Rev. Lett. **41**, 1565 (1978).

[186] P.A. Lee, P.H. Citrin, P. Eisenberger, and B.M. Kincaid, Rev. Mod. Phys. **53**, 769 (1981).

[187] E.A. Stern, in *Chemical Analysis, Vol. 92*, edited by D.C. Koningsberger and R. Prins, (John Wiley & Sons, New York, 1988), p. 3.

[188] J. Stöhr, in *Chemical Analysis, Vol. 92*, edited by D.C. Koningsberger and R. Prins, (John Wiley & Sons, New York, 1988), p. 443.

[189] U. Becker, O. Geßner, and A. Rüdel, J. Electron Spectrosc. Relat. Phenom. **108**, 189 (2000).

[190] A. Rüdel, R. Hentges, U. Becker, H.S. Chakraborty, M.E. Madjet, and J.M. Rost, Phys. Rev. Lett. **89**, 125503 (2002).

[191] S. Korica, D. Rolles, A. Reinköster, B. Langer, J. Viefhaus, S. Cvejanovic, and U. Becker, Phys. Rev. A **71**, 013203 (2005) and Virtual Journal of Nanoscale Science and Technology **11**, Issue 4 (2005).

[192] A.P. Hitchcock, P. Lablanquie, P. Morin, E. Lizon A Lugrin, M. Simon, P. Thiry, and I. Nenner, Phys. Rev. A **37**, 2448 (1988); Phys. Rev. A **39**, 6051 (1989).

[193] W.C. Stolte, D.L. Hansen, M.N. Piancastelli, I. Dominguez Lopez, A. Rizvi, O. Hemmers, H. Wang, A.S. Schlachter, M.S. Lubell, and D.W. Lindle, Phys. Rev. Lett. **86**, 4504 (2001).

[194] R. Dörner, *private communication*.

[195] B. Zimmermann, D. Rolles, O. Geßner, R. Hentges, S. Korica, T. Lischke, G. Prümper, A. Reinköster, J. Viefhaus, M. Polcik, E. Moler, D. Shirley, R. Dörner, V. McKoy, and U. Becker, *to be published*.

[196] B. Zimmermann, K. Wang, V. McKoy, Phys. Rev. A **67**, 042711 (2003).

[197] J.C. Slater, *The Self-Consistent Field for Molecules and Solids: Quantum Theory of Molecules and Solids, Vol. 4*, (McGraw-Hill, New York, 1974).

[198] S.K. Semenov, N.A. Cherepkov, T. Jahnke, and R. Dörner, J. Phys. B: At. Mol. Opt. Phys. **37**, 1331 (2004).

[199] D.L. Lynch and V. McKoy, Phys. Rev. A **30**, 1561 (1984).

[200] R.R. Lucchese, G. Raseev, and V. McKoy, Phys. Rev. A **25**, 2572 (1982).

[201] H.M. Köppe, A.L.D. Kilcoyne, J. Feldhaus, and A.M. Bradshaw, J. Electron Spectrosc. Relat. Phenom. **75**, 97 (1995).

[202] N. Pangher, H.M. Köppe, J. Feldhaus and J. Haase, Phys. Rev. Lett. **71**, 4365 (1993).

[203] A.P. Hitchcock, C.E. Brion, and W.J. Van der Wiel, J. Phys. B **11**, 3245 (1978).

[204] J.L. Dehmer, D. Dill, and S. Wallace, Phys. Rev. Lett. **43**, 1005 (1979).

[205] A.P. Hitchcock, S. Beaulieu, T. Steel, J. Stöhr, and F. Sette, J. Chem. Phys. **80**, 3927 (1984).

[206] J. Stöhr, and R. Jaeger, Phys. Phys. B **26**, 4111 (1982).

[207] J. Stöhr, J.L. Gland, W. Eberhardt, D. Outka, R.J. Madix, F. Sette, R.J. Koestner, and U. Doebler, Phys. Rev. Lett. **51**, 2414 (1983).

[208] J. Stöhr, F. Sette, and A. L. Johnson, Phys. Rev. Lett. **53**, 1684 (1984).

[209] J. Stöhr and D. A. Outka, Phys. Rev. B **36**, 7891 (1987).

[210] M.N. Piancastelli, D.W. Lindle, T.A. Ferrett, and D.A. Shirley, J. Chem. Phys. **86**, 2765 (1987).

[211] A.P. Hitchcock and J. Stöhr, J. Chem. Phys. **87**, 3253 (1987).

[212] M.N. Piancastelli, D.W. Lindle, T.A. Ferrett, and D.A. Shirley, J. Chem. Phys. **87**, 3255 (1987).

[213] B. Kempgens, H.M. Köppe, A. Kivimäki, M. Neeb, K. Maier, U. Hergenhahn, and A.M. Bradshaw, Phys. Rev. Lett. **79**, 35 (1997).

[214] B. Kempgens, H.M. Köppe, A. Kivimäki, M. Neeb, U. Hergenhahn, and A.M. Bradshaw, Surf. Sci. **425**, L376 (1999).

[215] N. Haack, G. Ceballos, H. Wende, K. Baberschke, D. Arvanitis, A. L. Ankudinov, and J. J. Rehr, Phys. Rev. Lett. **84**, 614 (2000).

[216] F. Sette, J. Stöhr, E.B. Kollin, D.J. Dwyer, J.L. Gland, J.L. Robbins, and A.L. Johnson, Phys. Rev. Lett. **54**, 935 (1985).

[217] H. Cohen and U. Fano, Phys. Rev. **150**, 30 (1966).

[218] I.G. Kaplan and A.P. Markin, Sov. Phys. Dokl. **14**, 36 (1969).

[219] J.W. Gadzuk, in *Electronic Structure and Reactivity of Metal Surfaces*, edited by E.G. Derouane and A.A. Lucas, (NATO proceedings, 1976), p. 341.

[220] P.S. Bagus and H.F. Schaefer III, J. Chem. Phys. **56**, 224 (1972).

[221] R. Broer and W.C. Nieuwpoort, J. Mol. Structure (Theochem) 458, 19 (1999).

[222] L.S. Cederbaum, W. Domcke, and J. Schirmer, Phys. Rev. A **57**, 206 (1998).

[223] L.C. Snyder, J. Chem. Phys. **55**, 95 (1971).

[224] A.A. Pavlychev, A.S. Vinogradov, Opt. Spektrosc. **62**, 329 (1987).

[225] A.A. Pavlychev, *private communication*.

[226] C. Solterbeck, W. Schattke, J.-W. Zahlmann-Nowitzki, K.-U. Gawlik, L.Kipp, M. Skibowski, C.S. Fadley, and M.A. Van Hove, Phys. Rev. Lett. **79**, 4681 (1997).

[227] M. Walter and J.S. Briggs, J. Phys. B **32**, 2487 (1999).

[228] N. Stolterfoht, B. Sulik, V. Hoffmann, B. Skogvall, J.Y. Chesnel, J. Rangama, F. Frémont, D. Hennecart, A. Cassimi, X. Husson, A.L. Landers, J.A. Tanis, M.E. Galassi, and R. D. Rivarola, Phys. Rev. Lett **87**, 023201 (2001).

[229] N. Stolterfoht, B. Sulik, B. Skogvall, J.Y. Chesnel, F. Fremont, D. Hennecart, A. Cassimi, L. Adoui, S. Hossain, and J.A. Tanis, Phys. Rev. A **69**, 012701 (2004).

[230] D. Misra, U. Kadhane, Y.P. Singh, L.C. Tribedi, P.D. Fainstein, and P. Richard, Phys. Rev. Lett **92**, 153201 (2004).

[231] L Sarkadi, J. Phys. B **36**, 2153 (2003).

[232] C.R. Stia, O.A. Fojon, P.F. Weck, J. Hanssen, and R.D. Rivarola, J. Phys. B **36**, L257 (2003).

[233] O.A. Fojon, J. Fernandez, A. Palacios, R.D. Rivarola, and F. Martin, J. Phys. B **37**, 3035 (2004).

[234] S.K. Semenov and N.A. Cherepkov, Chem. Phys. Lett. **291**, 375 (1998).

[235] S.K. Semenov, N.A. Cherepkov, G.H. Fecher, and G. Schönhense, Phys. Rev. A **61**, 032704 (2000).

[236] S.K. Semenov and N.A. Cherepkov, Phys. Rev. A **66**, 022708 (2002).

[237] S.K. Semenov and N.A. Cherepkov, J. Phys. B **36**, 1409 (2003).

[238] G. Bandarage and R.R. Lucchese, Phys. Rev. A **47**, 1989 (1993).

[239] R.E. Stratmann, G. Bandarage, and R.R. Lucchese, Phys. Rev. A **51**, 3756 (1995); J. Chem. Phys. **102**, 8493 (1995).

[240] F. Wuilleumier and M.O. Krause, J. Electron Spectrosc. Relat. Phenom. **15**, 15 (1979).

[241] A. Menzel, S.P. Frigo, S.B. Whitfield, C.D. Caldwell, and M.O. Krause, Phys. Rev. A **54**, 2080 (1996).

[242] D.W. Lindle, L.J. Medhurst, T.A. Ferrett, P.A. Heimann, M.N. Piancastelli, S.H. Liu, D.A. Shirley, T.A. Carlson, P.C. Deshmukh, G. Nasreen, and S.T. Manson, Phys. Rev. A **38**, 2371 (1988).

[243] M. Domke, K. Schulz, G. Remmers, G. Kaindl, and D. Witgen, Phys. Rev. A **53**, 1424 (1996).

[244] G.C. King, M. Tronc, F.H. Read, and R.C. Bradford, J. Phys. B **10**, 2479 (1977).

[245] P. Lin and R.R. Lucchese, J. Chem. Phys **117**, 4348 (2002).

[246] M. Stener, G. Fronzoni, P. Decleva, Chem. Phys. Lett. **351**, 469 (2002).

[247] J.E. Pollard, D.J. Trevor, J.E. Reutt, Y.T. Lee, and D.A. Shirley, J. Chem. Phys. **77**, 34 (1982).

[248] T. Baer and P.M. Guyon, J. Chem. Phys. **85** 4765 (1986).

[249] S. Svensson, L. Karlsson, P. Balzer, B. Wannberg, and U. Gellius, J. Chem. Phys. **89**, 7193 (1988).

[250] F. Burmeister, S.L. Sorensen, O. Björneholm, A. Naves de Brito, R.F. Fink, R. Feifel, I. Hjelte, K. Wiesner, A. Giertz, M. Bässler, C. Miron, H. Wang, M.N. Piancastelli, L. Karlsson, and S. Svensson, Phys. Rev. A **65**, 012704 (2001).

[251] L.M. Andersson, F. Burmeister, H.O. Karlsson, and O. Goscinski, Phys. Rev. A **65**, 012705 (2001).

[252] F. Burmeister, L.M. Andersson, G. Öhrwall, T. Richter, P. Zimmermann, K. Godehusen, M. Martins, H.O. Karlsson, S.L. Sorensen, O. Björneholm, R. Feifel, K. Wiesner, O. Goscinski, L. Karlsson, S. Svensson. and A.J. Yencha, J. Phys. B **37** 1173 (2004).

[253] R. Püttner, M. Domke, D. Lentz, and G. Kaindl, J. Phys. B **29**, L565 (1996).

[254] J.P. Pique, F. Hartmann, R. Bacis, S. Churassy, and J.B. Koffend, Phys. Rev. Lett. **52**, 267 (1984).

[255] R.S. Mulliken, Trans. Faraday Soc. **25**, 634 (1929).

[256] A. Harvey and F.A. Jenkins, Phys. Rev. **35**, 789 (1930).

[257] Y.H. Jiang, R. Püttner, M. Martins, R. Follath, J.M. Rost, and G. Kaindl, Phys. Rev. A **69**, 052703 (2004).

[258] A. Thiel, J. Schirmer, and H. Köppel, J. Chem. Phys. **119**, 2088 (2003).

[259] R.S. Mulliken, Phys. Rev. **28**, 1202 (1926).

[260] R.S. Mulliken, Phys. Rev. **29**, 391 (1927).

[261] G. Herzberg, *Molecular Spectra and Molecular Structure, Spectra of Diatomic Molecules, Vol. 1*, (Krieger, Malabar, Florida, 1989), p. 139.

[262] A.D.J. Critchley, A.N. Hughes, and I.R. McNab, Phys. Rev. Lett. **86**, 1725 (2001).

[263] P. Cacciani and V. Kokoouline, Phys. Rev. Lett. **84**, 5296 (2000).

[264] N. Bouloufa, P. Cacciani, V. Kokoouline, F. Masnou-Seeuws, R. Vetter, and Li Li, Phys. Rev. A **63**, 042507 (2001).

[265] P. Cacciani, V. Kokoouline, N. Bouloufa, F. Masnou-Seeuws, R. Vetter, Phys. Rev. A **68**, 042506 (2003).

[266] R. Püttner, I. Dominguez, T.J. Morgan, C. Cisneros, R.F. Fink, E. Rotenberg, T. Warwick, M. Domke, G. Kaindl, and A.S. Schlachter, Phys. Rev. A **59**, 3415 (1999).

[267] F.Kh. Gel'mukhanov, *private communication.*

[268] P. Skytt, P. Glans, J-H. Guo, K. Gunnelin, C. Såthe, J. Nordgren, F.Kh. Gel'mukhanov, A. Cesar, and H. Ågren, Phys. Rev. Lett. **77**, 5035 (1996).

[269] M. Greiner, O. Mandel, T. Esslinger, T.W. Hañsch, and I. Bloch, Nature **415**, 39 (2002).

[270] W. Domcke and L.S. Cederbaum, Chem. Phys. **25**, 189 (1977).

[271] P. Pesic, Foundations of Phys. Lett. **13**, 55 (2000).

[272] R.C. Ashoori, Nature **379**, 413 (1996).

[273] M. Bayer, P. Hawrylak, K. Hinzer, S. Fafard, M. Korkusinski, Z.R. Wasilewski, O. Stern. and A. Forchel, Science **291**, 451 (2001).

[274] M. Pi, A. Emperador, M. Barranco, F. Garcias, K. Muraki, S. Tarucha, and D.G. Austing, Phys. Rev. Lett. **87**, 066801 (2001).

[275] T. Hayashi, T. Fujisawa, H.D. Cheong, Y.H. Jeong, and Y. Hirayama, Phys. Rev. Lett. **91**, 226804 (2003).

[276] J. Andruszkow *et al.*, Phys. Rev. Lett. **85**, 3825 (2000).

[277] V. Ayvazyan *et al.*, Eur. Phys. J. D **20**, 149 (2002).

[278] H. Wabnitz, L. Bittner, A.R.B. de Castro, R. Döhrmann, P. Gürtler, T. Laarmann, W. Laasch, J. Schulz, A. Swiderski, K. von Haeften, T. Möller, B. Faatz, A. Fateev, J. Feldhaus, G. Gerth, U. Hahn, E. Saldin, E. Schneidmiller, K. Sytchev, K. Tiedtke, R. Treusch, and M. Yurkov, Nature **420**, 482 (2002).

[279] T. Laarmann, A.R.B. de Castro, P. Gürtler, W. Laasch, J. Schulz, H. Wabnitz, and T. Möller, Phys. Rev. Lett. **92**, 143401 (2004).

[280] BESSY FEL Technical Design Report (March 2004), p. 305; available online at `http://www.bessy.de/lab_profile/01.FEL/felneu1de.html`.

[281] J.B. Pendry, *Low Energy Electron Diffraction* (Academic Press, London, 1974).

[282] S. Andersson and J.B. Pendry, Phys. Rev. Lett. **43**, 363 (1979).

[283] M.A. Van Hove, W.H. Weinberg, and C.-M. Chan, *Low Energy Electron Diffraction*, (Springer-Verlag, Heidelberg, 1986).

[284] S.A. Chambers, Adv. Phys. **40**, 357 (1991).

[285] P.A. Lee and J.B. Pendry, Phys. Rev. B **11**, 2795 (1975).

[286] D. Rolles, *Electron Angular Distributions in the Photoionization of Oriented Molecules*, (Diplomarbeit, TU Berlin, 2001); available online at `http://agb2.rz-berlin.mpg.de/~rolles/diplom.html`.

[287] D. Rolles, R. Díez Muiño, F.J. García de Abajo, C.S. Fadley, and M.A. Van Hove, J. Electron Spectrosc. Relat. Phenom. **114-116**, 107 (2001).

[288] R. Díez Muiño, D. Rolles, F.J. García de Abajo, F. Starrost, W. Schattke, C.S. Fadley, and M.A. Van Hove, J. Electron Spectrosc. Relat. Phenom. **114-116**, 99 (2001).

[289] R. Díez Muiño, D. Rolles, F.J. García de Abajo, C.S. Fadley, and M.A. Van Hove, Surf. Rev. Lett. **9**, 1213 (2002).

[290] J.A. Stephens and D. Dill, Phys. Rev. A **31**, 1968 (1985).

[291] J.A. Stephens, D. Dill, and J.L. Dehmer, J. Chem. Phys. **84**, 3638 (1986).

[292] A.V. Golovin and N.A. Cherepkov, J. Phys. B. **35**, 3191 (2002).

[293] A.V. Golovin, J. Adachi, S. Motoki, M. Takahashi, and A. Yagishita, J. Phys. B. **38**, L63 (2005).

[294] J.C. Slater and K.H. Johnson, Phys. Rev. B **5**, 844 (1972).

[295] K.H. Johnson, in *Advances in Quantum Chemistry, Vol.7*, edited by P.O. Löwdin, (Academic, New York, 1973), p. 143.

[296] P.M. Dittman, D. Dill, and J.L. Dehmer, J. Chem. Phys. **76**, 5703 (1982).

[297] J.R. Swanson and D. Dill, J. Chem. Phys. **77**, 2010 (1982).

[298] D. Dill and J.L. Dehmer, J. Chem. Phys. **61**, 692 (1974).

[299] J. Siegel, D. Dill, J.L. Dehmer, J. Chem. Phys. **64**, 3204 (1976).

[300] D. Dill and J. L. Dehmer, Phys. Rev. A **16**, 1423 (1977).

[301] J. Siegel, D. Dill, and J.L. Dehmer, Phys. Rev. A **17**, 2106 (1978).

[302] J.L. Dehmer, J. Siegel, and D. Dill, J. Chem. Phys. **69**, 5205 (1978).

[303] M.G. Lynch, D. Dill, J. Siegel, and J. L. Dehmer, J. Chem. Phys. **71**, 4249 (1979).

[304] J. Siegel, J. L. Dehmer, and D. Dill, Phys. Rev. A **21**, 85 (1980).

[305] J.L. Dehmer, J. Siegel, J. Welch, and D. Dill, Phys. Rev. A **21**, 101 (1980).

[306] M.J. Frisch *et al.*, *Gaussian 98 (Revision A.7)*, (Gaussian Inc, Pittsburgh PA, 1998).

[307] J.L. Beeby, Proc. R. Soc. A **302**, 113 (1967).

[308] P. Lloyd and P. V. Smith, Adv. Phys. **21**, 69 (1972).

[309] K.P. Huber and G. Herzberg, *Molecular spectra and molecular structure. IV. Constants of diatomic molecules*, (Van Nostrand Reinhold, New York, 1979).

Acknowledgements

A large group of people has contributed to this dissertation project, and without their great support and collaboration, it would simply not have been possible to perform, analyze, and understand all the experiments presented here.

First and foremost, I express my gratitude to Professor Uwe Becker for his full support, the scientific guidance and many inspiring discussions throughout the years, starting already before the beginning of my Diplomarbeit and lasting until this very day. I hope we will always stay close colleagues and collaborators!

I very much enjoyed working together with my present and former colleagues at the Fritz-Haber-Institut, Markus Braune, Slobodan Cvejanovic, Oliver Geßner, Rainer Hentges, Uwe Hergenhahn, Sanja Korica, Oliver Kugeler, Burkhard Langer, Toralf Lischke, Georg Prümper, Axel Reinköster, Jens Viefhaus, and Björn Zimmermann, to all of whom I owe a lot, and with whom I spent many good beamtimes at BESSY and HASYLAB. Especially Jens with his unquestionable competence and his very pleasant way of collaborating has made these a very enriching experience.

Concerning the experimental apparatus and in particular the ARFMADS ion spectrometer, I was very lucky to have Oliver Geßner's full support and expertise available even after he left the group to continue his career overseas. Not only did he leave his phone number and a fine spectrometer behind, which was ready to be employed, but he also contributed the initial data sets to the photoelectron diffraction experiment on CO.

For the interpretation of the diffraction data, the theoretical support by Björn Zimmermann was essential, who provided the excellent RCHF calculations and many helpful discussion.

Of course, the experiments at HASYLAB and BESSY would not have been possible without the help of the competent beamline scientists and engineers, in particular Birgit Zada, Willy Mahler and Thorsten Kachel at BESSY and Thomas Möller and Ralf Döhrmann at HASYLAB. They have proven almost infinite patience and literally laid the fate of their beamlines in our hands, while we turned and tweaked every single screw in order to achieve ultimate photon resolution.

Once the high-resolution was achieved and the data were successfully acquired, Uwe Hergenhahn's help with the fitting of the measured spectra was just as essential as many helpful discussions with him as well as with Ralph Püttner about the interpretation of the isotope effect and its influence on the vibrational structure and the Franck-Condon factors.

I would also like to thank Christa Hermanni, Beatrix Wieczorek and Evelyn Prohn at the Fritz-Haber-Institut for their support in administrative and technical questions, and Professor Gerard Meijer for providing a scientific and administrative home in the Molecular Physics department.

The theoretical basis for this work was, to a big extend, laid during my year of study abroad at the University of California in Berkeley, sponsored by the German Fulbright Commission, and my first stay at the Lawrence Berkeley National Laboratory in the group of Chuck Fadley. I had the pleasure to meet and work with a number of great people, among them Ricardo Díez Muiño, who is the "father" of the MSNSP formalism and who wrote most of the programs I used for the scattering calculations in this work, and Javier García de Abajo, who developed the underlying cluster approach for the multiple scattering. My wonderful time in Berkeley was made complete by the excellent support and guidance offered by Michel van Hove and Chuck Fadley who gave me a most impressive warm and friendly welcome in their group.

To my great pleasure, I was able to spend two more very productive and memorable years at the Berkeley Lab thanks to the Advanced Light Source's Doctoral Fellowship in Residence Program, which provided the funding as well as the logistic support for my stay in Berkeley during most of my doctoral work. I enjoyed the close collaboration with professor Dennis Lindle and his group, especially Renaud Guillemin, Oliver Hemmers, Wayne Stolte, and Anna Wolska, and thank them for their great hospitality and collegiality.

Many thanks to my friends, my colleagues and my family for proof reading this work, and to all those who may not have been mentioned explicitly but who contributed as well.

Streu- und Kohärenzeffekte in der Photoionisation kleiner Moleküle

Interferenz und Kohärenz sind grundlegende Wesenszüge der Quantenmechanik und spielen in der molekularen Photoionisation eine entscheidende Rolle. In der vorliegenden Arbeit werden Streu- und Kohärenzphänomene daher exemplarisch in der Innerschalen-Photoionisation des Kohlenmonoxid- und Stickstoffmoleküls untersucht, und die in diesem Zusammenhang angewandten Messmethoden der winkelaufgelösten Elektronen-Flugzeitspektroskopie sowie der hochauflösenden Photoelektronen-Fragmentionen Koinzidenzspektroskopie werden vorgestellt. Letztere ermöglicht die Messung der Photoelektronenwinkelverteilung orientierter Moleküle (’fixed-in-space molecules’) und eröffnet dadurch direkte Einblicke in die Photoionisationsdynamik und die elektronische Struktur der betrachteten Systeme, die weit über die Möglichkeiten der bisherigen Experimente an Molekülen in der Gasphase hinausgehen.

Am Beispiel der erstmals über einen weiten Energiebereich untersuchten Photoelektronenbeugung an freien Kohlenmonoxidmolekülen wird der Einfluss der Photoelektronenstreuung auf die Dynamik der Innerschalenphotoionisation demonstriert. Dabei wird insbesondere ein unterschiedliches Verhalten der Vorwärts- und Rückwärts-Streukanäle sichtbar, das unter anderem den Mehrfachstreucharakter der sogenannten Formresonanz (’shape resonance’) belegt. Darüber hinaus ermöglicht die Analyse der Diffraktionsmodulation des Rückwärts-Streukanals erstmalig eine Bestimmung der molekularen Struktur eines freien Moleküls durch Photoelektronenbeugung.

Die Innerschalen-Photoionisation von homonuklearen, zweiatomigen Molekülen und die Frage der Lokalisation oder Delokalisation von Innerschalen-Löchern werden am Beispiel des Stickstoffmoleküls N_2 behandelt. An Hand der Winkelverteilung der $1\sigma_g$ und $1\sigma_u$ Photoelektronen wird dabei erstmalig gezeigt, dass die Photoelektronenemission in einem solchen System als molekulares Doppelspaltexperiment interpretiert werden kann. Die in der Inversionssymmetrie des Moleküls zum Ausdruck kommende Ununterscheidbarkeit der beiden atomaren Zentren führt zur kohärenten Emission der Photoelektronen und zu charakteristischen, die Delokalisation der Rumpflöcher widerspiegelnden Interferenzmus-

tern in der Photoelektronenwinkelverteilung.

Durch Vergleich des natürlich vorkommenden $^{14,14}N_2$ Stickstoff-Moleküls mit den isotopensubstituierten Molekülen $^{14,15}N_2$ und $^{15,15}N_2$ wird der Übergang vom inversionssymmetrischen zum symmetriegebrochenen System untersucht. Dabei zeigte sich, dass der durch die Isotopensubstitution verursachte Symmetriebruch in $^{14,15}N_2$ zu einer teilweisen Lokalisation des Rumpfloches und zu paritätsgemischten Photoelektronenwellen führt. Die $1\sigma_g$ und $1\sigma_u$ Zustände verlieren ihre Reinheit als Eigenfunktionen des Paritätsoperators, und es kommt zu einer Mischung beider Zustände und in der Folge zu einer Änderung des Wirkungsquerschnitts und der Winkelverteilung im Prozentbereich. Dieser unerwartete Isotopeneffekt auf die elektronische Struktur eines homonuklearen zweiatomigen Moleküls ist der erste in der Photoelektronenspektroskopie beobachtete Effekt dieser Art und veranschaulicht den Beginn eines kontinuierlichen Übergangs des kohärenten, delokalen zu einem inkohärenten, lokalen System. Dieser Übergang ist vergleichbar mit der in Teilcheninterferenzexperimenten beobachteten ’Dekohärenz’ und hat zum Beispiel auch in der Erforschung von Quantenpunkten konkrete und technische Bedeutung, da diese zur Speicherung von Quantenbits und als Bausteine für Quantengatter in Quantencomputern in Betracht gezogen werden. Weiterführende ’pump-probe’ Experimente an dem in diesem Jahr in Betrieb gehenden ’Freie Elektronen Laser’ (VUV-FEL) könnten die in dieser Arbeit gefundenen Erkenntnisse weiter vervollständigen und damit neue, wichtige Beiträge zur Erforschung von Kohärenz- und Dekohärenzprozessen leisten.